7

TISSUE POLARIMETRY

ALEX VITKIN,[1] NIRMALYA GHOSH,[2] AND ANTONELLO DE MARTINO[3]

[1]*Medical Biophysics and Radiation Oncology, University of Toronto, Toronto, ON, Canada*
[2]*Department of Physical Sciences, Indian Institute of Science Education and Research, Kolkata, India*
[3]*Ecole Polytechnique, Palaiseau, France*

7.1 INTRODUCTION

Although optical characterization of tissues is increasingly being studied and used for biomedical diagnostics, in the vast majority of cases this characterization is based on *intensity* measurements. However, the interaction with the sample of interest also induces significant changes in light *polarization*, which also conveys useful information about the morphology and functional state of the investigated tissue [1–4]. Polarimetry typically provides contrasts quite different from those observed in ordinary intensity imaging. Taken alone or in conjunction with other techniques these contrasts may prove very useful for biomedical diagnostics.

In spite of its great potential, polarimetry is far from having reached the same degree of maturity in the biomedical field as intensity-based techniques. One possible reason for this "lag" is the strongly depolarizing nature of almost all biological tissues, which require sophisticated experimental setups and data treatment procedures to be properly characterized. In fact, in complex random media like tissues, numerous complexities due to multiple scattering and spatially inhomogeneous birefringence, as well as simultaneous occurrences of several polarization events, present

Photonics: Scientific Foundations, Technology and Applications, Volume IV, First Edition.
Edited by David L. Andrews.

formidable challenges for biomedical tissue polarimetry [3]. However, polarimetric instrumentation as well as theoretical understanding and numerical simulation of the interaction of polarized light and biological tissues are progressing impressively, paving the way for attractive applications. Polarization can be used to discriminate singly versus multiply scattered light. Tissue optical anisotropy and depolarization power may be characterized quantitatively, even when these effects occur simultaneously. Via proper analysis and modeling, these data may ultimately provide reliable techniques for "optical biopsy" which, in turn, may dramatically improve the management of various diseases.

In this chapter, we review polarized light fundamentals and mathematical formulations of polarized light and its propagation in biological tissues, discuss advances in various emerging polarimetric measurement systems, describe forward and inverse problems in polarimetry of turbid media (both theoretical modeling and experimental validation), and focus on applications related to tissue diagnosis and assessment.

7.2 POLARIZED LIGHT FUNDAMENTALS

7.2.1 Polarization States

7.2.1.1 Totally Polarized States For a purely monochromatic optical wave of frequency ω, propagating along the z axis, its electric field $\mathbf{E}$ vibrates in the xy plane according to

$$\mathbf{E}(z,t) = \begin{bmatrix} E_{0x}\cos(\omega t - \beta z + \phi_x) \\ E_{0y}\cos(\omega t - \beta z + \phi_y) \end{bmatrix} = \mathrm{Re}[\exp(i\omega - i\beta z)\mathbf{J}], \tag{7.1}$$

with

$$\beta = |\boldsymbol{\beta}| = (n - ik)\frac{\omega}{c} \tag{7.2}$$

being the modulus of the propagation vector $\boldsymbol{\beta}$, c is the speed of light in vacuum, and n and k are the real and imaginary parts of the refractive index, which determine, respectively, the speed of light and the absorption in the medium. The amplitudes E_{0i} and phases ϕ_i are constants and define the Jones vector $\mathbf{J}$ as [5–7]

$$\mathbf{J} = \begin{bmatrix} E_{0x}\exp(i\phi_x) \\ E_{0y}\exp(i\phi_y) \end{bmatrix}. \tag{7.3}$$

The *polarization* of the wave—the shape of the trajectory described by $\mathbf{E}$ in the xy plane—depends only on the ratio of the amplitudes $\tan\alpha$ and the phase difference φ defined, respectively, as

$$\tan\upsilon = \frac{E_{0y}}{E_{0x}} \text{and} \quad \phi = \phi_y - \phi_x. \tag{7.4}$$

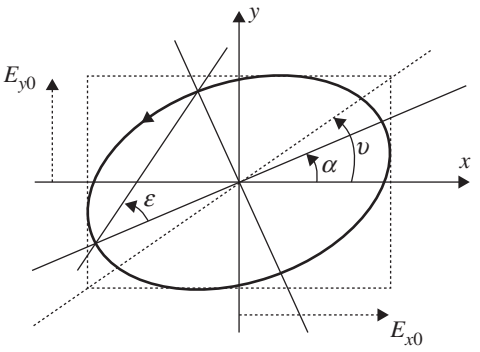

FIGURE 7.1 The polarization ellipse of a wave propagating in the z direction (toward the observer). E_{0x} and E_{0y} are the amplitudes of the field oscillations along the x and y directions; their ratio is equal to $\tan \upsilon$. α is the azimuth of the major axis of the ellipse and ε is its ellipticity. Ellipticity is positive or negative for left- or right-handed states, respectively.

This trajectory is in general elliptical and is represented in Figure 7.1. Besides the parameters defined in Eq. (7.4), the ellipse can also be described by the orientation (azimuth) α of its major axis and its ellipticity ε, which is positive for left handedness and negative for right handedness. The ellipticity ε varies between the two limits of zero (linearly polarized light) and $\pm 45°$ (circularly polarized light), which thus represent the two limits of generally elliptical polarization. Table 7.1 lists the Jones vectors of usual polarization states (with H, V, P, and M for linear polarizations along the horizontal, vertical, $+45°$, and $-45°$ directions, and L and R for left and right circular polarizations, respectively).

The *intensity* of a fully polarized wave characterized by the Jones vector **J** is given by

$$I = I_x + I_y = \frac{1}{2}\left(E_{ox}^2 + E_{oy}^2\right) = \frac{1}{2}(J \otimes J^*). \tag{7.5}$$

TABLE 7.1 Usual polarization states: Jones vectors, azimuths, ellipticities, and shapes of the ellipses

State	H	V	P	M	L	R	Elliptical
J	$\begin{bmatrix}1\\0\end{bmatrix}$	$\begin{bmatrix}0\\1\end{bmatrix}$	$\frac{1}{\sqrt{2}}\begin{bmatrix}1\\1\end{bmatrix}$	$\frac{1}{\sqrt{2}}\begin{bmatrix}1\\-1\end{bmatrix}$	$\frac{1}{\sqrt{2}}\begin{bmatrix}1\\-i\end{bmatrix}$	$\frac{1}{\sqrt{2}}\begin{bmatrix}1\\i\end{bmatrix}$	$\begin{bmatrix}\cos\alpha\cos\varepsilon - i\sin\alpha\sin\varepsilon\\ \sin\alpha\cos\varepsilon + i\cos\alpha\sin\varepsilon\end{bmatrix}$
α	0	90°	45°	−45°	Undefined	Undefined	α
ε	0	0	0	0	45°	−45°	ε
Shape of the ellipse	→	↑	↗	↖	◯	◯	⬭

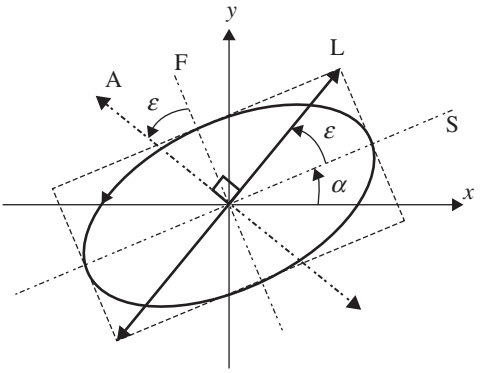

FIGURE 7.2 Illustration of the extinction method of analysis of arbitrary elliptical polarizations. The initial elliptical polarization is transformed into a linear one (L) by inserting a quarter-wave plate with its slow axis S at azimuth α. Extinction is then obtained by setting a linear analyzer A perpendicular to L. The ellipticity ε is thus measured as the angle between the analyzer set for extinction and the fast axis F of the quarter-wave plate.

Experimentally, the usual "recipe" to determine that a light beam propagating along z is linearly polarized along an azimuth α is to observe its *extinction* through a linear analyzer set perpendicular to α. This characterization may be extended to elliptically polarized beams as illustrated in Figure 7.2.

To determine the ellipticity ε (as the beam may not be fully linearly polarized), a quarter-wave plate (QWP) is inserted in the beam path with its slow axis at the azimuth α. Due to the 90° induced phase shift thus introduced, the initial incident elliptical polarization is transformed into a linear one, oriented at $\alpha + \varepsilon$ from the x reference axis. Then, a linear analyzer with its passing axis set at ε from the fast axis of the QWP will totally extinguish the beam. In practice, the extinction is achieved by trial-and-error procedure, and the azimuth α and the ellipticity ε are eventually determined from the angular settings of the QWP and the analyzer when maximum extinction is obtained.

7.2.1.2 Partially Polarized States If one tries the extinction method to characterize "natural" light directly coming from a source such as the sun or a light bulb, the detected intensity is seen to be independent of the settings of the QWP and the analyzer. One can thus conclude that the light coming from the sun or the light bulb is *totally depolarized*.

In other cases—for example the light coming from a bulb but reflected on a plastic floor en route to observer—the intensity detected through the QWP and the analyzer varies between $I_{\min}$ and $I_{\max}$. This provides an experimental definition of the *degree of polarization* (DOP) of the light beam

$$\mathrm{DOP} = \frac{I_{\max} - I_{\min}}{I_{\max} + I_{\min}}. \tag{7.6}$$

For totally polarized states, $I_{\min}$ vanishes and DOP = 1. At the other extreme, for totally unpolarized light $I_{\min} = I_{\max}$ and DOP = 0. For partially polarized states, the DOP may take any intermediate values between zero and one.

For partially polarized states, the motion of the electric field in the *xy* plane is no longer a perfect ellipse, but rather a somewhat *disordered* one. In case of a totally random motion of the electric vector **E**, one would surmise that in the extinction procedure the analyzer would detect the same constant intensity. What is implicitly assumed in this description is that the light polarization may be defined at any instant, but may vary significantly over time scales much shorter than the integration time of the detector. As a result, this detector takes the *temporal averages of the intensities*, sequentially generated by *different totally polarized states*. While this idea is basically correct, it is important to emphasize that this averaging of intensities (i.e., *incoherent* sum) of polarized contributions is not necessarily temporal.

To this end, consider the scattering experiments schematized in Figure 7.3. In one case (top panel), the object is optically thin and the laser undergoes single scattering by the rough surface. Conversely, in the other case the object is optically thick and multiple scattering is dominant. In both cases, the incident laser beam is spatially coherent, and the scattering objects are *static* (we ignore for the moment any possible thermal/Brownian motions). It is well known that in these conditions what is observed on the screen is a *speckle pattern* due to the interferences, at each point of the screen, of many scattered waves which reach this point with random (but static) amplitudes and relative phases [8].

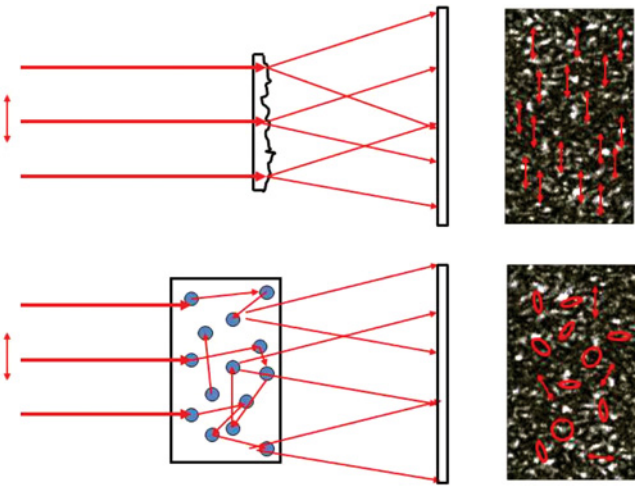

FIGURE 7.3 Scattering experiment of a linearly polarized coherent beam by static samples. Top: single scattering by a thin sample. The polarization state of the speckle spots is the same as that of the incident beam throughout the speckle pattern. Bottom: multiple scattering by an optically thick sample. The polarization state varies from speckle to speckle. *(For a color version of this figure, see the color plate section.)*

The major difference between single and multiple scattering regimes is that for the former, the polarization of all scattered waves is the same as that of the incident laser, while in case of multiple scattering these polarizations are random. Consequently, as outlined in Figure 7.3, for single scattering all the speckles feature the same polarization as the incident laser, while in the other case, each speckle is still *fully polarized*, *but this polarization varies randomly from one speckle to the next*.

Can one thus conclude that multiple scattering always depolarizes an incident polarized beam? The correct answer depends on how the sample is illuminated and how the emerging light is detected.

- If the beam is *coherent*, the sample is *static and the detection zone is smaller than the size of the speckles, then there is no depolarization*. The initial polarization state is converted into another fully polarized one at each point of the speckle pattern.
- If *the detector is much larger than the speckle size,* then if one applies the extinction method to analyze the polarization, some speckles will exhibit varying intensity, but randomly so (different speckles displaying different polarization states). Thus, the overall detected signal will be constant, and according to the criterion defined in Eq. (7.6), *the detected light is totally depolarized*. This is because the large detector performs a *sum of intensities* of the contributions of different polarized states (the speckles), this sum being performed spatially in this case. On the other hand, for single scattering the same large detector would see an extinction for suitably aligned QWP and analyzer, and the emerging light would be considered fully polarized.
- If the illumination beam *is not spatially coherent* (which is generally the case for a beam from a classical source), then the relative phases at different points of this beam change very rapidly, and so does the resultant speckle pattern. As a result, even if the detector is small, the polarization will vary rapidly in time, and the measured DOP would be small.
- The same conclusion may be reached (strong depolarization at each point of the screen) if the beam is coherent but the sample *is not static*, as for example a liquid suspension of small scatterers which undergo Brownian motion. However, the typical time constants for Brownian-motion-induced speckle variations are much longer (ms to seconds) than those due to the lack of spatial coherence for a light beam coming from a classical source (∼fs), and they may be temporally resolved by many detectors.
- Finally, if the incident light is *polychromatic*, then each wavelength creates its own speckle pattern, with basically no correlation between the patterns created at different wavelengths. As no interferences are possible between waves with different wavelengths, the incoherent intensity summation takes places naturally, leading to depolarization in each point of the observation screen.

To summarize, "true" depolarization requires that the detected signal is *the sum of intensities due to various polarized contributions with different polarizations*. This

summation may be performed temporally, spatially, or spectrally, and it depends not only on the sample itself but also on the characteristics of the illumination beam and of the detection system.

7.2.1.3 Stokes Vectors Following the above presentation, polarized states are not characterized in terms of well-determined field amplitudes, but rather from intensities measured through various analyzers, which are in turn averages of quadratic functions of the field amplitudes. These quantities may be arranged in various ways. The most commonly used is the *Stokes vector*, which is a real four-row single-column array defined as

$$S = \begin{bmatrix} I \\ Q \\ U \\ V \end{bmatrix} = \begin{bmatrix} Ix + Iy \\ Ix - Iy \\ IP - IM \\ I_{\mathrm{L}} - I_{\mathrm{R}} \end{bmatrix} = \begin{bmatrix} \left\langle E_x E_x^* + E_y E_y^* \right\rangle \\ \left\langle E_x E_x^* - E_y E_y^* \right\rangle \\ \left\langle E_x E_y^* + E_y E_x^* \right\rangle \\ \left\langle i(E_x E_y^* - E_y E_x^*) \right\rangle \end{bmatrix}, \tag{7.7a}$$

where I_x, I_y, I_P, and I_M are the intensities measured through ideal linear polarizers oriented along x or y axes, or at $+45°$ or $-45°$ azimuths. I_{L} and I_{R} are measured through left and right circular polarizers, respectively. It can be shown [9–12] that Stokes vectors can define any polarization state and any DOP. The first element I is the polarization-independent light intensity, and as such is equal to any other sum of orthogonal intensities (e.g., $I_P + I_M$ or $I_{\mathrm{L}} + I_{\mathrm{R}}$). Also note that $\mathbf{S}$ is not a vector in the geometric space, rather this array of intensity values represent a directional vector in the polarization state space (Poincaré sphere, described subsequently). For totally polarized states defined by Jones vectors of the form given by Eq. (7.3), the corresponding Stokes vectors are

$$\mathbf{S} = \begin{pmatrix} \frac{1}{2}\left(E_{0x}^2 + E_{0y}^2\right) \\ \frac{1}{2}\left(E_{0x}^2 - E_{0y}^2\right) \\ (E_{0x}E_{0y}\cos\varphi) \\ (E_{0x}E_{0y}\sin\varphi) \end{pmatrix}. \tag{7.7b}$$

Note that the Stokes vector by its definition (Eq. 7.7a) incorporates both the pure (totally polarized) and mixed (partially polarized) states and this definition evolves from the so-called 2×2 coherency matrix $\mathbf{N}$ [12]. The coherency matrix is defined through the ensemble averaged Jones vector as $\mathbf{N} = \langle J \otimes J^* \rangle$ and accordingly its four elements are $\langle E_x E_x^* \rangle$, $\langle E_x Ey^* \rangle$, $\langle E_y E_x^* \rangle$, and $\langle E_y E_y^* \rangle$ [12]. Conversely, it follows that the Stokes vector elements (I, Q, U, and V) are the expansion coefficients of the coherency matrix in terms of the identity matrix and the three Pauli spin matrices [12].

TABLE 7.2 Normalized Stokes vectors for usual totally polarized states (cf Table 7.1)

State	H	V	P	M	L	R	Elliptical
S	$\begin{bmatrix}1\\1\\0\\0\end{bmatrix}$	$\begin{bmatrix}1\\-1\\0\\0\end{bmatrix}$	$\begin{bmatrix}1\\0\\1\\0\end{bmatrix}$	$\begin{bmatrix}1\\0\\-1\\0\end{bmatrix}$	$\begin{bmatrix}1\\0\\0\\1\end{bmatrix}$	$\begin{bmatrix}1\\0\\0\\-1\end{bmatrix}$	$\begin{bmatrix}1\\\cos 2\alpha\ \cos 2\varepsilon\\\sin 2\alpha\ \cos 2\varepsilon\\\sin 2\varepsilon\end{bmatrix}$

Stokes vectors can be written in normalized form as

$$\mathbf{S}^{\mathrm{T}} = I\left(1, \frac{Q}{I}, \frac{U}{I}, \frac{V}{I}\right) = I(1, q, u, v) = I(1, \mathbf{s}^{\mathrm{T}}), \tag{7.7c}$$

where the superscript $^{\mathrm{T}}$ means the transpose. The three intensity-normalized coordinates q, u, and v are the quantities which *actually define the polarization state* independently of the total intensity I. The normalized Stokes vectors for usual fully polarized states are listed in Table 7.2.

At the other extreme, for *totally unpolarized states*, $Q = U = V = 0$, which corresponds to the fact that no matter how the analyzer is oriented, for such states the transmitted intensity is always the same, equal to one half of the total intensity.

The DOP defined experimentally in Eq. (7.6) can be expressed in terms of the normalized Stokes vector components as

$$\mathrm{DOP} = \sqrt{q^2 + u^2 + v^2}. \tag{7.8a}$$

It is straightforward to check that for Stokes vectors of the form (7.7b) we get DOP = 1. In addition to the overall DOP, we can define the linear and circular DOPs, respectively, as

$$\mathrm{DOP_L} = \sqrt{q^2 + u^2} \quad \text{and} \quad \mathrm{DOP_C} = v. \tag{7.8b}$$

Experimentally, the $\mathrm{DOP_L}$ can be measured by the extinction method using only a rotatable linear polarizer, without the QWP. Equation (7.6) then applies with $I_{\max}$ and $I_{\min}$, representing the maximum and minimum intensities measured when the polarizer is rotated. On the other hand, $\mathrm{DOP_C}$ can be measured by using left and right circular polarizers. Calling again I_{L} and I_{R} the intensities measured through these circular polarizers, $\mathrm{DOP_C}$ is given by the same formula (7.6) but with I_{L} and I_{R} replacing $I_{\min}$ and $I_{\max}$.

Physical realizability. In contrast with Jones vectors, which could be any 2D complex vectors, any four-dimensional element real array is not necessarily an acceptable Stokes vector, due to the condition

$$\mathrm{DOP} \leq 1. \tag{7.9}$$

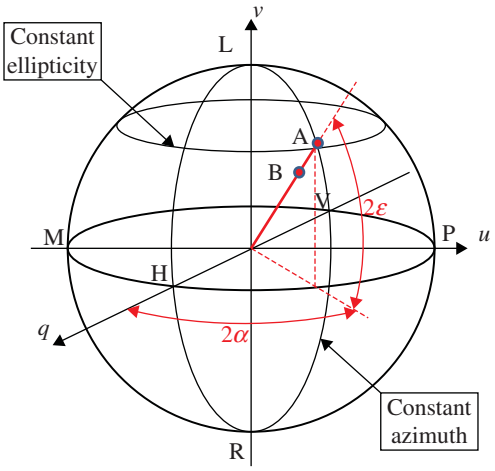

FIGURE 7.4 Geometrical representation of Stokes vectors within the Poincaré sphere. Any given polarization state is represented by a point whose Cartesian coordinates are the intensity-normalized coordinates (q, u, v). The radial coordinate is the DOP and the "longitude" and "latitude" are, respectively, 2α and 2ε. Totally polarized states are found at the surface of the unit radius sphere, while partially polarized states are inside (e.g., points A and B, respectively). Linearly polarized states, among which H, V, P, and M states, are on the "equator" while the L and R circular states are found at the "poles."

The Poincaré sphere. A very convenient geometrical representation of all possible polarization states involves the intensity-normalized coordinates q, u, and v defined above, as illustrated in Figure 7.4 [12]. In this space, the DOP is nothing else but the distance of the representative point from origin. Thus, the physical realizability condition given by Eq. (7.9) implies that all acceptable Stokes vectors are represented by points located within the unit radius sphere, also called the *Poincaré sphere*. Totally polarized states are found at the surface of the sphere (point A) while partially polarized states are inside (point B). The other spherical coordinates, the points "latitude" and "longitude" are nothing else but twice the azimuth α and ellipticity ε, as shown by the last column of Table 7.2 for totally polarized states. As shown throughout this chapter, this geometrical representation provides simple and intuitive descriptions of many aspects of the interaction between polarized light and samples and/or instruments.

Before we move on to define sample polarization interactions through this "conventional" Stokes–Mueller algebra, it may be worthwhile to briefly mention the validity regime of such algebra. Note that both the Jones vector (in the field representation, Eq. 7.3) and the Stokes vector (intensity-based representation, Eq. 7.7a) deal with two-dimensional electromagnetic field and are applicable when the light wave is completely transverse (plane electromagnetic waves or more generally to uniformly polarized elementary beams). However, it has been shown that even for paraxial beam-like fields, the spatial mode (field distribution) and polarization are

not always separable (unlike plane waves or elementary beams), and accordingly one needs different algebra to describe such inhomogeneous polarization [13]. This so-called *classical entanglement* between polarization and spatial mode is handled by defining beam coherency polarization matrix (a variant of the 2×2 coherency matrix incorporating simultaneously both the field polarization and its spatial distribution) [13]. In other general cases involving three-dimensional field (as encountered in tight focusing scenarios and in the near field), the two-dimensional polarimetry formalisms have been extended via the definition of 3×3 coherency matrix and generalized nine-element Stokes vector [14]. Moreover, there are other emerging "unconventional" polarization algebra formulations involving vector beams, geometric phases (Pancharatnam–Berry phase) arising from spin orbit interactions of light, radial, and azimuthal polarization of light beams, and so forth [15–17]. Even though such generalized polarization algebra may find useful biomedical applications; these have yet not been explored in tissue polarimetry research (possibly due to the unknown magnitude/relative importance of these effects in tissues, and possibly due to the numerous complexities in tissue signal detection and analysis). We thus restrict our discussion to the "conventional" polarization algebra and its applications in tissue polarimetry.

7.2.2 Interaction with a Sample

7.2.2.1 Mueller Matrices For any optical system operating in the linear regime (which is always the case except when the light source is a high power pulsed laser), the output intensities are linear functions of the inputs. As a result, the transformation of the Stokes vectors must also be linear, thus described by a 4×4 real matrix $\mathbf{M}$ called Mueller matrix [18]:

$$\mathbf{S}_{\text{out}} = \mathrm{M} \bullet \mathrm{S}_{\text{in}}. \tag{7.10}$$

In analogy with $\mathbf{S}$, which represents the polarization *state of the beam*, $\mathbf{M}$ thus represents the corresponding polarization *properties of the sample*; the link between the two is accomplished via the Mueller–Stokes calculus as described by Eq. (7.10).

Physical realizability. Analogous to Stokes vectors, any 4×4 real matrix is not necessarily a physically acceptable Mueller matrix. An obviously necessary condition is that in never transforms a physically acceptable Stokes vector $\mathbf{S}_{\text{in}}$ into an "overpolarized" one $\mathbf{S}_{\text{out}}$, with DOP > 1. However, this condition is necessary but not sufficient. A general procedure for determining the acceptability of $\mathbf{M}$, based on the calculation of the so-called coherency matrix $\mathbf{N}$ [12, 19], is given in Reference 20 and is outside the scope of this review. This procedure may also be used to "correct" a slightly unphysical matrix (possibly due to measurement errors) to make it acceptable.

Depolarizing or nondepolarizing character. A physically acceptable Mueller matrix is said to be *nondepolarizing* if any input totally polarized Stokes vector $\mathbf{S}_{\text{in}}$ is transformed into a totally polarized $\mathbf{S}_{\text{out}}$. (in other words, the DOP does not decrease). Necessary and sufficient conditions for a matrix to be nondepolarizing

have been examined [20,21]. Conversely, for depolarizing Mueller matrices the DOP of $\mathbf{S}_{\text{out}}$ is smaller than that of $\mathbf{S}_{\text{in}}$. It is important to note that, for any resulting Mueller matrix, the reduction of the DOP depends on the input state $\mathbf{S}_{\text{in}}$; for example, a given tissue sample in a particular examination geometry can be more depolarizing for input circular states than for input linear ones, or vice versa. It is therefore impossible to *uniquely* define the depolarization power of a generic Mueller matrix $\mathbf{M}$.

Among the various definitions of this depolarization power of a sample described by $\mathbf{M}$, one very widely used is the "depolarization index" P_{d} [22]:

$$P_{\text{d}} = \sqrt{\frac{\sum_{i,j} M_{i,j}^2 - M_{1,1}^2}{3M_{1,1}^2}} = \sqrt{\frac{Tr(\mathbf{M}^T\mathbf{M}) - M_{1,1}^2}{3M_{1,1}^2}}, \tag{7.11}$$

which varies from 0 for a total depolarizer to 1 for nondepolarizing matrices.

7.2.2.2 Diattenuation and Polarizance These two properties can be determined *unambiguously* for any Mueller matrix $\mathbf{M}$ from its very definition in terms of intensities. Quite generally, $\mathbf{M}$ can be rewritten as

$$\mathbf{M} = m_{11} \begin{pmatrix} 1 & \mathbf{D}^{\text{T}} \\ \mathbf{P} & \mathbf{m} \end{pmatrix}, \tag{7.12}$$

where $\mathbf{D}$ (first row) and $\mathbf{P}$ (first column) are the *diattenuation* and *polarizance* vectors, respectively, while $\mathbf{m}$ is a 3×3 real matrix. These formulations are easily justified as follows.

Diattenuation. For a diattenuating system, *the output intensity depends on the polarization of the incident wave*. If we consider an intensity-normalized input Stokes vector $\mathbf{S}$

$$\mathbf{S}_{\text{in}}^{\text{T}} = (1, \mathbf{s}^{\text{T}}) \quad \text{with} \quad \|\mathbf{s}\| = \text{DOP} \leq 1 \tag{7.13}$$

corresponding to arbitrary polarizations at constant intensity (normalized to 1), then the output intensity (i.e., the first component of $\mathbf{S}_{\text{out}}$) is simply given by

$$I_{\text{out}} = m_{11}(1 + \mathbf{D} \cdot \mathbf{s}). \tag{7.14}$$

This output intensity reaches its maximum (resp. minimum) value I_{max} (resp. I_{min}) when the scalar product $\mathbf{D} \cdot \mathbf{s}$ is maximum (resp. minimum) under the constraint $\|\mathbf{s}\| = \text{DOP} \leq 1$, that is, when $\mathbf{s} = \pm\frac{\mathbf{D}}{\|\mathbf{D}\|}$. We thus obtain

$$\mathbf{S}_{\text{max}}^{\text{T}} = \left(1, \frac{\mathbf{D}^{\text{T}}}{\|\mathbf{D}\|}\right) \quad \text{and} \quad I_{\text{max}} = m_{11}(1 + \|\mathbf{D}\|) \tag{7.15a}$$

$$\mathbf{S}_{\text{min}}^{\text{T}} = \left(1, -\frac{\mathbf{D}^{\text{T}}}{\|\mathbf{D}\|}\right), \quad \text{and} \quad I_{\text{min}} = m_{11}(1 - \|\mathbf{D}\|) \tag{7.15b}$$

from which we immediately get for the *scalar diattenuation D*

$$D = \frac{I_{\max} - I_{\min}}{I_{\max} + I_{\min}} = \|\mathbf{D}\|. \tag{7.16}$$

In summary, the diattenuator vector **D** defines both the scalar diattenuation D and the polarization states transmitted with the largest (or the lowest) intensity. Note that the two polarization states providing these extreme intensity transmission values are totally polarized, and located at diametrally opposite positions on the Poincaré sphere.

Polarizance. We now consider this property which corresponds to the capacity of the sample to polarize incoming beams, specifically *to impart a finite DOP to an unpolarized input beam*. In this case the Stokes vector of the output beam is simply

$$\mathbf{S}_{\text{out}} = m_{11} \begin{pmatrix} 1 & \mathbf{D}^{\mathrm{T}} \\ \mathbf{P} & \mathbf{m} \end{pmatrix} \begin{pmatrix} I \\ 0 \\ 0 \\ 0 \end{pmatrix} = m_{11} I \begin{pmatrix} 1 \\ \mathbf{P} \end{pmatrix}. \tag{7.17}$$

In a way analogous to diattenuation, from the polarizance vector **P** we can define a scalar polarizance $P = \|\mathbf{P}\|$,

Independence of polarizance and diattenuation. In practice, diattenuation and/or polarizance may occur

- at *interfaces*, where the transmission and/or reflections coefficients may be different for the polarization in the plane of incidence (*p* polarization) or orthogonal to this plane (*s* polarization), due to the well-known Fresnel laws [23]: transmission is larger (and reflection is smaller) for *p* than for *s* polarization; and
- during *the propagation in bulk anisotropic materials*. In this case, diattenuation and/or polarizance is due to the dependence of the imaginary part of the optical refractive index on the light polarization.

For the simple cases cited above, the polarizance is directly related to the diattenuation: $\mathbf{P} = \mathbf{D}$. For more complex systems, and in particular depolarizing ones, **P** and **D** become totally independent parameters, as shown by the following examples:

1. Consider a *polarizer followed by a perfect depolarizer*. Such a system clearly exhibits diattenuation, as the intensity transmitted by the polarizer depends on the orientation of the incoming linear polarization. However, the beam emerging from the depolarizer is, by definition, totally depolarized, implying that an initially depolarized beam would remain totally depolarized. As a result, such a system exhibits a *strong diattenuation but no polarizance*.
2. Let us now consider *the same elementary components, but in reverse order* (depolarizer first, polarizer afterwards). In this case, any incoming polarized beam is transformed by the depolarizer into a totally depolarized beam whose

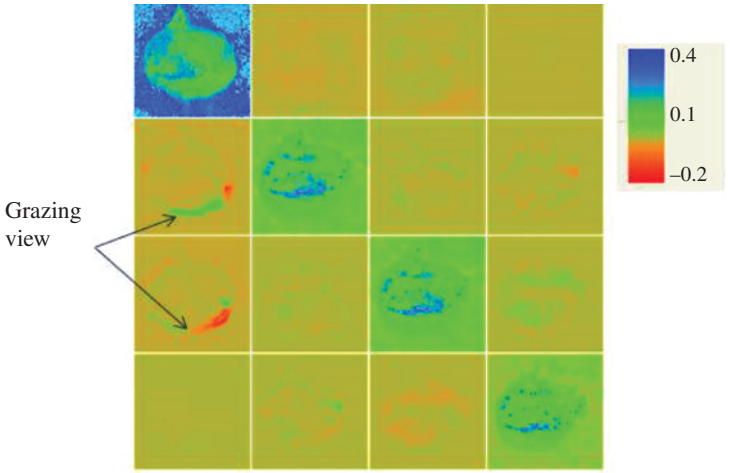

FIGURE 7.5 Normalized Mueller matrix image of a resected human cervix in backscattering geometry. The field of view is 3×3 cm^2. The sample is about 5 mm thick and has conical shape. All elements are normalized by m_{11} and these normalized values are given in the color scale shown at top right, ranging from -0.2 to 0.4. This sample features no diattenuation, as shown by the vanishing elements in the first row, and significant linear polarizance (elements m_{21} and m_{31}) at some points where the light emerges at grazing angles from the sample surface, and is polarized by a local "Brewster angle" effect (A. de Martino, unpublished results). (*For a color version of this figure, see the color plate section.*)

intensity does not depend on the incoming polarization. Then, the polarizer transforms this beam into a polarized one, with always the same polarization. In contrast with the previous case, now the system exhibits *zero diattenuation but a strong polarizance* ($P = 1$ for a perfect output polarizer).

While such effects may seem purely "academic," they can actually occur in real systems, and more particularly in biological samples. Figure 7.5 shows a Mueller image of an *ex vivo* surgical sample of uterine cervix, normalized by m_{11}. On this image, some narrow regions, close to the edge of the sample, clearly exhibit nonzero linear polarizance (elements m_{21} and m_{31}), without any detectable counterpart in the diattenuation (elements m_{12} and m_{13}). As indicated in the figure, these regions are seen under *grazing angles*. Then, as outlined above, the light component polarized parallel to the local surface normal (the local p polarized component) is much better transmitted at the air–tissue interface than the component polarized parallel to the surface itself (the local s polarized component). As a result, the light emerging from these regions is strongly polarized even if the sample is illuminated with unpolarized light. On the other hand, the main contribution to this emerging light is due to rays impinging on the samples in other places, at incidences closer to normal and then multiply scattered. As a result, there is little or no diattenuation effect for these impinging rays and the situation is quite similar to the case 2 outlined above.

7.2.2.3 Homogeneous Diattenuators and Retarders Polarimetric elements are called homogeneous if they exhibit two fully polarized orthogonal eigenstates, that is, two polarization states which are transmitted without alteration and which do not interfere with each other. In practice, such light states are linearly polarized along two perpendicular directions, or circularly polarized and rotating in opposite senses. The normalized Stokes vectors $\mathbf{S}_1$ and $\mathbf{S}_2$ of such orthogonal states are of the form

$$\mathbf{S}_1^{\mathrm{T}} = (1, \mathbf{s}^{\mathrm{T}}),\ \mathbf{S}_2^{\mathrm{T}} = (1, -\mathbf{s}^{\mathrm{T}}) \tag{7.18}$$

with $\|\mathbf{s}\| = 1$, as these states are fully polarized. Orthogonal states are thus found on the surface of the Poincaré sphere at diametrally opposed positions. For any homogeneous polarimetric element, there are thus two (and only two) such states which are left invariant on the Poincaré sphere.

Homogeneous diattenuators: These elements are uniquely determined by their diattenuation vector $\mathbf{D}$. Their (totally polarized) eigenpolarization states corresponding, respectively, to maximum and minimum transmissions are given by Eqs. (7.15) with

$$\mathbf{s}_{\max} = \frac{\mathbf{D}}{D}, \qquad \mathbf{s}_{\min} = -\frac{\mathbf{D}}{D}. \tag{7.19}$$

The corresponding Mueller matrix is then given in synthetic form by [24]

$$\mathbf{M}_{\mathrm{D}} = \tau \begin{pmatrix} 1 & \mathbf{D}^{\mathrm{T}} \\ \mathbf{D} & \mathbf{m}_{\mathrm{d}} \end{pmatrix} \text{ where } \mathbf{m}_{\mathrm{D}} = \sqrt{1 - D^2}\mathbf{I}_3 + (1 - \sqrt{1 - D^2})\mathbf{D} \quad \mathbf{D}^{\mathrm{T}}, \tag{7.20}$$

where τ is the intensity transmission for incident unpolarized light. As already mentioned, diattenuation may occur due to reflection and/or refraction at an interface, or to propagation in anisotropic or chiral materials. Anisotropy may introduce *linear dichroism*. If so, for any propagation direction (except very particular ones determined by the symmetry of the material) the imaginary part of the refractive index k may take two different values, k_{L} and k_{H}; The former, corresponding the lowest absorption, is valid for a wave linearly polarized at azimuth θ and the latter for the orthogonal polarization, at $\theta + 90°$. The *linear* (scalar) dichroism is then defined as

$$\Delta k = k_{\mathrm{H}} - k_{\mathrm{L}} > 0. \tag{7.21}$$

For a parallel slab of thickness L, the intensity transmissions for the two eigenpolarizations are respectively

$$T_{\max} = \exp(-2k_{\mathrm{L}}L), \qquad T_{\min} = \exp(-2k_{\mathrm{H}}L) \tag{7.22}$$

resulting in a scalar diattenuation

$$D = \frac{T_{\max} - T_{\min}}{T_{\max} + T_{\min}} = \sinh(d) \tag{7.23}$$

where $d = \Delta kL$ is the dichroism integrated over the slab thickness L.

Chiral media (e.g., a biological fluid with glucose) can also feature dichroism, but then it is *circular dichroism*. The above formulas are still valid, but in this case the eigenpolarizations for which the absorption coefficients are well defined are left and right circular ones.

The matrix of a homogeneous diattenuator is symmetric, explicitly written for a linear diattenuator as [12]:

$$\mathbf{M}_{\mathrm{LD}}(\tau, D, \theta) = \frac{\tau}{2}\begin{pmatrix} 1 & D\cos 2\theta & D\sin 2\theta & 0 \\ D\cos 2\theta & \cos^2 2\theta + \sqrt{1-D^2}\sin^2 2\theta & (1-\sqrt{1-D^2})\cos 2\theta \sin 2\theta & 0 \\ D\sin 2\theta & (1-\sqrt{1-D^2})\cos 2\theta \sin 2\theta & \sin^2(2\theta) + \sqrt{1-D^2}\cos^2 2\theta & 0 \\ 0 & 0 & 0 & \sqrt{1-D^2} \end{pmatrix} \tag{7.24}$$

implying that the maximum and minimum intensity transmittances are obtained for linearly polarized states with azimuths θ and $\theta + 90°$. A straightforward calculation indeed shows that

$$\begin{aligned} \mathbf{M}_{\mathrm{LD}}(\tau, D, \theta)\begin{pmatrix} 1 \\ \cos 2\theta \\ \sin 2\theta \\ 0 \end{pmatrix} &= \frac{\tau}{2}(1+D)\begin{pmatrix} 1 \\ \cos 2\theta \\ \sin 2\theta \\ 0 \end{pmatrix} \quad \text{and} \\ \mathbf{M}_{\mathrm{LD}}(\tau, D, \theta)\begin{pmatrix} 1 \\ -\cos 2\theta \\ -\sin 2\theta \\ 0 \end{pmatrix} &= \frac{\tau}{2}(1-D)\begin{pmatrix} 1 \\ -\cos 2\theta \\ -\sin 2\theta \\ 0 \end{pmatrix} \end{aligned}, \tag{7.25}$$

which is a direct check that these states are unchanged by $\mathbf{M}_{\mathrm{LD}}(\tau,D,\theta)$, but are transmitted with intensity factors $\frac{\tau}{2}(1 \pm D)$. Similarly, for circular diattenuators the corresponding matrix is

$$\mathbf{M}_{\mathrm{CD}}(\tau, D) = \frac{\tau}{2}\begin{pmatrix} 1 & 0 & 0 & D \\ 0 & \sqrt{1-D^2} & 0 & 0 \\ 0 & 0 & \sqrt{1-D^2} & 0 \\ D & 0 & 0 & 1 \end{pmatrix} \tag{7.26}$$

and of course in this case there is no need to define any particular azimuth θ.

Homogeneous retarders: For these elements too there are two orthogonal eigenpolarization states, each of which is transmitted without modification of its shape. In contrast with diattenuators, retarders transmit both eigenstates with the same intensity coefficients, but *different phases*. This phase difference is the *scalar retardation* δ.

In practice, like diattenuation, retardation may be caused by reflection and/or refraction at an interface, or by propagation in anisotropic materials. This latter case is particularly relevant for tissue polarimetry. Anisotropic tissues are typically connective tissues, with fibrillar proteins (collagen is the prime example) which may be spatially organized with a preferential orientation. Then if we consider a light wave propagating along z, and call θ the azimuth of the fiber orientation direction in the xy plane, the refractive index is larger for light linearly polarized at azimuth θ than at $\theta + 90°$. These azimuths then define the *slow* (θ) and *fast* ($\theta = 90°$) *axes* in the xy plane, with refractive indices n_S and n_F. The *linear birefringence* of the material is then defined as

$$\Delta n = n_S - n_F. \tag{7.27}$$

Propagation over a distance L in such a material introduces a scalar retardation δ (in radians)

$$\delta = 2\pi \frac{\Delta n\, L}{\lambda}. \tag{7.28}$$

For homogeneous retarders, the orthogonal Stokes eigenvectors are again of the form given by Eq. (7.18). A pure retarder can be described geometrically as rotation in the space of Stokes vectors. Mathematically the Mueller matrix $\mathbf{M}_R$ of the retarder can be written in compact notation as [24]

$$\mathbf{M}_R = \begin{pmatrix} 1 & \mathbf{0}^T \\ \mathbf{0} & \mathbf{m_R} \end{pmatrix}, \tag{7.29}$$

where $\mathbf{0}$ represents the null vector and the 3×3 submatrix, $\mathbf{m_R}$, is a rotation matrix in the (q, u, v) space. As a result, the action of a homogeneous diattenuator on an arbitrary incident Stokes vector $\mathbf{S}$ is a mere rotation of its representative point on the Poincaré sphere, described by $\mathbf{m}_R$. Moreover, the axis of this rotation is defined by the two diametrally opposed points representing the two eigenpolarizations, and the rotation angle is nothing else but the retardation δ [12].

For *linear retarders* with eigenstates linearly polarized along θ and θ +90° azimuths, the Mueller matrices are [12]

$$\mathbf{M}_{LR}(\tau, \delta, \theta) = \tau \begin{pmatrix} 1 & 0 & 0 & 0 \\ 0 & \cos^2 2\theta + \sin^2 2\theta \cos\delta & \cos 2\theta \sin 2\theta\,(1 - \cos\delta) & -\sin 2\theta \sin\delta \\ 0 & \cos 2\theta \sin 2\theta\,(1 - \cos\delta) & \sin^2 2\theta + \cos^2 2\theta \cos\delta & \cos 2\theta \sin\delta \\ 0 & \sin 2\theta \sin\delta & -\cos 2\theta \sin\delta & \cos\delta \end{pmatrix} \tag{7.30}$$

And Eq. (7.25) is still valid, provided both intensity transmittance factors $\frac{\tau}{2}(1 \pm D)$ are replaced by τ.

We now consider *circular retarders*, that is, elements for which the eigenpolarizations are counter-rotating circular ones. The Mueller matrices of such elements are of the form:

$$\mathbf{M}_{\mathrm{CR}}(\psi) = \tau \begin{pmatrix} 1 & 0 & 0 & 0 \\ 0 & \cos 2\psi & -\sin 2\psi & 0 \\ 0 & \sin 2\psi & \cos 2\psi & 0 \\ 0 & 0 & 0 & 1 \end{pmatrix}. \tag{7.31}$$

When a linearly polarized wave interacts with a circular retarder, its polarization remains linear, but *it is rotated* by an angle ψ which is nothing else but the circular retardance, as it can be checked by a straightforward calculation analogous to that shown in Eq. (7.25). Circular birefringence is observed in media lacking any mirror symmetry, like solutions of chiral molecules where only one enantiomer is present. An example of major practical clinical importance is that of *glucose*, as discussed in greater detail later. Chiral media are usually characterized by their *optical activity* χ rather than their circular birefringence Δn_{c}:

$$\chi = \frac{2\pi}{\lambda}\Delta n \tag{7.32a}$$

so that the optical rotation ψ due to propagation over a distance L is simply

$$\psi = \chi L. \tag{7.32b}$$

We point out, however, that in tissues (like in essentially any usual materials, except for example some particular liquid crystals) optical activity is an *extremely weak* effect, much weaker than linear birefringence whenever this latter effect is present.

Finally, we point out that the scalar retardation of any homogeneous retarder (linear or circular) is easily determined from its Mueller matrix $\mathbf{M_R}$ as

$$\delta, \psi = \cos^{-1}\left(\frac{Tr(\mathbf{M}_{\mathrm{R}})}{2} - 1\right). \tag{7.33}$$

7.2.2.4 Depolarizers By definition, a depolarizer is an object that reduces the DOP of the incoming light. The conceptually simplest (and most relevant in practice) depolarizers are those for which the Mueller matrix $\mathbf{M}_\Delta$ is diagonal

$$\mathbf{M}_\Delta = \tau \begin{pmatrix} 1 & 0 & 0 & 0 \\ 0 & a & 0 & 0 \\ 0 & 0 & b & 0 \\ 0 & 0 & 0 & c \end{pmatrix} \tag{7.34}$$

with absolute values of a, b, and c smaller than 1. If so, any incident Stokes vector $\mathbf{S}_i$ of the form

$$\mathbf{S}_i^T = I(1, q, u, v) \tag{7.35a}$$

is transformed into

$$\mathbf{S}_{out}^T = \tau I(1, aq, bu, cv) \tag{7.35b}$$

which implies that

$$\mathrm{DOP}_{out} = \sqrt{a^2q^2 + b^2u^2 + c^2v^2} \leq \sqrt{q^2 + u^2 + v^2} = \mathrm{DOP}_{in}. \tag{7.35c}$$

In the geometrical representation, the action of a depolarizer defined in (7.34) is to "pull" the representative point of the incoming Stokes vector toward the origin. As a result, the Poincaré sphere is transformed into an ellipsoid limited by the segments $[-a,a]$, $[-b,b]$, and $[-c,c]$ along the q, u, and v axes.

As discussed in Section 7.2.1.2, depolarization occurs due to incoherent addition of intensities of polarized states with different polarizations. In tissues, depolarization is due to multiple scattering in the first place, together with spatially varying linear birefringence in connective tissues [4]. However, these effects alone are not sufficient to cause "real" depolarization, but would give rise to a speckle pattern with DOP = 1 everywhere but with different polarizations from one point to another. "True" depolarization occurs if this speckle pattern is "blurred" by motion of the scattering sample, lack of spatial coherence of the illumination beam, sample motion (e.g., blood flow during *in vivo* measurements), and the like.

Depolarization is a *major polarimetric effect* in virtually all tissues (with the noticeable exceptions of eye cornea and aqueous and vitreous humors). In the absence of strong optical anisotropy, the tissue can be viewed as *a suspension of isotropic scatterers*. Then

- If the incident light is *linearly polarized* along the azimuth α, the reduction of DOP (also called the depolarization power) is independent of α. A necessary and sufficient condition for this is $a = b$ in Eq. (7.34). Moreover, as there is no reason why the azimuth of the "blurred" ellipse should change, a and b must be positive, and thus finally comprised between 0 and 1.
- If the incident light is *circularly polarized*, then the depolarization effect is described by the c diagonal term. This term is always positive in forward scattering, and also in the vast majority of cases of backward scattering, where the handedness is reversed with respect to the incident one, as it occurs for a reflection on a mirror [25]. However, c may sometimes take on negative values in other geometries, and more particularly in backward scattering [26].This unusual behavior may be observed when each individual scattering process takes place at small angles from the forward direction, and the overall backscattering process is dominated by "U turns" with large radii of curvature and circular polarizations which follow these turns "adiabatically" [27].

- There is no general relationship between $a = b$ and c. As discussed in more detail in Section 7.4.1.2 when the size of the scatterers is much smaller than the optical wavelength (Rayleigh scattering regime) then $a = b > |c|$, resulting in stronger depolarization for circularly than linearly polarized incident light. Conversely, when the scatterers are larger than the wavelength, the opposite holds ($a = b < c$). As a result, comparison of linear and circular depolarizing powers provides useful information about the average size of the scatterers. In practice, the vast majority of tissues behave as Rayleigh or Rayleigh-Gans scatterers [28–31], at least with respect to their polarization response.

In the most general case, the Mueller matrix of a depolarizer, $\mathbf{M}_\Delta$, is given in compact notation as [24]

$$\mathbf{M}_\Delta = \begin{pmatrix} 1 & \mathbf{0}^{\mathrm{T}} \\ \mathbf{0} & \mathbf{m}_\Delta \end{pmatrix}, \tag{7.36}$$

where $\mathbf{m}_\Delta$ is a 3×3 real symmetric matrix. This matrix can be diagonalized to recover the form given by Eq. (7.34) where the eigenvalues a, b, and c are real numbers varying between -1 and 1. Thus, the Mueller matrix of the most general depolarizer depends on *six parameters* (as it can be seen from the very definition of the $\mathbf{m}_\Delta$ matrix as a 3×3 symmetric matrix, or by the fact that the diagonalization process involves not only the three eigenvalues, but also the basis formed by the eigenvectors of $\mathbf{m}_\Delta$. General depolarizers are thus rather complex mathematical objects, this complexity being related to situations like multiple scattering in anisotropic media. Here we will not discuss the properties of general depolarizers any further, and in the following we will only consider depolarizers of the form given by Eq. (7.34). We thus define the depolarizing power of such samples as

$$\Delta = 1 - \frac{1}{3}(|a| + |b| + |c|) \tag{7.37a}$$

which can be further specialized in depolarizing powers for linear and circular polarizations as

$$\Delta_{\mathrm{L}} = 1 - \frac{1}{2}(|a| + |b|) \qquad \text{and} \qquad \Delta_{\mathrm{C}} = 1 - |c|. \tag{7.37b}$$

As a final remark, the depolarization powers Δ defined in Eqs. (7.35) and (7.36) vary from 0, for nondepolarizing samples, to 1 for totally depolarizing ones, while the opposite holds for the general depolarization index P_{d} defined in Eq. (7.11).

7.2.3 Decompositions into "Elementary" Component Matrices

Ideally, any polarimetric measurement, once obtained, should be interpreted by fitting to the measured Mueller matrices the results of numerical simulations based on a relevant model. Unfortunately this is not always possible, especially with complex

and/or disordered samples such as biological tissues. These exhibit depolarization in virtually all experimental conditions and have several of the above-described polarization effects occurring simultaneously, making accurate measurements *and* interpretation of the measured data difficult. The use of Mueller polarimetry followed by additional methods of results extraction and interpretation is thus essential in tissue studies.

It is thus desirable to develop and use novel approaches to "classify" and interpret the measured tissue Mueller polarimetry data, for example by determining its *retardance* and *depolarization* properties (in addition to the immediately and unequivocally accessible diattenuation and polarizance). Unfortunately, *retardance and depolarization cannot be uniquely determined from a given Mueller matrix*, except in very special cases of "pure" retarders or depolarizers.

The most usual way to process complex Mueller matrices then consists of *decomposing them into products of elementary matrices* with well-defined polarimetric properties and gleans quantitative parameters, meaning biophysical metrics from these. In the following, we first briefly list the form of these elementary matrices, and then outline the most commonly used procedures to decompose any Mueller matrix into various combinations (generally products) of elementary matrices. Note that these mathematical analysis methods do not imply that the sequence of polarization alterations, as described by a particular decomposition product, actually happens in tissue; rather, we are simply stating that the end result of the proposed decomposition sequence is "equivalent" to the experimentally measured one and lends itself to easier extraction of meaningful biophysical quantities.

Product decompositions thus represent an arbitrary Mueller matrix as a product of elementary Mueller matrices—diattenuators, retarders, and depolarizers. These decompositions are characterized by the number of elementary components and their respective positions in the multiplication. The order of the components is important since generally depolarizer matrices commute neither with diattenuator nor with retarder matrices. In principle, product decompositions are better suited to describe physical situations in which the beam interacts sequentially with different parts of the sample, each of which is characterized by a well-defined fundamental polarization property. Although this generally does not happen in biological tissues (where the effects more likely occur simultaneously), product decompositions have nevertheless been shown to yield accurate and reliable measures of tissue polarization properties.

7.2.3.1 Forward and Reverse Product Decompositions into Three Factors All these decompositions describe the input matrix $\mathbf{M}$ as a product of a diattenuator, a retarder, and a depolarizer. Actually with three elementary component types, there are six different possible orders that yield slightly different results, as in general, matrices do not commute [32]. Among these, the most widely used choice is that of Lu and Chipman [24]:

$$\mathbf{M} = \mathbf{M}_{\Delta P}\mathbf{M}_{R}.\mathbf{M}_{D}, \tag{7.38}$$

where the "special" symbol $\mathbf{M}_{\Delta \mathbf{P}}$ has been used for the depolarizer. Actually, for this decomposition to be quite general if $\mathbf{M}_{D}$ and $\mathbf{M}_{R}$ represent homogeneous

diattenuators and retarders, then the depolarizer cannot be a "pure" depolarizer of the form defined in Eq. (7.34), as the product matrix **M** would exhibit no polarizance and three parameters would be missing. As a result, in general the "depolarizer" has nonzero polarizance and its elementary matrix is of the form

$$\mathbf{M}_{\Delta \mathbf{P}} = \begin{pmatrix} 1 & \mathbf{0}^{\mathrm{T}} \\ \mathbf{P} & \mathbf{m}_{\Delta} \end{pmatrix}. \tag{7.39}$$

With these assumptions, the approach is numerically stable and always provides physically realizable elementary matrices $\mathbf{M}_{\Delta\mathbf{P}}$, $\mathbf{M}_{\mathrm{R}}$, and $\mathbf{M}_{\mathrm{D}}$. This procedure is thus very convenient and is widely used for the phenomenological interpretation of experimental (or even simulated) Mueller matrices. Moreover, its accuracy has been checked for well-characterized controlled systems (phantoms) as described in detail in Section 7.4.

What happens if the order of the elementary components is changed [32]? Simple matrix algebra shows that the above results are easily generalized to two out of the other five possible product sequences, namely those for which the diattenuator precedes the depolarizer:

$$\mathbf{M} = \mathbf{M'}_{\mathrm{R}}\mathbf{M'}_{\Delta\mathrm{P}}\mathbf{M'}_{\mathrm{D}} \text{ or } \mathbf{M} = \mathbf{M''}_{\Delta\mathrm{P}}\,\mathbf{M''}_{\mathrm{D}}\mathbf{M''}_{\mathrm{R}}. \tag{7.40}$$

More precisely, the depolarizer matrices keep the form defined in Eq. (7.39) and the $\mathbf{M'}$ and $\mathbf{M''}$ matrices are deduced from those provided by the standard decomposition (7.38) by unitary transformations.

This kind of simple generalization is no longer valid for the three remaining cases in which the depolarizer precedes the diattenuator. Morio and Goudail [33] introduced a "reverse" decomposition procedure for these three cases with the same definition of the depolarizer, but this procedure could lead to unstable or even unphysical results in case of very strong depolarizations. This issue has been solved by Ossikovski et al. [34] assuming that when the depolarizer precedes the diattenuator, the former features zero polarizance. The "standard" reverse decomposition takes then the form

$$\mathbf{M} = \mathbf{M}_{\mathrm{D}}\mathbf{M}_{\mathrm{R}}\mathbf{M}_{\mathrm{D'}\Delta}, \tag{7.41}$$

with a depolarizer matrix of the form

$$\mathbf{M}_{\mathbf{D'}\Delta} = \begin{pmatrix} 1 & \mathbf{D'}^{T} \\ \mathbf{0} & \mathbf{m}_{\Delta} \end{pmatrix}. \tag{7.42}$$

As in the case of "direct" decompositions defined by Eqs. (7.38) and (7.40), the matrices of the three possible "reverse" cases (with the depolarizer preceding the diattenuator) are deduced from one another by simple orthogonal transformations.

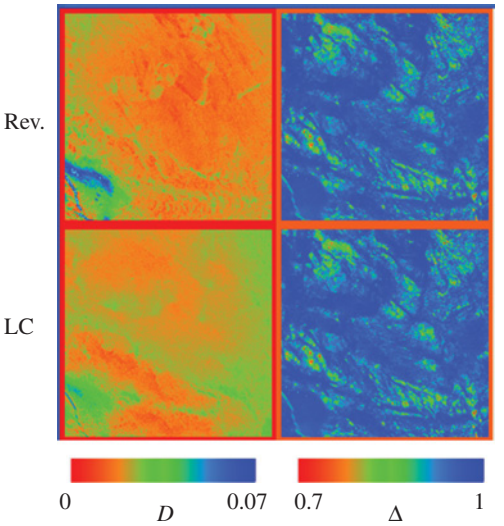

FIGURE 7.6 Polarimetric images of a pig skin sample in backscattering geometry taken at 600 nm. Field of view 5×5 cm^2. Top: diattenuation and depolarization images obtained with the reverse decomposition via Eq. (7.41). Bottom: diattenuation and depolarization images obtained with the Lu-Chipman decomposition. Color bars give the scales for scalar diattenuation D (left) and depolarization power Δ (right). Adapted from Reference 35. (*For a color version of this figure, see the color plate section.*)

The reverse decomposition procedure is also stable and always provides physically realizable Mueller matrices for the elementary components.

Figure 7.6 shows an example of the results provided by direct and reverse decompositions on a pig skin sample. The depolarization images are almost identical, which support the intuitive assumption that depolarization is due to multiple scatterings occurring *inside* the sample. Conversely, the diattenuation images are quite different for the two decompositions, the reverse one giving sharper details and larger absolute values. As the diattenuation is likely to be due to interface effects (diattenuation inside biological tissues is typically very small in the visible, as absorption is essentially due to hemoglobin, which is microscopically isotropic), the reverse decomposition apparently yield a better image of such effects, with a clearer correlation to the details of the depolarization image. These details are absent in the diattenuation image provided by the forward Lu-Chipman analysis (Eq. 7.38). The reverse decomposition seems *a priori* better suited to characterize the surface of such samples.

In summary, three-factor product decompositions may be very useful when studying turbid media, as they yield numerically stable and accurate information about the samples, provided these samples can be reasonably described as stacks comprising a depolarizer (typically the turbid medium), a retarder and a diattenuator in a given order. For isotropic tissues, the latter two effects are expected to occur essentially at the sample surface, while for samples like striated muscles birefringence is expected to arise from the bulk of the sample; consequently, three-factor decompositions may

not be necessarily well suited to all cases, a situation that justified the development of the alternative decompositions we outline in the following sections. In general though, it must be borne in mind that whatever decomposition approach is chosen, the claim is not that its physical embodiment is "what actually happens in tissue"; rather, this simply provides a mathematically "equivalent" framework that enables easier extraction of meaningful (and hopefully accurate) biophysical metrics that are contained but otherwise hidden in the complex Mueller matrix of biological tissues.

7.2.3.2 Symmetric Decomposition In symmetric decompositions, the input Mueller matrix $\mathbf{M}$ is decomposed into a product of *five* factors [36, 37]:

$$\mathbf{M} = \mathbf{M}_{D2}.\mathbf{M}_{R2}.\mathbf{M}_{d\Delta} \cdot \mathbf{M}_{R1}.\mathbf{M}_{D1}, \tag{7.43}$$

where $\mathbf{M}_{D1}$ and $\mathbf{M}_{D2}$ represent homogeneous diattenuators, $\mathbf{M}_{R1}$ and $\mathbf{M}_{R2}$ homogeneous retarders, and $\mathbf{M}_{d\Delta}$ a diagonal depolarizer as per Eq. (7.34). The central position of the depolarizer in the symmetric decomposition can be very useful for samples which can be viewed as purely depolarizing media bounded by tilted input and output interfaces: in this case the diattenuation and retardation effects are likely to occur at the output interfaces and the depolarization in between. Moreover, in many cases of practical interest the Mueller matrix of the depolarizer is indeed diagonal. However, the relevance of this decomposition for tissue polarimetry may be limited by two issues which may frequently in practice:

- As discussed in Section 7.2.2.4, the Mueller matrices of depolarizers consisting of spherical scatterers are diagonal (Eq. 7.34) with $a = b$. In presence of such "degeneracy" of the depolarizer eigenvalues, the Mueller matrices $\mathbf{M}_{R1}$ and $\mathbf{M}_{R2}$ of the retarders commute with $\mathbf{M}_{d\Delta}$ (i.e., $\mathbf{M}_{Ri}\mathbf{M}_{d\Delta} = \mathbf{M}_{d\Delta}\,\mathbf{M}_{R1}$) and thus cannot be unambiguously determined (only their product is unambiguous), and some *a priori* knowledge of these "retarders" is required. This issue has been raised in a work devoted to experimental validation of this decomposition [38].
- In contrast with the decompositions into three factors, the symmetric decompositions are not "universal," as there is a class of Mueller matrices, the so-called "non-Stokes diagonalizable" Mueller matrices, for which these decompositions cannot be applied. For such matrices there is one, and only one totally polarized input Stokes vector which retains its full polarization (DOP = 1) after transformation by the Mueller matrix [38, 39]. Analogous to the degenerate depolarizers, such matrices are not some artificial theoretical "curiosities," but do occur in nature (e.g., in scattering cholesteric structures such as shiny beetle cuticles, observed in backscattering [40]).

7.2.3.3 Logarithmic Decomposition The logarithmic decomposition was proposed recently as a complementary alternative to the standard product decompositions for spatially homogeneous systems where the polarimetric effects occur simultaneously and "continuously" during the propagation of light and not sequentially as

implied by the product approaches above. This decomposition is a natural generalization [41, 42] of the classic differential matrix formalism [43] applied to the depolarizing case. The approach, based on the physical picture of a continuously distributed depolarization, parallels and complements the product decomposition approach whereby depolarization is modeled as a spatially localized "lumped" phenomenon. In particular, the differential matrix methodology appears particularly well adapted to the phenomenological description of the scattering in turbid media such as biological tissues.

For a beam propagating along z, the Mueller matrix $\mathbf{M}(z + dz)$ is deduced from $\mathbf{M}(z)$ by

$$\mathbf{M}(z + dz) = \mathbf{U}(dz)\mathbf{M}(z) = [\mathbf{I} + \mathbf{m}dz], \tag{7.44}$$

where $\mathbf{I}$ is the identity matrix, $\mathbf{U}(dz)$ is the differential propagation matrix, and the differential matrix $\mathbf{m}$ can be defined in the most general case as

$$\mathbf{m} = \begin{pmatrix} \alpha & \beta'' & \gamma'' & \delta'' \\ \beta' & \alpha_1 & \mu'' & \nu'' \\ \gamma' & -\mu' & \alpha_2 & \eta'' \\ \delta' & -\nu' & -\eta' & \alpha_3 \end{pmatrix}. \tag{7.45}$$

Equation (7.44) can also be rewritten as

$$\frac{d\mathbf{M}}{dz} = \mathbf{m}\mathbf{M}. \tag{7.46}$$

Let us first assume that the medium is nondepolarizing and postpone the discussion of the effects of depolarization. Then it can be shown that $\mathbf{m}$ features additional transposition symmetries, namely $\beta' = \beta''$, $\gamma' = \gamma''$, $\delta' = \delta''$, $\mu' = \mu''$, and so on [37]. Then, the differential propagation matrix $\mathbf{U}(dz)$ takes the form

$$\mathbf{U}(dz) = [\mathbf{I} + \mathbf{m}dz] \approx (1 + \alpha dz) \begin{pmatrix} 1 & \beta dz & \gamma dz & \delta dz \\ \beta dz & 1 & \mu dz & \nu dz \\ \gamma dz & -\mu dz & 1 & \eta dz \\ \delta dz & -\nu dz & -\eta dz & 1 \end{pmatrix}, \tag{7.47}$$

which shows that αdz is simply the differential attenuation of unpolarized light over the distance dz. Moreover, due to the small size of the nondiagonal elements of $\mathbf{m}dz$ (due to the magnitude of dz itself), these elements describe the differential polarimetric effects due to the propagation over the distance dz as follows [43]:

- βdz is the differential linear diattenuation along the x–y laboratory axes.
- γdz is the differential linear diattenuation along the $\pm 45°$ axes.
- δdz is the differential circular diattenuation.
- ηdz is the differential linear retardation along the x–y axes.

- νdz is the differential linear retardation along the $\pm 45°$ axes.
- μdz is the differential circular retardation.

Another essential consequence of the smallness of the off-diagonal elements of the $\mathbf{U}(dz)$ matrices is that *they always commute* (provided dz is small enough). Indeed, a straightforward matrix calculation shows that to first order

$$\mathbf{U}_1(dz)\mathbf{U}_2(dz) = [\mathbf{I} + \mathbf{m}_1 dz][\mathbf{I} + \mathbf{m}_2 dz] = [\mathbf{I} + (\mathbf{m}_1 + \mathbf{m}_2)dz] = \mathbf{U}_2(dz)\mathbf{U}_1(dz) \quad (7.48)$$

In other words, the differential approach is well adapted to the propagation of light media featuring simultaneously various polarimetric properties, by eliminating the ambiguities related to the noncommutation of Mueller matrices describing finite instead of differential effects.

Note that in the general case of longitudinally inhomogeneous medium, $\mathbf{m}$ is a function of the propagation coordinate z (the direction of light propagation). If the medium can be considered homogeneous in the z direction over a distance L, expression (7.46) can be easily integrated to give

$$\mathbf{M} = \exp(\mathbf{m}\, L) = \exp(\mathbf{L}) \quad (7.48)$$

which can be also written as

$$\ln(\mathbf{M}) = \mathbf{m}\, L = \mathbf{L}. \quad (7.49)$$

This expression indicates that the fundamental properties of the medium under consideration, contained in $\mathbf{m}$, can be deduced from the logarithm of the related Mueller matrix if the total thickness L is known.

In the presence of depolarization, the matrix $\mathbf{m}$ takes its general form (7.45) and can be decomposed into a sum of two matrices

$$\mathbf{m} = \mathbf{m}_{\mathrm{m}} + \mathbf{m}_{\mathrm{u}}, \quad (7.50)$$

where $\mathbf{m}_{\mathbf{m}}$ has the same shape and symmetry properties as the $\mathbf{m}$ matrix defined in Eq. (7.45) (and is thus nondepolarizing). More specifically

$$\mathbf{m}_{\mathbf{m}} = \frac{1}{2}\begin{pmatrix} 2\alpha & \beta' + \beta'' & \gamma' + \gamma'' & \delta' + \delta'' \\ \beta' + \beta'' & 2\alpha_1 & \mu - \mu' & \nu - \nu' \\ \gamma' + \gamma'' & \mu' - \mu'' & 2\alpha_2 & \eta - \eta' \\ \delta' + \delta'' & \nu' - \nu'' & \eta' - \eta'' & 2\alpha_3 \end{pmatrix} \quad \text{and}$$

$$\mathbf{m}_{u} = \frac{1}{2}\begin{pmatrix} 0 & \beta' - \beta'' & \gamma' - \gamma'' & \delta' - \delta'' \\ \beta - \beta' & 0 & \mu' + \mu'' & \nu' + \nu'' \\ \gamma'' - \gamma' & \mu'' + \mu' & 0 & \eta' + \eta'' \\ \delta'' - \delta' & \nu'' + \nu' & \eta'' + \eta' & 0 \end{pmatrix} \quad (7.51)$$

Then $\mathbf{m_m}$ thus represents the mean values of the six elementary polarization properties, while $\mathbf{m_u}$ represents their respective uncertainties due to depolarization [41,42].

The elementary polarization properties of the medium can thus be directly determined from the logarithm $\mathbf{L}$ of the Mueller matrix $\mathbf{M}$, by constructing the Lorentz antisymmetric, $\mathbf{L}_{\mathrm{m}}$, and symmetric, $\mathbf{L}_{\mathrm{u}}$, components of $\mathbf{L}$ ($\mathbf{L} = \mathbf{L}_{\mathrm{m}} + \mathbf{L}_{u}$), respectively, as follows:

$$\mathbf{L}_{\mathrm{m}} = \frac{1}{2}(\mathbf{L} - \mathbf{G}\mathbf{L}^{\mathrm{T}}\mathbf{G}) \quad \text{and} \quad \mathbf{L}_{\mathrm{u}} = \frac{1}{2}(\mathbf{L} + \mathbf{G}\mathbf{L}^{\mathrm{T}}\mathbf{G}), \tag{7.52}$$

where $\mathbf{G} = \mathrm{diag}(1, -1, -1, -1)$ is the Minkowski metric tensor.

Apparently, for a depolarizing medium, the off-diagonal elements of $\mathbf{L}_{\mathrm{m}}$ represent the mean values of the six elementary properties accumulated over path length L, while the off-diagonal elements of $\mathbf{L}_{\mathrm{u}}$ express their respective uncertainties. Further, the main diagonal elements of the matrix $\mathbf{L}_{\mathrm{u}}(\alpha_1, \alpha_2, \text{and } \alpha_3)$ represent the depolarization coefficients (after the subtraction of the isotropic absorption α from the diagonal) along the xy, $\pm 45°$, and circular axes [42]. The accumulated polarization parameters (intrinsic properties integrated over the path length L) can be determined from the elements of the $\boldsymbol{L}_{\mathbf{m}}$ and $\boldsymbol{L}_{\mathbf{u}}$ matrices as

- **Integrated dichroism**

$$d = \sqrt{L_{\mathrm{m},12}^2 + L_{\mathrm{m},13}^2 + L_{\mathrm{m},14}^2}. \tag{7.53a}$$

- **Integrated depolarization**

$$\Delta = \frac{1}{3}|\alpha_1 + \alpha_2 + \alpha_3|. \tag{7.53b}$$

- **Linear retardation**

$$\delta = \sqrt{L_{\mathrm{m},24}^2 + L_{\mathrm{m},34}^2}. \tag{7.53c}$$

- **Optical rotation**

$$\psi = \frac{1}{2}L_{\mathrm{M},23}. \tag{7.53d}$$

- **Total retardation**

$$R = \sqrt{\delta^2 + 4\psi^2}. \tag{7.53e}$$

The corresponding uncertainties (standard deviations) of the parameters, diattenuation, linear retardance, and optical rotation (and total retardance) can also be derived employing the same set of equations (7.53) on the off-diagonal elements of the matrix $\boldsymbol{L}_{\mathbf{u}}$.

The conversion relationships between the medium polarimetry characteristics defined in the polar decomposition formalism (forward decomposition and its variants, reverse and symmetric decomposition) and those in the logarithmic decomposition (differential matrix formalism) also worth a brief mention here. In fact, the Mueller matrix corresponding to each accumulated polarization parameter (elements of the differential matrix $\mathbf{m}$ scaled by path length L) can be obtained from the solution of Eq. (7.46) and the eigenvalues of $\mathbf{m}$. These Mueller matrices for each of the individual polarization effects can be related to those defined in the polar decomposition formalism, to yield conversion from one set of parameters to the other:

$$D^{\log} = \tanh(d) = \tanh\left[\sqrt{L_{\mathrm{m},12}^2 + L_{\mathrm{m},13}^2 + L_{\mathrm{m},14}^2}\right] \leftrightarrow D^{\mathrm{pol}}, \tag{7.54a}$$

$$\Delta^{\log} = 1 - \frac{1}{3}(e^{-\alpha_1} + e^{-\alpha_2} + e^{-\alpha_3}) \leftrightarrow \Delta\mathrm{pol}. \tag{7.54b}$$

Note that the above two conversion relations, transforms *dichroism* into *diattenuation* (7.54a) and converts the three *logarithmic* depolarization coefficients into a single "conventional" net depolarization (7.54b). However, no such conversion is required for retardance.

The accuracy of this decomposition has been successfully tested with experimental Mueller matrices of phantoms consisting of dispersion of polystyrene microspheres in sucrose containing polyacrylamide and Monte-Carlo simulation, nematic liquid crystal plates [44] and adhesive tapes [42] and samples with diattenuators embedded in scattering and optically active media [45], to vary the commutation properties of the elementary polarization components. Some of these validation studies are discussed in Section 7.4.2.2.

7.2.4 Summary

In this section, we introduced the Stokes Mueller formalism, which provides a mathematically sound and physically intuitive description of all light polarization states, including partially polarized ones, which are particularly relevant for tissue polarimetry. The essential polarimetric properties, namely the diattenuation, the polarizance, the retardation, and the depolarization have been defined for "simple" polarimetric objects.

While Mueller matrices provide the most complete polarimetric characterization of any samples of interest, in vast majority of cases the most interesting information about these samples—such as those relevant to diagnostics for biological tissues for example—remain "hidden" in the 16 elements of the matrices. The decomposition procedures outlined in this part allow one to "extract" this information, provided the various decomposition procedures are used wisely.

On the one hand, each procedure is based on a specific description or representation of the sample, for example as a "stack" of simple elements following each other in a well-defined order (product decompositions). Of course, the parameters provided by

such procedures may be accurate only if the sample is actually of the form assumed by the decomposition, which is seldom the case. So the question then becomes whether the assumed physical representation implied by a specific mathematical decomposition can be considered as is "equivalent" to the original tissue? A "toolbox" of several procedures is then needed to decide how critical this issue really is, and how to cope with it.

Another important feature is the *stability* of the results. As a rule of thumb, the more factors are involved, the more unstable these factors may be for a given product (the initial Mueller matrix **M**). Commutation (multiplication order) issues may also arise, which may compromise the possibility to actually determine the values of some factors. For example, the stability and uniqueness of the solution provided by the three-factor decompositions (the Lu Chipman in its forward and reverse forms) is an advantage of these "simple" decompositions over the more complex symmetrical ones. This may explain why the former are the most widely used, even though they may provide only "effective" values of diattenuation, retardation, and depolarization in many cases, and all the more so in biological tissues.

In contrast, the logarithmic decomposition seems very appropriate to the characterization of tissues by its very definition, as these are turbid media with volumetrically "distributed" polarimetric properties (i.e., effects occur simultaneously and not sequentially as matrix multiplication/product decompositions imply). Moreover, this decomposition is intrinsically stable and has been successfully validated in several complex situations. One limitation, which may be overcome soon, is that if has been developed and tested only in the forward scattering direction, while for diagnostic purposes the backward geometry is typically more interesting and practical.

7.3 INSTRUMENTATION

A huge variety of polarimetric instruments have been developed, to meet the many different requirements related to the studied objects. In this part, we outline the general principles behind the design of polarimetric instruments, mention the various optical polarization components, and provide illustrative examples of actually used instruments, without attempting to be exhaustive.

7.3.1 General Principles

7.3.1.1 Overall Scheme of Polarimetric Instruments A generic polarimetric instrument is schematized in Figure 7.7. The light emitted by one (or possibly several) source(s) traverses a Polarization State Generator (PSG) and an illumination optical system (IO) which define the polarization state and other characteristics of the beam which impinges on the sample (Sp). The light emerging from the sample in a particular direction of interest (shown in transmission for illustration purposes in Figure 7.7) is then captured by another optical system (DO), traverses a Polarization State Analyzer (PSA) whose transmission depends on the light polarization, and is eventually detected by one (or possibly several) detectors (D). Though in

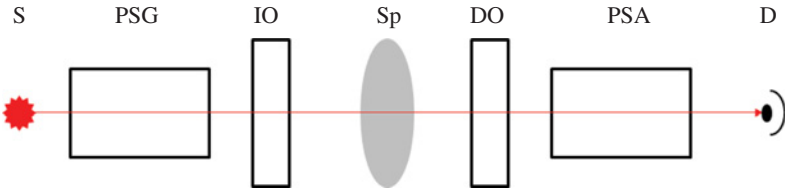

FIGURE 7.7 Block diagram of a generic polarimetric instrument. S, source(s); PSG, polarization state generator; IO, illumination optics; Sp, sample; DO, detection optics; PSA, polarization state analyzer; D, detector(s). Transmission geometry is illustrated above, but polarization analysis in many other detection directions is often possible and/or desirable.

practice the PSG, the PSA, and the other optics may overlap each other, either physically or conceptually, these elements are represented as separate as they play different roles.

The source(s) and detector(s) may be point-like or extended, and the other optics may implement full field imaging or pointwise measurements, the latter possibly with spatial scanning. Moreover, the instrument may be designed for single or multiple wavelength operation, with various requirements on acquisition speed or acceptable signal-to-noise ratio (SNR). Of course, the polarimetric elements composing the PSG and the PSA must also be chosen to satisfy the same requirements as the other optics. For example, their geometrical *étendue* and/or spectral bandwidth must be sufficient if full field imaging and/or multispectral operation are required. These issues will be briefly discussed later for various optical elements used for polarization studies.

7.3.1.2 Polarization Modulation and Analysis **Sequential polarization modulation and analysis.** Among the various schemes actually used for polarization modulation by the PSG and analysis by the PSA, the conceptually simplest is the modulation and analysis using discrete polarization basis states. In this scheme, the PSG sequentially generates m different polarizations, represented by m physical

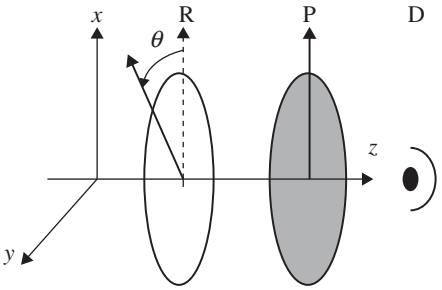

FIGURE 7.8 PSA based on a rotatable retarder (R) preceding a linear polarizer (P) and the detector (D). The pass axis of P is aligned along x, while the fast axis of the retarder makes a variable angle $\theta = \omega t$ with the x-axis.

Stokes vectors $\mathbf{S}_j$ incident on the sample, which can be considered as the columns of a real $4 \times m$ matrix, the *modulation matrix* $\mathbf{W}$. The PSG is said to be

- Incomplete if $m < 4$,
- Complete if $m = 4$ and the four Stokes vectors **S**j are linearly independent, meaning that the device correctly "samples" the whole polarization space. The 4×4 matrix $\mathbf{W}$ is then invertible.
- Redundant, if $m > 4$ and the **S**j vectors form a complete basis of the polarization space. In this case, the instrument "oversamples" this space, which is a possible way to reduce the noise or the systematic errors. In this case, the 4 x m $\mathbf{W}$ matrix possesses a pseudo-inverse.

Quite similarly to PSGs, a PSA can be characterized by its analysis matrix $\mathbf{A}$. When this PSA is illuminated by a light beam emerging from the sample whose Stokes vector is $\mathbf{S}$, it generates a set of n signals I_i (the eventually detected intensities), each of which is obtained by passing the light through a "polarization filter" described by a Stokes vector $\mathbf{S}'_i$. Mathematically this filtering corresponds to taking the scalar product of the incoming and the filter Stokes vectors:

$$I_i = \mathbf{S}'_i \cdot \mathbf{S}. \tag{7.55}$$

The I_i form a signal vector $\mathbf{I}$ of dimension n, related to the Stokes vector $\mathbf{S}$ emerging from the sample by

$$\mathbf{I} = \mathbf{A} \cdot \mathbf{S}. \tag{7.56}$$

In a way analogous to PSGs, PSAs may be incomplete, complete, or redundant depending on the dimension of the polarization space spanned by the line vectors $\mathbf{S}'_i$ of $\mathbf{A}$.

In a generic polarimeter as schematized in Figure 7.7, each Stokes vector $\mathbf{S}_j$ generated by the PSG is transformed into $\mathbf{MS}_j$, (where $\mathbf{M}$ is the Mueller matrix of the sample) and generates a corresponding signal vector $\mathbf{I}_j$. When the index j spans the range from 1 to m, these signal vectors form the columns of matrix $\mathbf{B}$, as for each of the incident PSG states the PSA produces n signals. The raw signal matrix can be written as

$$\mathbf{B} = \mathbf{A} \cdot \mathbf{M} \cdot \mathbf{W}. \tag{7.57}$$

Obviously, in order to retrieve useful information about $\mathbf{M}$ from the raw data $\mathbf{B}$, the matrices $\mathbf{A}$ and $\mathbf{W}$ must be known—the system must be *calibrated*. Moreover, provided both the PSG and the PSA are *complete* or *redundant* (i.e., the instrument is a Mueller polarimeter), the sample Mueller matrix $\mathbf{M}$ can be extracted from the raw data $\mathbf{B}$ by inverting Eq. (7.57):

$$\mathbf{M} = \mathbf{A}^{-1} \cdot \mathbf{B} \cdot \mathbf{W}^{-1}. \tag{7.58}$$

Periodic time modulation. If the PSGs and/or the PSA polarimetric properties vary periodically in time at angular frequency ω, for example due to the presence of rotating elements (see Figure 7.8), the detected signal(s) also vary periodically at the same frequency, allowing decomposition by Fourier analysis into harmonics; experimentally, this enables improved noise rejection and higher SNR via synchronous phase-sensitive detections (e.g., through lock-in amplification). The basis states of the PSG and/or the PSA are simultaneously encoded in different Fourier components if the detected signal(s). The modulation and analysis matrices of the PSG and the PSA are then defined in frequency (Fourier) space. We will not explicitly cover the (quite cumbersome!) equations giving a rigorous description of polarization encoding and/or detection in Fourier space, but a few simple examples of very widely used setups based on this scheme will be described in Section 7.3.2. Generally, temporal polarization modulation is easier to implement with point-like measurement systems, as detection schemes with imaging cameras are more challenging to modulate in synchrony.

Spectral or spatial modulation. The idea behind these schemes is quite similar to above. If the PSG and/or the PSA exhibit very fast (and well known!) variation of their characteristics with wavelengths while the Mueller matrix of the sample is constant or varies much more slowly, then the Fourier analysis of the signal can be realized in wavelength space. This scheme is very appealing in realizing "snapshot" spectroscopic polarimeters. The same idea may be applied for imaging applications, by imposing very fast variations of the polarization response of the PSA in the image plane, with subsequent Fourier analysis to extract the much more slowly varying polarization properties of the object under study.

7.3.1.3 Design and Optimization Considerations Here we address the following question, which is of importance when designing a complete polarimeter and has been widely discussed in the literature [46–52]; how can we use the degrees of freedom we have on the actual matrices $\mathbf{W}$ (through the judicious selection of PSG input states) and $\mathbf{A}$ (through the judicious selection of PSA filter states) for a given type of instrument *to minimize the noise on the final matrix* $\mathbf{M}$, *in the presence of additive noise on the raw data* $\mathbf{B}$?

We first discuss this issue for *complete* PSAs. Equation (7.56) can be rewritten as

$$\mathbf{I} = \mathbf{A} \cdot \mathbf{S} \qquad \Leftrightarrow \qquad \mathbf{S} = \mathbf{A}^{-1} \cdot \mathbf{I}. \tag{7.59}$$

If the raw measured intensity vector $\mathbf{I}$ is affected by an additive noise $\delta\mathbf{I}$, this noise will introduce an additive noise $\delta\mathbf{S}$ in the value of $\mathbf{S}$, given by

$$\delta\mathbf{S} = \mathbf{A}^{-1} \cdot \delta\mathbf{I}. \tag{7.60}$$

The rms noise on the raw data is nothing else but the usual Euclidean norm $\|\delta\mathbf{I}\|$ of $\delta\mathbf{I}$. With proper definition of the norm of matrices (the largest of their singular values), we get an upper bound of the noise on the $\mathbf{S}$ vector:

$$\|\delta\mathbf{S}\| \leq \|\mathbf{A}^{-1}\| \|\delta\mathbf{I}\|. \tag{7.61}$$

If the noise $\|\delta\mathbf{I}\|$ on the raw measurements does not depend on the exact configuration of the PSA, as is usually the case, a good criterion to optimize the design of a complete PSA consists *in minimizing the norm* $\|\mathbf{A}^{-1}\|$ [47].

Actually this criterion tells us that **A** is "as far as possible from singular" and thus is optimally conditioned to be inverted as required to extract **S** (which contains the information about the sample Mueller matrix **M**) from **I**. To achieve this optimization, the PSA basis states must be "as different as possible" from each other. For complete PSAs, this condition is achieved when the four basis states are at the tips of a regular tetrahedron on the Poincaré sphere [47]. This simple "geometrical" criterion can be generalized to the case of redundant PSAs, from which noise propagation is optimized when the basis states form simple symmetric polyhedra (such as an octahedron for $n = 6$, a cube for $n = 8$,and so on…) at the surface of the Poincaré sphere [52]. Moreover, when **A** is optimized, the noise on **S** is not only minimized, but it is also *most equally distributed among the various components of* **S** [48].

On the other hand, this general criterion may not be valid if one is interested in specific components of **S**, for which the noise can be minimized further at the expense of increasing it for other components (presumably less relevant in a particular application).

These results are easily generalized from PSAs to complete Mueller polarimeters: not surprisingly, the noise is minimized and most equally distributed on all **M** components if both $\|\mathbf{W}^{-1}\|$ and $\|\mathbf{A}^{-1}\|$ are minimized [49–51].

7.3.1.4 Complete versus Incomplete Instruments At first sight, one would assume that complete or redundant polarimeters are always superior to incomplete ones, as they are the only polarimeters able to provide full Mueller matrices upon mathematical analysis. However, for practical applications, complete Mueller polarimeters are not always the best choice, for two reasons:

1. Complete polarimeters are necessarily *more complex* than incomplete ones, and it may be difficult to make them compliant with demanding experimental requirements in terms of speed, spectral or angular bandwidth, and the like which may be imposed by the envisioned application.
2. If the polarimetric response of the sample under study is known to be of a s*pecific form*, then incomplete polarimeters may be *sufficient, and even better* than complete ones, as they can be designed to optimize the SNR and accuracy of the measurements of the Mueller matrix elements of interest.

The best practice, whenever possible, is to explore the polarimetric response of the samples of interest with complete instruments, and then, once the necessary polarimetric measurements are defined to make the device to be used in practice (e.g., for diagnostic purposes) as simple and rugged as possible.

As discussed below, for bulk biological tissues the "hierarchy" of the polarimetric effects is strong depolarization, modest linear birefringence, very weak optical activity (circular birefringence), and essentially nonexistent diattenuation/dichroism (either

linear or circular). In the absence of linear birefringence, tissues are essentially pure depolarizers, with diagonal Mueller matrices featuring typically $m_{22} = m_{33} \neq m_{44}$ (i.e., often (but not always!) linear depolarization is independent of orientation and is different from circular depolarization). Accurate determination of these elements can be done by incomplete polarimeters. On the other hand, if two of the three mentioned characteristics are simultaneously present (e.g., linear birefringence and depolarization, or depolarization and optical activity) and are of interest, then the determination of the full Mueller matrix and subsequent decomposition of this by the procedures outlined in Section 7.2 may be unavoidable.

7.3.2 Commonly Used PSAs

The many different designs for PSAs can be classified according to several possible criteria, with significant overlaps. Note that in principle, any PSA may be converted into a PSG (and the other way around) by interchanging the source(s) and the detector(s). In the following, after a short description of the usual polarization handling components, we present commonly used polarimetric PSAs, by increasing "complexity" starting from those based on simple linear polarizers.

7.3.2.1 PSAs Based on Linear Polarizers *Linear polarizers* are the most basic polarization handling components, and they are ubiquitous in polarimetric setups. In practice, these elements are of two main types:

- *Dichroic polarizers*, consisting of thin sheets of (typically plastic) materials which exhibit full absorption for one polarization and typically 70–85% transmission for the other. These polarizers typically feature quite broad angular acceptances, well adapted for imaging applications, but somewhat limited spectral bandwidths (the visible or the NIR for example).
- *Polarizing beam splitters,* which transmit two linear orthogonal polarization in different directions. These elements are made of complementary prisms of crystalline materials (Glan or Wollaston prisms) or glass with multilayer dielectric coatings. Crystalline beam splitters feature very wide spectral but rather narrow angular bandwidths while the opposite holds for glass beam splitters.

Sequential PSAs. As immediately obvious from the very definition of Stokes vectors (Eq. 7.7a), a *single linear polarizer coupled with a single detector* allows the determination of the I, Q, and U (but not V) components of the Stokes vector $\mathbf{S}$ of incoming light propagating along the z axis, provided the polarizer can be oriented sequentially along x, y, $+45°$, and $-45°$ in the transverse plane to provide the intensities I_x, I_y, I_P, and I_M, respectively.

PSAs with continuously rotating polarizers. Alternatively, if the polarizer rotates *continuously* at angular frequency ω, it transforms the Stokes vector $\mathbf{S}$ that traverses it into

$$\mathbf{S}'(t) = \mathbf{M}_{\mathrm{LD}}(1, 1, \omega t)\, \mathbf{S}, \tag{7.62}$$

where $\mathbf{M}_{\mathrm{LD}}(1, 0, \omega t)$ is the matrix of a linear diattenuator defined in Eq. (7.24) with $\tau = 1$ and $D = 1$ (perfect polarizer) oriented at $\theta = \omega t$. Equation (7.62) above can then be rewritten as

$$\mathbf{S}'(t) = \frac{1}{2}\begin{pmatrix} 1 & \cos 2\omega t & \sin 2\omega t & 0 \\ \cos 2\omega t & \cos^2 2\omega t & \cos 2\omega t \sin 2\omega t & 0 \\ \sin 2\omega t & \cos 2\omega t \sin 2\omega t & \sin^2 2\omega t & 0 \\ 0 & 0 & 0 & 0 \end{pmatrix}\begin{pmatrix} I \\ Q \\ U \\ V \end{pmatrix}. \tag{7.63}$$

The detected signal I_1 is the first component of $S'(t)$

$$I_1(t) = I + Q\cos(2\omega t) + U\sin(2\omega t) \tag{7.64}$$

from which I, Q, and U are immediately extracted by a straightforward *Fourier analysis*, as the amplitudes of the constant term and the two in-phase and quadrature components at frequency 2ω.

7.3.2.2 Combinations of Linear Polarizers and Constant Retarders *Constant retarders* are also very commonly found in polarimetric setups, to generate and analyze elliptically (circularly) polarized states. For these components, there are also two basic technologies:

- *Retardation plates*. These plates are slabs of birefringent materials (typically quartz or mica) which introduce a phase retardation $\Delta\phi = 2\pi \cdot Dn \cdot d/\lambda$ between their two orthogonal eigenpolarizations (Δn is the refractive index difference, d the plate thickness, and λ the wavelength). The natural dispersion of $\Delta\phi$ due to the $1/\lambda$ dependence can be reduced, around well-specified wavelengths, by assemblies of two plates with their slow axes at 90° to each other. Generally, the angular acceptance is rather small, except for very thin plates (called "true zero order" plates).
- *Fresnel rhombs*. These devices are based on the very achromatic phase retardation introduced by a total internal reflection between in-plane and out-of-plane polarizations. The spectral bandwidth may be huge (essentially equal to the transparency window of the material) but the angular acceptance is again very small. These components are thus very well suited to spectroscopic point-sensing polarimeters but present formidable challenges for imaging applications.

Sequential PSAs with a linear polarizer and a removable QWP. As noted above, linear polarizers alone cannot measure the V component of the incoming Stokes vector $\mathbf{S}$. The conceptually simplest way to address this limitation is to add to the measurements performed with the polarizer alone another two measurements performed with a QWP (a retarder with 90° retardation) with its axes set at ±45°

from those of the polarizer, to convert the linear polarizer into right and left circular polarizers. As a result, such a system may be operated

- *in redundant mode* [53], by taking into account the full set of six measurements (I_{x}, I_y, I_P, I_M, I_{L}, I_{R}) and solving the overdetermined system of six equations for the four unknowns I, Q, U, V (a particularly simple example of rectangular matrix **A**):

$$I_{\mathrm{x}} = I + Q, I_{\mathrm{y}} = I - Q, I_P = I + U, I_M = I - U, I_L = I + V, I_R = I - V, \quad (7.65)$$

- *in complete, nonredundant mode*, by skipping the measurements of I_{-45° and I_{R} and relying on the fact that the total intensity can be written as

$$I = I_x + I_y = I_P + I_M = I_L + I_R. \quad (7.66)$$

As mentioned earlier, the nonredundant scheme is obviously faster but the accuracy obtained with the redundant mode may be significantly better due to possible systematic errors which may be "averaged out" by increasing the number of measurements.

Sequential PSAs with a linear polarizer and a rotatable retarder set at discrete azimuths. In this kind of PSAs, the light to be analyzed passes through a rotatable retarder (R) and then a polarizer (P), which can be assumed to be aligned along the x axis without loss of generality. The light polarization is analyzed by recording the detected signal while the angle $\theta = \omega\, t$ between the fast axis of the retarder and the passing axis of the polarizer varies.

Upon reaching the detector, the Stokes vector **S** emanating from the sample of interest is transformed into

$$\mathbf{S}'(t) = \mathbf{M}_{\mathrm{LD}}(1, 1, 0)\, \mathbf{M}_{\mathrm{LR}}(\delta, \theta)\, \mathbf{S}, \quad (7.67)$$

where δ is the retardation of R. For a fixed value of δ, the detected intensity I_{D} varies as a function of θ according to

$$I_{\mathrm{D}}(\theta) = I + Q\left[\cos^2\frac{\delta}{2} + \sin^2\frac{\delta}{2}\cos 4\theta\right] + U\sin^2\frac{\delta}{2}\sin 4\theta - V\sin\delta\sin 2\theta \quad (7.68)$$

When the retarder azimuth sequentially takes n discrete values θ_{i}, the corresponding intensities are given by the formula above, which can be rewritten in matrix form to explicitly show the analysis matrix **A**:

$$\begin{bmatrix} I_1 \\ I_2 \\ .... \\ I_n \end{bmatrix} = \begin{bmatrix} 1 & \cos^2\frac{\delta}{2} + \sin^2\frac{\delta}{2}\cos\theta_1 & \sin^2\frac{\delta}{2}\sin 4\theta_1 & \sin\delta\sin 2\theta_1 \\ 1 & \cos^2\frac{\delta}{2} + \sin^2\frac{\delta}{2}\cos\theta_2 & \sin^2\frac{\delta}{2}\sin 4\theta_2 & \sin\delta\sin 2\theta_2 \\ ... & ... & ... & ... \\ 1 & \cos^2\frac{\delta}{2} + \sin^2\frac{\delta}{2}\cos\theta_n & \sin^2\frac{\delta}{2}\sin 4\theta_n & \sin\delta\sin 2\theta_n \end{bmatrix} \begin{bmatrix} I \\ Q \\ U \\ V \end{bmatrix}. \quad (7.69)$$

If $n = 4$, the PSA is complete provided δ is different from $p\pi$. Moreover, $\|\mathbf{A}^{-1}\|$ is minimized for $\delta = 132°$ and $\theta_{1,2} = \pm 51.7\,°$ and $\theta_{3,4} = \pm 15.1°$ [47]. The *a priori* surprising value of 132° stems from the criterion cited above: the basis states of the PSA must form a regular tetrahedron on the surface of the Poincaré sphere. It turns out that to do so, for example, a quarter wave is not sufficient: such a component would transform the initial linearly polarized state, into other states by rotations of 90° about various axes. As a result, these states would be confined to the same hemisphere as the initial linear state and would never form a regular tetrahedron. This does not mean that QWPs cannot be used in actual implementations of PSAs (and it is often the case in practice) but the noise in the final result may be slightly larger than with $\delta = 132°$.

PSAs with a linear polarizer and a continuously rotating retarder. As the retarder is continuously rotated at angular frequency ω, Eq. (68) above immediately shows that the only Fourier components with nonzero amplitudes are DC, $\sin(2\omega t)$, $\cos(4\omega t)$, and $\sin(4\omega t)$. Calling these amplitudes I_{DC}, $I_{\mathrm{S}2\omega}$, $I_{\mathrm{C}4\omega}$, and $I_{\mathrm{S}4\omega}$, we obtain their expression in function of $\mathbf{S}$ given in Eq. (7.70), which defines the analysis matrix $\mathbf{A}$ of the PSA in Fourier space. Again this matrix becomes singular for $\delta = p\pi$, as expected: in this case, the retarder is either half-wave and provides no sensitivity to the circularity component V; or "non-existent" (if p is an even integer) and the PSA reduces to a fixed linear polarizer. Analogous to above, $\mathbf{A}$ is optimal for $\delta = 129°$:

$$\begin{bmatrix} I_{\mathrm{DC}} \\ I_{\mathrm{S}2\omega} \\ I_{\mathrm{C}4\omega} \\ I_{\mathrm{S}4\omega} \end{bmatrix} = \begin{bmatrix} 1 & \cos^2\left(\frac{\delta}{2}\right) & 0 & 0 \\ 0 & 0 & 0 & -\sin\delta \\ 0 & \sin^2\left(\frac{\delta}{2}\right) & 0 & 0 \\ 0 & 0 & \sin^2\left(\frac{\delta}{2}\right) & 0 \end{bmatrix} \begin{bmatrix} I \\ Q \\ U \\ V \end{bmatrix}. \tag{7.70}$$

Practical considerations. PSAs and PSGs comprising a linear polarizer and a rotatable retarder (often improperly called "compensator") achieve complete polarization generation and analysis with only two passive polarization elements. Due to this simplicity, they are very widely used, with the two operation modes outlined above, with the retarders rotating either stepwise (discretely) or continuously:

- Continuous rotation is usually preferred when the detector is fast enough, which is usually the case for *pointwise measurements* requiring a single photodetector or *spectroscopic measurements* with one-dimensional CCD arrays at the focal plane of a spectrometer. In this latter case, the retarders must be reasonably achromatic, like Fresnel rhombs or, to a lesser extent, "achromatic" retardation plates made of stacks of elementary birefringent plates. Compared to stepwise rotation, continuous retarder rotation is easier to implement and provides shorter measurement times. However, in this configuration the PSG and the PSA cannot be optimized independently of each other, due to possible "mixing" of the Fourier components encoding the various polarization basis states.

A typical choice is to rotate the PSG and PSA retarders at frequencies 3ω and 5ω [50, 54].

- Conversely, stepwise rotation may be better suited for polarimetric *imaging* applications, typically with two-dimensional CCDs. In this scheme, prior to each image acquisition the retarders are set at the prescribed couple of azimuths and left still during the camera integration time, until the full set of $n \times m$ raw images are taken. For this polarimetric imaging, it is essential to use retarders with wide enough angular acceptances. Image "wander" is frequently observed in relation with retarder rotation, and must be corrected for by suitable imaging treatment/analysis procedures.
- Continuous retarder rotation and Fourier analysis of the signal would be possible with two-dimensional CCDs, only for extremely fast CCDs (both in acquisition and data transmission) and would require large computational power. A practically easier alternative would involve stroboscopic illumination, synchronized with the polarization modulation. This approach has already been implemented for partial polarimetric measurements [55] but not for complete Mueller polarimetry.

7.3.2.3 Combinations of a Linear Polarizer and Variable Retarder(s) Historically, the first variable retarders were the Babinet Soleil compensators, made of two crystalline wedges which could slide with respect to each other, and which were equivalent to a single birefringent crystal with variable thickness. Though still in use, these devices have been largely replaced by others, of the two following types:

- *Pockels cells*. In these elements, a driving voltage is applied to two or four suitably oriented crystals, to modify their birefringence, and the resulting retardation between two linear orthogonal eigenpolarizations. These devices typically exhibit very fast time responses (in the nanosecond range, if a suitable voltage driver is used), but they require high driving voltages ($\sim$200 V for $\Delta\phi = 180°$ in the visible) and exhibit very small spatial and angular apertures. In practice these devices can be used only with laser beams, and thus are included in PSGs (but generally not in PSAs) when studying highly scattering samples like thick tissues.
- *Photoelastic modulators*. These devices consist of a slab of glass (typically fused silica) about 10 cm long. Piezoelectric transducers generate a sound wave at frequency ν, which, in turn, creates a time dependent birefringence in the glass slab at the same frequency ν, which can be used to modulate the polarization of a passing light beam at ν and its harmonics 2ν, 3ν... This effect is usable if ν is a sonic resonant frequency of the glass bar. Such resonances, extremely narrow, typically lie around 50 kHz. As a result, polarimeters with photoelastic modulators are typically operated with synchronous detection locked on the modulator excitation and/or its harmonics. Such high frequency modulation schemes reduce the $1/f$ and other noise sources thereby increasing the SNR, an advantage which may be crucial when the available signal is low. This

scheme is typically realized electronically with single point-sensing detectors, but it can also be implemented optically, with a stroboscopic illumination of the polarimeter to "freeze" the polarization at specific phases with respect to the modulator excitation.

- *Liquid crystals cells*. In these components, a very thin (∼10 μm thick) layer of nematic liquid crystal is "sandwiched" between two glass plates with transparent electrodes. AC driving voltages up to 20 V are sufficient to modulate the retardation over 360° or more. The angular acceptance of these devices is very large (tens of degrees), making them very well suited for imaging applications. On the other hand, the time response is slow (several tens of milliseconds) for a significant shift in retardation. The spectral range is also limited to the visible and the near infrared.

Polarizer and one variable nonrotating retarder. As these elements are typically set at azimuths 45° apart from each other, we will assume without loss of generality that the retarder is aligned along the x axis, and the polarizer at 45° without loss of generality, as shown in Figure 7.9. The incoming Stokes vector $\mathbf{S}$ is transformed by the variable retarder VR and polarizer into

$$\mathbf{S}'(t) = \mathbf{M}_{\mathrm{LD}}(1, 1, 45°)\, \mathbf{M}_{\mathrm{LR}}(1, \delta(t), 0)\, \mathbf{S}, \tag{7.71}$$

where $\delta(t)$ is the time-dependent retardation of the VR. The detected intensity is now

$$I_{\mathrm{D}}(t) = \frac{1}{2}(I + U\cos\delta(t) - V\sin\delta(t)) \tag{7.72}$$

and does not depend on Q at all. This result is general: a PSA for which the only variable parameter is the retardation of a VR set at constant azimuth is never complete.

Thus, the measurements provided by this setup have to be completed by other measurements for Mueller matrix determination, for example, via a removable QWP

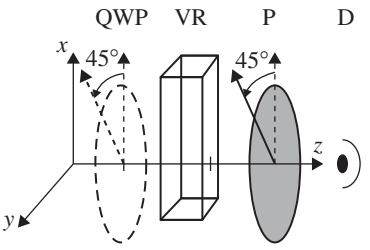

FIGURE 7.9 Scheme of a PSA composed of a variable retarder (VR), a polarizer (P), and a detector (D). The VR has its fast and slow axes aligned with x- and y-axes, respectively, and its retardation is varied to analyze the incoming beam polarization. The measurements are performed with and without the removable QWP to allow complete determination of the incoming beam polarization.

in added at the entrance of the device. With this additional component, Eq. (7.71) becomes

$$\mathbf{S}'(t) = \mathbf{M}_{\mathrm{LD}}(1, 1, 45°)\ \mathbf{M}_{\mathrm{LR}}(1, \delta(t), 0)\ \mathbf{M}_{\mathrm{LR}}(1, 90°, 45°)\mathbf{S} \tag{7.73}$$

which transforms the detected intensity into

$$I_{\mathrm{D}}^{\mathrm{QW}}(t) = \frac{1}{2}\left(I - Q\sin\delta(t) + U\cos\delta(t)\right) \tag{7.74}$$

and thus completes the determination of $\mathbf{S}$ when the retardation $\delta(t)$ is varied to define the analysis matrix $\mathbf{A}$. As mentioned above, the temporal evolution of δ may be essentially arbitrary for nonresonant devices like Pockels cells or liquid crystals. For resonant devices like photoelastic modulators, the retardation varies sinusoidally in time:

$$\delta(t) = \delta_0 \sin\omega t. \tag{7.75}$$

The Fourier expansions of the functions $\cos(\delta_0 \sin\omega t)$ and $\sin(\delta_0 \sin\omega t)$ are well known. Keeping the first three terms (DC, ω, and 2ω frequencies), we obtain

$$I_{\mathrm{D}}(t) = \frac{1}{2}(I + U[J_0(\delta_0) + 2J_2(\delta_0)cos2\omega t] - V[2J_1(\delta_0)sin\omega t]), \tag{7.76}$$

$$I_{\mathrm{D}}^{\mathrm{QW}}(t) = \frac{1}{2}(I - Q[2J_1(\delta_0)sin\omega t] + U[J_0(\delta_0) + 2J_2(\delta_0)cos2\omega t]), \tag{7.77}$$

where J_{n} are Bessel functions. The Fourier components at zero, ω, and 2ω frequencies are the relevant quantities for the synchronous detection scheme generally used to optimize the SNR. Analogous to the rotating retarder scheme, the expressions above can be recast in terms of the system analysis matrix $\mathbf{A}$, which is then redundant, with six measured quantities (I_{DC}, $I_{\mathrm{S}\omega}$, $I_{\mathrm{C}2\omega}$, and the like with the QWP inserted) for the four components of $\mathbf{S}$.

Polarizer and two nonrotating variable retarders. This type of PSA is schematized in Figure 7.10. The incoming light traverses two variable retarders, whose fast axes are set at constant azimuths θ_1 and θ_2 from the x axis, then again a linear polarizer set along x before being detected. The Stokes vector $\mathbf{S}'$ of the light reaching the detector is now

$$\mathbf{S}'(t) = \mathbf{M}_{\mathrm{LR}}(1, \delta_2, \theta_2)\ \mathbf{M}_{\mathrm{LR}}(1, \delta_1, \theta_1)\ \mathbf{S}. \tag{7.78}$$

The calculation is quite similar to the previous ones and will not be reproduced here. The main result is that by varying the retardations δ_1 and δ_2, it is easy to make *this device a complete PSA*, provided the orientations θ_1 and θ_2 are properly chosen. Actually, *the best choice* is $\theta_1 = 0°$ and $\theta_2 = 45°$, as any arbitrarily chosen elliptical "polarization filter" can be obtained by adjusting the retardations. This property is

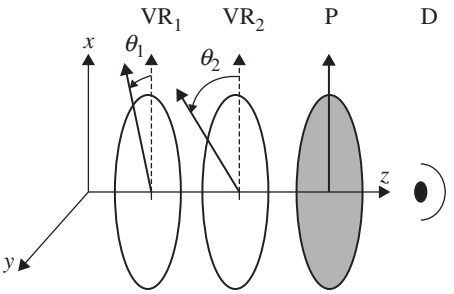

FIGURE 7.10 PSA composed of two variable retarders (VRi), a polarizer (P), and a detector (D). The VR fast and slow axes are set at azimuths θ_1 and θ_2 with respect to the x axis and their retardations δ_1 and δ_2 are varied in time to analyze the incoming beam polarization.

also valid when the device is used as a PSG, with a source replacing the detector and the light travelling in the $-z$ direction: such a PSG can generate *any* predefined Stokes vector **S**.

Such versatility is not really needed to make complete Mueller polarimeters: as long as the PSG and the PSA are each able to generate four linearly independent basis states, complete measurements are possible (**W** and **A** are invertible). However, potential SNR improvements inherent in no-moving-mechanical-part polarimeters (often with synchronous detection schemes) offer significant advantages in low-signal situations often encountered in biomedicine. Further, the possibility to generate *any* state by the PSG and to project the emerging state on *any* polarization state at the PSA opens interesting possibilities for polarization contrast optimization of different

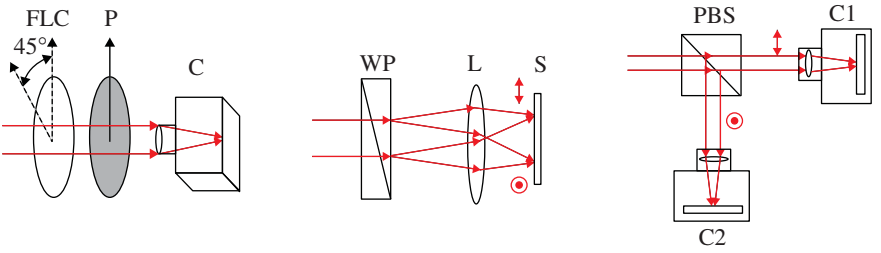

FIGURE 7.11 Three PSA setups implemented for OSC imaging. Left: a sequential PSA. The incident beam traverses a ferroelectric liquid crystal (FLC) equivalent to a half wave plate which can be rapidly switched between two azimuths separated by 45°, and a linear polarizer (P) before reaching the camera (C). This system allows sequential acquisition of the orthogonally polarized images with switching times less than 1 ms [58]. Center: the incoming beam is separated into two beams with orthogonal polarizations by the Wollaston prism (WP), to form two polarized images on the sensor (S) via the lens (L) [59]. Right: the two orthogonal polarizations are separated by the polarizing beam splitter (PBS) and form two images on two separate cameras C1 and C2 [60].

tissue states to be distinguished from each other (e.g., cancerous and noncancerous tissues) without measuring the full Mueller matrices [56, 57].

7.3.3 Examples of Tissue Polarimetry Instruments

In this part, we illustrate the above considerations by giving some examples of polarimetric instruments, without attempting to exhaustively describe the very wide variety of such devices which have been successfully implemented.

7.3.3.1 Orthogonal State Contrast Imagers Orthogonal state contrast (OSC) imaging (which has also been called, somewhat improperly, DOP imaging) is quite a simple, and thus experimentally very appealing polarimetric characterization technique, whenever applicable. In this modality, the sample is illuminated with linearly polarized light and imaged with two polarization filters, one parallel and one perpendicular to the illumination polarization. The two images, $I_{\parallel}$ and $I_{\perp}$, are then combined to form the OSC image:

$$I_{\mathrm{OSC}} = \frac{I_{\parallel} - I_{\perp}}{I_{\parallel} + I_{\perp}}. \tag{7.79}$$

The OSC contrast is independent of the overall reflectivity of the sample (within the limits imposed by the instrumental dynamical range!) and thus a purely polarimetric characterization technique (the tissue reflectance $(I_{\parallel} + I_{\perp})$ can be studied independently). Moreover, for isotropic pure depolarizers, as may be true for many biological tissues, OSC directly provides the elements $m_{22} = m_{33}$ of the sample-normalized Mueller matrix, which define the tissue depolarizing power for linearly polarized light. Of course, OSC can also be implemented with co- or counter-oriented circular polarizations, and then it provides m_{44}.

An OSC imager thus comprises a linearly polarized source, and a PSA able to provide images with two linear orthogonal polarizations as efficiently as possible. Three schemes of such PSAs have been described in the literature and are outlined in Figure 7.11. In the first scheme (*left panel*), the acquisition of the two polarized images is realized sequentially, by "optically rotating" the linear polarizer by means of a liquid crystal cell with constant half wave retardation whose orientation can be switched between two azimuths 45° apart from each other in less than 1 ms. With so fast a polarization modulation, the time needed to take both polarized images is determined solely by the CCD speed and the integration time necessary to reach a good SNR. Such a device has been used on a colposcope for *in vivo* examination of uterine cervix at 10 fps for the OSC images [58]. In the second scheme (*center panel*), the two polarizations are separated by means of a Wollaston prism and two images are formed simultaneously on the CCD sensor (S) in the focal plane of the lens (L) [59]. The third scheme (*right panel*) makes use of a polarizing beam splitter (PBS) and two separate cameras to take the polarized images. In the last scheme, the polarized images are taken simultaneously at video rates, but there may be issues

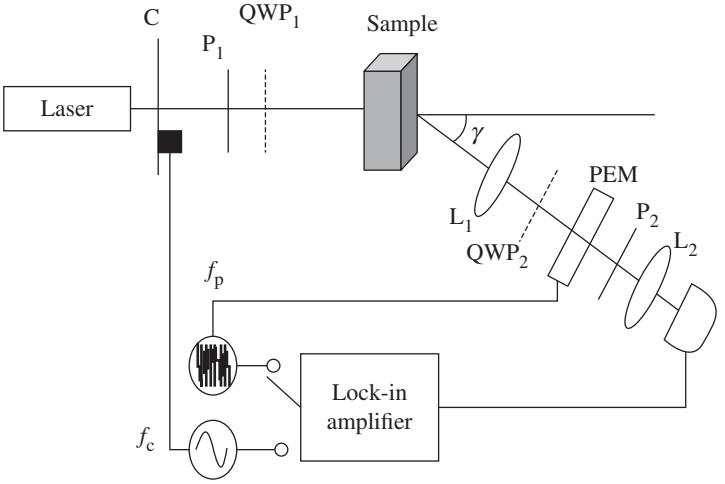

FIGURE 7.12 Highly sensitive complete Mueller point-sensing polarimeter. The PSG comprises a linear polarizer and a removable quarter-wave plate (QWP) while the PEM-based PSA is of the type described above. f_c and f_p are the chopper and PEM modulation frequencies, respectively. γ is the detection angle. Adapted from References 61 and 62.

with *misregistration*, that is, unavoidable shifts in the pixel-to-pixel correspondence of identical points in the optical images.

7.3.3.2 A nonimaging Mueller Polarimeter A complete point-sensing polarimeter combining a PSG with a polarizer and a removable QWP and a PSA based with a photoelastic modulator as described above is shown in Figure 7.12.

To boost the SNR as much as possible in this arrangement, the illuminating laser is chopped (at the sub kHz range, f_c) to allow synchronous detection of the "DC" component, in addition to that of the signals modulated by the PEM at ω (50 kHz, f_p) and 2ω (100 kHz).

7.3.3.3 Complete Mueller Imagers In both examples shown below, the polarimetric images are taken with a CCD. Of course imaging can also be achieved by using a single detector and a spatially scanning laser beam.

Dual rotating retarders. In these instruments, the PSG and the PSA both comprise a linear polarizer and a rotating retarder. An example of such an instrument is shown in Figure 7.13. As mentioned above, in such setups the rotatable retarders are sequentially set at discrete azimuths and are kept fixed for each raw image acquisition by the CCD. As acquisition of full Mueller images can take tens of seconds these instruments are well suited to the characterization of static samples.

Pairs of variable retarders. The instrument shown in Figure 7.14 is the Mueller imager developed at Ecole Polytechnique, for examination of *ex-vivo* tissue samples. Both the PSG and the PSA are of the type outlined in Figure 7.10 with nematic liquid crystals as non-rotating variable retarders.

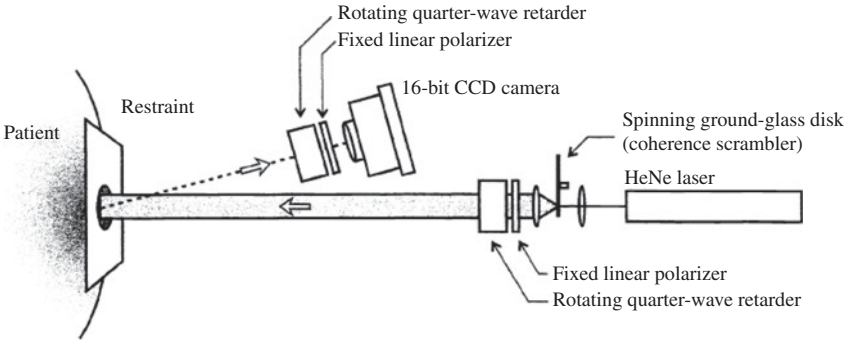

FIGURE 7.13 Mueller imager with PSG and PSA, each comprising of a polarizer and a rotating retarder set sequentially at discrete azimuths for image acquisition by the CCD. From Reference 63.

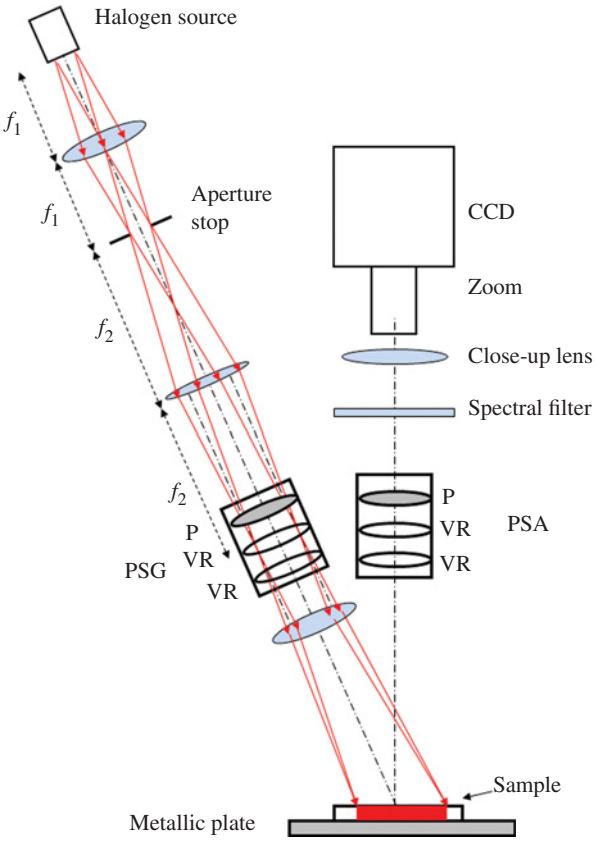

FIGURE 7.14 Mueller imager for examination of *ex-vivo* samples. The PSG and PSA are both made of a linear polarizer and two VR making use nematic liquid crystals at fixed orientations. The retardations of each of the four VRs are switched discretely between pairs of different values to generate the 16 polarization basis states. The illumination system is designed to ensure that the polarizations defined by the PSG are uniform over the entire 5×5 cm^2 field of view. Adapted from Reference 64.

Nematic liquid crystals feature very wide angular acceptance, no image motion when retardance is changed, and a time response typically less than 100 ms. Full Mueller images are then acquired in a few seconds by sequentially switching the retardations of each of the four VRs between pairs of suitably chosen values and leaving these retardations constant during the CCD integration time. By using a white light source (halogen lamp) and interference filters, the wavelength can be selected at will throughout the visible spectrum to enable spectral polarimetry studies.

7.3.4 Summary

In this section, we briefly reviewed the basic principles of design and optimization of polarimetric instrumentation, and outlined the most widely used practical implementations. These may take a variety of forms, depending on the selected optical systems (imaging or non-imaging) and the way the polarization is encoded and detected (in discrete states, or in Fourier components of periodically varying systems such as photoelastic modulators). The availability of so many possibilities is very valuable in practice, as it allows one to "tailor" the polarimetric system for the specific needs of the envisioned application. In particular, polarization modulation and detection may be "added" to virtually any optical system, at the microscopic as well as macroscopic levels; note that this is not the case for many other techniques widely used in biomedicine, such as confocal imaging or OCT, which operate only at microscopic scales. Last but not least, often polarimetry may be implemented at very reasonable cost, an essential point for many possible practical applications.

7.4 FORWARD MODELING AND TESTING IN PHANTOMS

7.4.1 Forward Modeling of Polarized Light Propagation in Tissue

7.4.1.1 Overview As outlined in the introduction, tissue polarimetry research has two major application directions:

(a) *Polarized light tissue imaging,* wherein polarization can be used as a gating mechanism to filter out multiply scattered (image blurring) photons in order to enhance contrast and to improve imaging resolution; and
(b) *Tissue characterization/diagnosis*, wherein the rich abundance of important biophysical information contained in the intrinsic tissue polarimetry characteristics (retardance, diattenuation, and depolarization encoded in the tissue Mueller matrix) are extracted and quantified.

For either, accurate modeling of interaction of polarized light with biological turbid media or tissue is extremely useful. The insight gained from such *forward models* helps in designing and optimizing experiments, and analyzing/interpreting measured data for specific applications.

Driven by the two different classes of applications, forward modeling of polarized light transport in tissue also has takes different routes. For the tissue imaging applications, the major emphasis has been on *modeling depolarization of multiply scattered light* in turbid media. In these analytical/heuristic approaches, the tissue is typically modeled as a turbid medium having bulk-average scattering and absorption properties, where propagation leads to depolarization as a result of strong multiple scattering events (birefringence and other simultaneously occurring polarization effects are often ignored) [1, 65–69]. The main aim of these models has been to understand the overall depolarization trends, its dependence on the scattering properties of the media (density, size, shape, and refractive index of the scatterers), and on the incident state of polarization, and to design/optimize general polarization schemes to discriminate against multiply scattered photons for tissue imaging in "simple" geometries.

Applications involving extraction/quantification of the intrinsic tissue polarimetry characteristics for tissue characterization and assessment, on the other hand, require more accurate and complete forward models incorporating the simultaneously exhibited complex tissue polarimetry and scattering events [3]. Nevertheless, for either of the aforementioned approaches, rigorous electromagnetic (EM) theory based models for analyzing polarized light propagation in tissue has not been feasible. This is because the Maxwell's equations-based EM theoretical approach will need to identify and incorporate the spatial/temporal distribution of complex tissue dielectric structures (different cells and subcellular structures, connective stromal tissues/extracellular matrix, blood and lymphatic networks, interstitial fluids, etc.), which is clearly a formidable (if not impossible) task.

Instead, light propagation through such media is often modeled using the *radiative transport theory* [70]. Although the scalar radiative transport theory and its simplified approximation, the diffusion equation, have been successfully used in tissue optics (specifically to yield light intensity distribution in tissue volume and measurable quantities such as diffuse reflectance, transmittance, spatially resolved diffuse reflectance and so on), both are intensity-based techniques, and hence typically neglect polarization [1, 70]. Alternatively, the vector radiative transfer equation (VRTE), which includes polarization information by describing transport of the Stokes vectors of light (photon packet) through a random medium, has been explored for tissue polarimetry modeling [1]. However, solving the VRTE in real systems is rather complex and the solutions are often too slow and insufficiently flexible to handle the necessary boundary conditions for arbitrary geometries, heterogeneities, and optical properties as desirable in case of tissue.

The *polarization sensitive Monte Carlo* (PSMC) *technique* is a more general and robust approach that overcomes these limitations [70, 71]. The PSMC technique has thus been widely explored for tissue forward modeling, specifically for applications involving tissue characterization/diagnosis as described in greater detail subsequently. For polarized light imaging applications, relatively simpler analytical/heuristic approaches based on photon diffusion formalisms [68], random walk models [69], and maximum entropy principles [65] have proven moderately successful. In the following, we provide a very brief account of some of these simpler

analytical approximations developed to deal with depolarization of multiply scattered light in turbid medium. Interested readers are referred to References 1, 65–69 for further details.

7.4.1.2 Modeling Depolarization of Multiply Scattered Light: Photon Diffusion Formalism As noted, these simpler analytical theories are aimed at deriving relationships between various quantities of practical interest such as the DOP (either linear or circular) of forward-scattered or back-scattered light from a turbid medium, average path lengths, the optical transport parameters of the medium, and so forth. As in the case of radiative transport theory, in these models also, the turbid medium is considered to have *bulk-average scattering and absorption properties*, representative of isotropic tissue volumes. The turbid medium is usually modeled through the optical transport parameters, namely, the *absorption coefficient* (μ_a), *single scattering coefficient* (μ_s), and s*ingle scattering anisotropy* (g) [70]. As is known from the transport theory, the linear isotropic optical coefficients are defined so that

$$l_a = \mu_a^{-1} \qquad \text{and} \qquad l_s = \mu_s^{-1} \tag{7.80}$$

give the absorption and scattering mean free paths, respectively.

The anisotropy parameter g is defined as the average cosine of scattering angle. The value of g ranges from –1 to +1, where $g = -1$ corresponds to fully backward scattering, $g = 0$ corresponds to forward-backward symmetric scattering (isotropic scattering being a special case) and $g = +1$ corresponds to fully forward scattering. In general, the value of g depends on the average size of the scatterers in the medium relative to the wavelength of the irradiation. For a medium composed of scatterers whose size is much smaller than the wavelength (radius $a \ll \lambda$), the anisotropy parameter g is ~0, its value approaching unity ($g \sim 1$) for media composed of larger sized scatterers ($a \geq \lambda$). The latter regime applies to most biological tissues in the visible/near-infrared spectral range ($g \sim 0.7$–0.95) [70].

Another couple of parameters frequently used in tissue optics are

$$\mu_s^{/} = \mu_s(1 - g) \text{ and } l^* = (\mu_s^{/}) - 1 \tag{7.81}$$

namely, the reduced scattering coefficient and the transport mean free path. Because of typical tissue g-values, $1 - g$ is a small number, and thus $\mu_s > \mu_s^{/}$ and $l^* > l_s$. The use of μ'_s assumes that the reflection and transmission for a slab of tissue with optical parameters μ_a, μ_s, and g are the same as those for the same slab with optical parameters μ_a, $\mu_s^{/}$, and $g = 0$ [70]. This so-called *similarity principle* is not exact and holds if the light distribution is studied far enough away from the light source and boundaries, typically at a distance greater than l^*, which in turn is referred to as the typical length scale over which the propagation direction of photons gets randomized in a multiply scattering medium.

In the photon diffusion formalisms, the depolarization of multiply scattered light is usually modeled by assuming an exponential decay of the single path (photon undergoing successive scattering events) DOP with increasing number of scattering

events (n). Analytical expressions for depolarization via the characteristic depolarization length scales ξ_L and ξ_C (for linear and circular polarizations, respectively) has also been derived based on the so-called *maximum entropy principle* [1, 65]. The degree of residual polarization of multiply scattered light at a chosen detection point can be obtained by averaging (or weighing) the single path DOP over the path length distribution function.

Approximate analytical expressions for the path length distribution function are conveniently obtained from the solution of photon diffusion equation for a given detection geometry [1, 70]. The resulting DOP $\mathrm{DOP}_{L,C}$ of diffusely transmitted or reflected light from a turbid medium for two practical geometries, the forward scattering and the backscattering geometries, has accordingly been derived for linear and circular polarizations:

- ***Forward scattering geometry, slab of thickness L***

$$\mathrm{DOP}_{L,C} \cong 2\frac{L}{l_s}\sinh\left[\frac{l_s}{\varsigma_{L,C}}\right]\exp\left[-\frac{L}{\varsigma_{L,C}}\right] \tag{7.82a}$$

  where l_s is the scattering mean free path defined in Eq. (7.80), and

$$\zeta_{L,C} = \left[\frac{1}{3}l_s\xi_{L,C}\right]^{\frac{1}{2}}, \tag{7.82b}$$

  where $\xi_{L,C}$ is the characteristic depolarization length scales for linear and circular polarizations. These lengths are defined as the average distances a (linearly or circularly) polarized photon has to go through in the medium to see its DOP decrease by a factor of e. The ratios ξ_L/l_s and ξ_C/l_s thus define the average number of collisions required to reduce the DOP by a factor of e.
- ***Back-scattering geometry, semi-infinite medium, $L \to \infty$***

$$\mathrm{DOP}_{L,C} \cong \frac{3}{2}\exp\left[-\gamma\sqrt{\frac{3l^*}{\xi_{L,C}}}\right], \tag{7.83}$$

  where $l^*(= l_s/(1-g))$ is the transport mean free path of Eq. (7.81) and γ is the correlation decay parameter with value ranging between 1.5 and 3 [1].

We emphasize that the expressions for residual DOP in Eqs. (7.82) and (7.83) are valid in the *photon diffusion limit*, that is, after many scattering events. Moreover, these expressions typically neglect absorption, which can also be incorporated. In backscattering geometry, Eq. (7.83) is then modified to [1]:

$$\mathrm{DOP}_{L,C} \cong \frac{3}{2}\exp\left[-\gamma\left\{\sqrt{\frac{3l^*(1+\mu_a\xi_{L,C})}{\xi_{L,C}}} - \sqrt{3l^*\mu_a}\right\}\right] \tag{7.84}$$

Equations (7.82) to (7.84) essentially capture all the qualitative features of depolarization of light by multiple scattering (implicit is the assumption that the other polarimetry effects such as birefringence and diattenuation are absent). This is illustrated in Figure 7.13, where the computed variations of characteristic length scales of depolarization (normalized by the scattering mean free path l_s) ξ_L/l_s and ξ_C/l_s are shown as a function of the anisotropy parameter g of the medium. The inset shows the variations of ξ_L/l_s and ξ_C/l_s as a function of the size parameter of the scatterers

$$X = \frac{2\pi a\, n_m}{\lambda}, \tag{7.85}$$

where a is the scatterer radius, n_m the surrounding medium refractive index, and λ the wavelength. The observed qualitative trends can be summarized as follows:

(a) For isotropic scattering media composed of *Rayleigh scatterers* ($g \sim 0$, $a \ll \lambda$), depolarization of circularly polarized light is stronger than linearly polarized light ($\xi_L > \xi c$).
(b) The reverse is true if ($\xi_L < \xi c$), for anisotropic scattering media consisting of larger scatterers ($g \geq 0.7$, $a \geq \lambda$, the so-called *Mie regime*).
(c) The values of ξ_L/l_s and ξ_C/l_s increase monotonously (depolarization decreases) with increasing anisotropy g. When the same quantities are plotted as functions of the size parameter X, their variation is no longer monotonous, as they decrease for $X \geq 10$ (inset of Figure 7.15). This behavior is actually due to a decrease in g with increasing X in this range, an effect attributed to Mie resonances.

The underlying mechanism for depolarization dependence of linearly and circularly polarized light on the size of scatterers is worth a brief mention here. The decrease of depolarization with increasing g is easily understood as a decrease of the polarization randomization when scattering becomes more and more peaked in the forward direction.

The difference in relative rates of depolarization of linearly and circularly polarized light can be attributed to the different mechanisms of depolarization of the two. The depolarization of incident linearly polarized light occurs primarily due to the randomization of the direction of the incident field vector as a result of multiple scattering [65, 66]. On the other hand, depolarization of circularly polarized light occurs both due to the randomization of the field vector's direction and randomization of helicity [66]. Note that scattering at large angles flips the helicity of the circular polarization state resulting in its larger depolarization. In a turbid medium, light travels along many possible zig-zag paths, having contributions from scattering at various angles. For Rayleigh scatterers (where forward and backward scattering are approximately equally likely), the contribution of the large angle scattered photons is greater as compared to the larger sized Mie scatterers (where forward scattering predominates), ensuing stronger randomization of helicity and thus resulting in

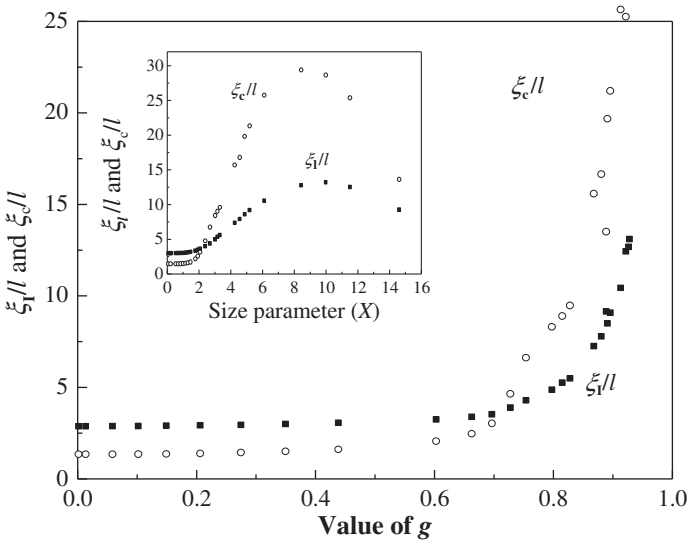

FIGURE 7.15 The theoretically computed variations of characteristic length scales of depolarization (normalized by scattering mean free path l_s) of incident linearly (ξ_L/l_s) and circularly (ξ_C/l_s) polarized light as a function of anisotropy parameter g. The inset shows the corresponding variation as a function of size parameter of scatterer X. The calculations were made for surrounding medium and scatterer refractive indices, respectively, equal to 1.33 and 1.59; and $\lambda = 0.6328$ μm). Adapted from Reference 65.

stronger depolarization of circularly polarized light in Rayleigh media. As the scatterer size increases, the additional cause of depolarization of circularly polarized light, that is, the flipping of helicity due to back scattering also gets reduced, resulting in weaker depolarization of circularly polarized light for anisotropic scattering samples [66, 67].

Note that the depolarization of light in a turbid medium is additionally influenced by the refractive index of the scatterers present in the medium. In fact, it has been shown that despite having large value of anisotropy parameter g, the depolarization characteristics of weakly fluctuating random medium (low value of the relative refractive index contrast $m = n_s / n_m \sim \leq 1.05$) can be similar to that of media composed of Rayleigh scatterers [61, 66]. This intriguing behavior originates from the fact that the anisotropic scatterers ($g \geq 0.7$, $X \gg 2$) having a lower value of relative refractive index m ($m \leq 1.05$) seem to belong in the weak scattering or Rayleigh-Gans regime, where each volume element within the scatterer gives electrical dipole scattering in an independent manner [72], yielding Rayleigh-like scattering matrix elements. The retention of this dipolar nature of scattering thus leads to depolarization characteristics of such low refractive index, anisotropic scattering medium (such as majority of biological tissues) much similar to that of Rayleigh scatterers.

These depolarization trends have been verified experimentally in turbid media composed of spherical scatterers having varying sizes [72–75]. One should,

however, exercise caution in generalizing these depolarization trends to arbitrary detection geometries, as depolarization metrics may exhibit more complex behaviors. Moreover, these analytical approaches, while useful, are approximate by their very nature and are accordingly restricted to the "tissue imaging" applications (employing polarization gating methods and various other co/cross polarization detection schemes). In contrast, for applications involving extraction/quantification of the intrinsic tissue polarimetry characteristics for tissue characterization, more encompassing approach such as the polarization-sensitive Monte-Carlo modeling are required.

7.4.1.3 Robust Polarization-Sensitive Monte-Carlo (PSMC) Approach for Modeling Complex Tissue Polarimetry Characteristics In this statistical approach to radiative transfer, the multiple scattering trajectories of individual photons are determined using a random number generator to predict the probability of each scattering event. It is also assumed that scattering events occur independently and exhibit no coherence effects. The position and propagation direction of each photon are initialized and modified as the photon propagates through the scattering medium. The photon propagates in the sample between scattering events a distance ℓ sampled from the probability distribution [70, 71]:

$$P(\ell)\,\mathrm{d}\ell = \frac{1}{\mu_\mathrm{t}} \exp[-\mu_\mathrm{t}\,\ell]\,\mathrm{d}\ell, \tag{7.86}$$

where the extinction coefficient μ_t describes the cumulative effect of scattering and absorption in the decay of the propagating light beam:

$$\mu_\mathrm{t} = \mu_\mathrm{s} + \mu_\mathrm{a}. \tag{7.87}$$

In conventional intensity-based MC models, when the photon encounters a scattering event, a scattering plane and angle are statistically sampled based on the so-called *scattering phase function*. Various types of scattering phase function has been used in MC tissue models, namely, the Mie theory-computed phase function or analytical approximations like the Henyey–Greenstein function [1].

In the polarization-sensitive Monte Carlo (PSMC) model, the photon's polarization, with respect to a set of arbitrary orthonormal axes defining its reference frame, is represented as a Stokes vector **S** and polarization effects are applied using medium Mueller matrices **M**, as illustrated in Figure 7.16. Upon encountering a scattering event, a scattering plane and angle are statistically sampled based on the polarization state of the photon (Stokes vector) and the full scattering Mueller matrix **M** (note that the angular variation of the m_{11} element of the scattering Mueller matrix is actually the scattering phase function for unpolarized light). The photon's reference frame is first expressed in the scattering plane and then transformed to the laboratory (experimentally observable) frame through multiplication of appropriate rotation matrices (reference frame manipulation) and by the Mueller matrix corresponding to

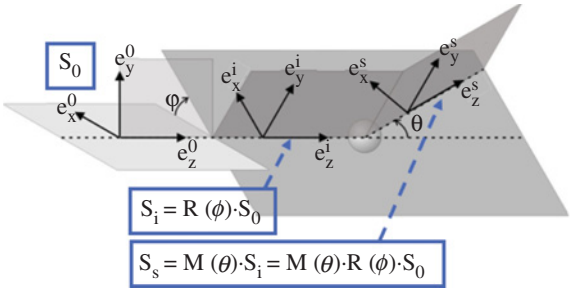

FIGURE 7.16 Transformation of the polarization state by an individual scattering event. The Stokes vector $\mathbf{S}_0$ describing the incident polarization is expressed in the reference frame $(\mathbf{e}_x^0, \mathbf{e}_y^0, \mathbf{e}_z^0)$defined from the previous scattering event. Then the azimuth ϕ and the polar angle θ of the scattered photon are sampled statistically from the phase function. The Stokes vector i describing the incident polarization is expressed as $\mathbf{S}_i$ in the $(\mathbf{e}_x^i, \mathbf{e}_y^i, \mathbf{e}_z^i)$frame obtained by rotating the initial frame by an angle ϕ in the (x,y) plane. Then the output Stokes vector $\mathbf{S}_e$ obtained from the previous one by applying the scattering Mueller matrix $\mathbf{M}(\theta)$, on $\mathbf{S}_i$ is expressed in the $(\mathbf{e}_x^s, \mathbf{e}_y^s, \mathbf{e}_z^s)$frame obtained by rotating the intermediate frame in the scattering plane by an angle θ around $\mathbf{e}_y^i = \mathbf{e}_y^s$.

the scattering event. Usually, the scattering Mueller matrix $\mathbf{M}$ is computed using Mie theory, which assumes the scattering medium to be composed of discrete spherical scatterers [76,77]. In principle, incorporation of scattering Mueller matrices for other non-spherical scatterers or the scattering matrices for other continuously fluctuating medium (such as tissue) is also possible [78].

The evolution of polarization state of each photon packet is tracked (via the Stokes vectors) following successive scattering events. The absorption effects are incorporated after successive scattering events by multiplying the photon by a factor that decreases its weight

$$\Omega = \frac{\mu_s}{\mu_a + \mu_s} \tag{7.88}$$

also called *albedo*, as conventionally done in intensity-based MC models [70].

Upon encountering an interface (either an internal one, representing tissue layers of different optical properties, or an external one, representing external boundary), the probability of either reflection or transmission is calculated using Fresnel coefficients. Assuming no interference effects, the final Stokes vectors for light exiting the sample in a particular direction (at any user selected detection point) are computed as the sum of all the appropriate sub-populations of photons. The sample Mueller matrix (for a given detection geometry) can then be calculated by sequentially changing the input polarization between four (or more) states, by recording the corresponding output Stokes vectors for each respective input states, and performing algebraic manipulations [76].

While the effects of scattering on the polarization evolution with successive scattering events can be modeled by the scattering Mueller matrix M, the effects of other medium polarimetry effects such as linear birefringence and optical activity can also be incorporated by including their corresponding Mueller matrices. However, difficulty arises in modeling many simultaneous polarization events in the presence of multiple scattering. Matrix multiplication is generally not commutative ($\mathbf{M}_A\mathbf{M}_B \neq \mathbf{M}_B\mathbf{M}_A$); thus, different orders in which these are applied will yield different effects (cf decomposition discussion of Section 7.2.3). Yet in actual tissues, these effects (such as optical activity due to chiral molecules and linear birefringence due to anisotropic tissue structures) are exhibited simultaneously and not one after the other as sequential multiplication implies. Thus, a realistic tissue model must include these simultaneous polarization effects in the presence of scattering.

This problem is tackled through the use of the so-called *N*-matrix formalism [7, 79], which combines several polarization effects into a single matrix describing them simultaneously. Briefly, in this formalism, the matrix of the sample is represented as exponential *sum* of differential matrices (*N*-matrices), wherein each matrix includes a single polarization effect [7, 79]. The issue of ordering of noncommutative matrices is overcome as matrix addition is always commutative. The differential matrices corresponding to each optical property exhibited by the sample are then summed to express the combined effect, and are subsequently applied to the photons as they propagate between scattering events. Note that an analogous differential matrix formalism for combining simultaneous polarimetry effects has been discussed in Section 7.2.3.3, in context to inverse polarimetry analysis. Finally, the scattering histories of a large number of photon packets (typically 10^7–10^9 photons are required to generate statistically acceptable results) are tracked as they propagate through the medium and are summed to yield the macroscopic parameters of practical interest (Stokes vectors, Mueller matrices, path length distributions, polarization statistics from different scattering histories, etc.).

In the simulation, circular and linear birefringence (these are the two relevant tissue polarimetry effects in addition to depolarization) are modeled through the optical activity χ in degrees per centimeter, and through the anisotropy in refractive indices (Δn), respectively [76]. Here, $\Delta n = (n_e - n_o)$ is the difference in refractive index along the extraordinary axis (n_e) and the ordinary axis (n_o). For simplicity, it is generally assumed that the direction of the extraordinary axis and the value for Δn is constant throughout the scattering medium (although recent research efforts are exploring the effects of multiple uniaxial domains of varying magnitude and orientation of birefringence [4; 80]. In each simulation, n_e and n_o are taken as input parameters and a specific direction of the extraordinary axis is chosen. As each photon propagates between scattering events, the difference in refractive indices seen by the photon depends on the propagation direction with respect to the extraordinary axis. The effect is usually modeled using standard formulae describing the angular variation of refractive index in uniaxial medium. Similar to conventional MC model, the scattering and absorption properties are modeled using the optical transport parameters (scattering coefficient μ_s and absorption coefficient μ_a and single scattering anisotropy g).

7.4.2 Experimental Testing and Validation in Tissue Phantoms

7.4.2.1 Forward Model The polarization sensitive Monte Carlo forward model, described above and the Mueller matrix inverse analysis methods, described in Section 7.2.4, requires comprehensive validation prior to their implementation for polarized light assessment of complex systems like tissues. The validity of these approaches has thus been tested on various tissue simulating phantoms exhibiting scattering and polarization properties, which are known and user-controlled *a priori* [61, 62, 81]. The validation studies have been performed on optical phantoms exhibiting either *sequential* or *simultaneous* polarization effects in presence of multiple scattering [45]. Note that in complex systems like tissues, no unique order (or sequence) can be assigned to the polarimetry effects; rather, these are exhibited *simultaneously* (except a few specific type of layered tissues, wherein sequential occurrence of some polarimetric effects may indeed happen). We shall thus present selected validation results on tissue phantoms exhibiting *simultaneous* scattering and polarization effects [3, 61, 62].

These solid phantoms were developed using polyacrylamide as a base medium, with sucrose-induced optical activity, polystyrene microspheres-induced scattering, and mechanical stretching to cause linear birefringence (or linear retardance). To apply controllable strain to produce linear birefringence, one end of the polyacrylamide phantoms was clamped to a mount and the other end to a linear translational stage, inducing varying linear birefringence with its axis along the direction of strain. These phantom systems mimic the complexity of biological tissues, exhibiting simultaneous effects of linear birefringence, optical activity, and depolarization due to multiple scattering. The experimentally recorded Mueller matrix from a birefringent, chiral, turbid phantom measured in the transmission geometry is shown in Figure 7.17a. The corresponding matrix generated through the PSMC model, using the same input optical parameters is shown in Figure 7.17b.

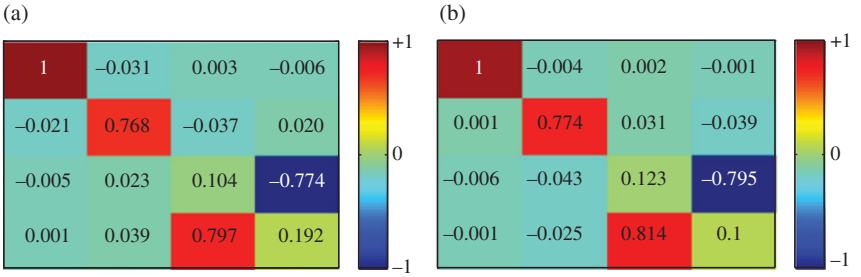

FIGURE 7.17 (a) The *experimentally* recorded Mueller matrix in the forward (transmission) detection geometry from a birefringent (extension = 4 mm, corresponding to a value of linear retardance $\delta = 1.345$ rad for 1 cm path length), chiral (concentration of sucrose = 1 M, $\chi = 1.96°$ cm^{-1}) turbid ($\mu_s = 30$ cm^{-1}, $g = 0.95$) phantom of thickness of 1 cm. (b) The corresponding Mueller matrix generated through the *PSMC model* with input parameters: linear birefringence $\Delta n = 1.36 \times 10^{-5}$ (corresponding to $\delta = 1.345$ rad), $\chi = 1.96°$ cm^{-1}, $\mu_s = 30$ cm^{-1}, $g = 0.95$. Adapted from Reference 3. (*For a color version of this figure, see the color plate section.*)

The simultaneous occurrence of the constituent medium polarization properties (depolarization, linear birefringence, and optical activity) are observed to contribute in a complex interrelated way to the Mueller matrix elements (both the experimental and the MC-simulated one), resulting in essentially all sixteen nonzero elements. Even though a direct quantification of the individual polarimetric contributions from such "lumped" system Mueller matrix is not possible, some qualitative features of the constituent polarimetry effects may readily be identified from the Mueller matrix elements:

1. In both the experimental and the MC-generated Mueller matrices, the signature of *linear birefringence* is reflected as considerable magnitudes of the m_{34} and m_{43} elements (representing horizontal/vertical linear birefringence), as one would expect for a linear retarder with orientation angle $\theta = 90°$. This is however, accompanied with nonzero magnitudes of m_{24} and m_{42} elements, which is a manifestation of the random orientation effects of linear birefringence (as experienced by different subpopulation of multiply scattered photons undergoing zig-zag paths in the medium).
2. *Chirality* (optical rotation) is manifested as a difference of m_{23} and m_{32} elements, even though the effect is considerably weaker. The inequality of the magnitudes of m_{23} and m_{32} elements is a manifestation of interrelated "cross-talk" contributions from other simultaneous effects.
3. The effect of *depolarization* is prominently reflected in the diagonal elements of the Mueller matrix. While the m_{22} element closely resembles polarization loss (horizontal/vertical linear depolarization) due to multiple scattering alone (additionally weakly influenced by optical rotation effects), the m_{33} ($\pm 45°$ linear depolarization) and m_{44} (circular depolarization) elements are strongly influenced by simultaneous linear birefringence effects and are accordingly considerably lower in magnitude.
4. In absence of any intrinsic diattenuation effects (either in the experimental phantom or in the simulation), the characteristic elements m_{12}, m_{13}, and m_{14} do not exhibit appreciable magnitudes.

The excellent agreement between the experimental and the simulated Mueller matrices emphasizes the capability of the PSMC model in simulating complex tissue polarimetry effects (simultaneous optical activity and birefringence in the presence of multiple scattering). Yet the complicated nature of the resultant Mueller matrix underscores the problems associated with polarimetric data interpretation in such complex systems. But as illustrated below, despite these complexities, the constituent polarimetry characteristics can be successfully isolated and quantified using the Mueller matrix inverse analysis (various decomposition) methods. The theory behind these was described in Section 7.2.3; we now turn to experimental validation studies of these approaches.

7.4.2.2 Inverse Polarimetric Analysis Figure 7.18 displays the results of inverse polarimetry analysis (Mueller matrix decomposition) on the experimental Mueller

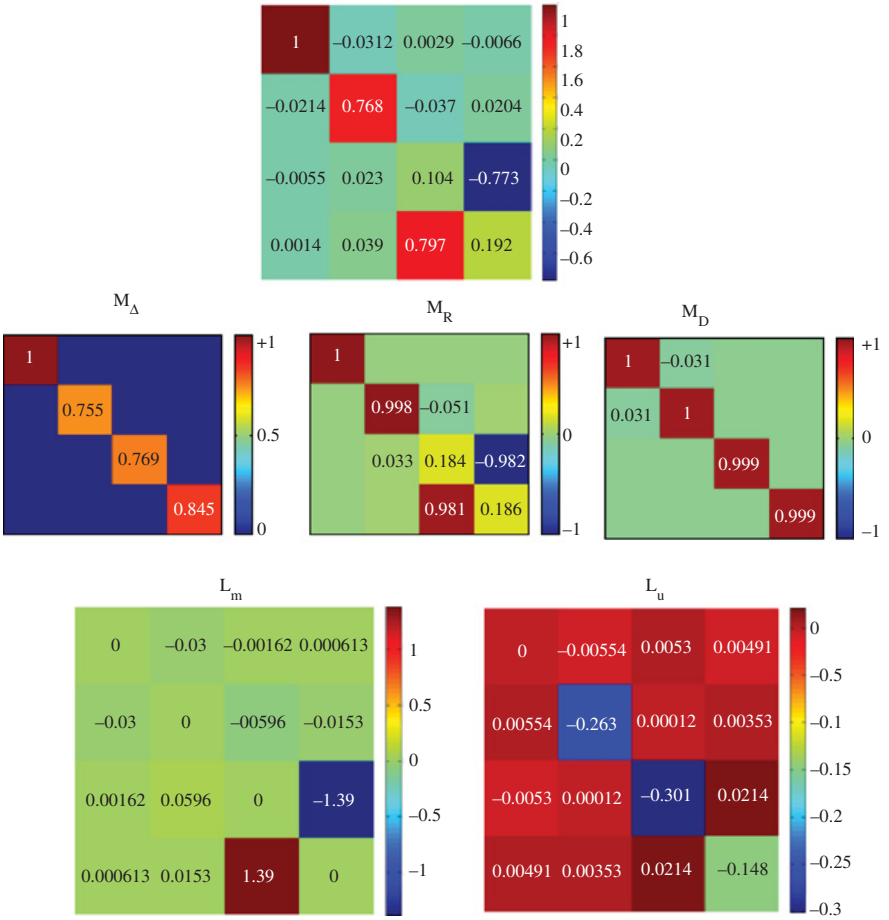

FIGURE 7.18 The *experimentally* recorded Mueller matrix in the forward detection geometry (top panel, reproduced from Fig. 7.17a). The basis matrices (M_Δ, M_R, M_D) obtained following the *forward polar decomposition* process (middle panel). The matrix logarithms L_m and L_u, derived using the *logarithmic decomposition* (bottom panel). The estimated polarization parameters using both the polar decomposition and the differential matrix approaches are listed in Table 7.3. Adapted from Reference 44. (*For a color version of this figure, see the color plate section.*)

matrix shown in Figure 7.17a [44]. Since these tissue phantoms exhibit *simultaneous* (rather than sequential) polarization effects, use of the *forward*, *reverse*, or *symmetric* product decomposition within the polar decomposition family (which employs *sequential* factorization of the elementary polarization effects) is expected to be somewhat inaccurate. For these three sequential product approaches, representative results are shown for the forward decomposition only (Figure 7.18, middle); these are compared with the logarithmic (differential matrix) decomposition which assumes *simultaneous* occurrence of the constituent polarimetry effects) (Fig. 7.18, bottom)

TABLE 7.3 The values for the polarization parameters, Δ, δ, ψ, and D, extracted using the *logarithmic decomposition* from the L_m matrix.

Parameters	Control input	Logarithmic decomposition	Forward polar decomposition
Δ	~0.188	0.211	0.210
δ (radian)	~1.574	1.386 ± 0.022	1.386
Ψ (radian)	~0.030	0.030 ± 0.001	0.030
D	~0	0.030 ± 0.009	0.032

The uncertainties in the δ, ψ, and D parameters are derived from the $\boldsymbol{L}_{\mathbf{u}}$ matrix. The values for the parameters extracted via *forward polar decomposition* (fourth column). The second column shows the control inputs. The control input for the net depolarization coefficient Δ was determined from the experimental Mueller matrix of the pure depolarizing phantom having no birefringence and optical activity. The expected value for linear retardance (δ) and optical rotation (ψ) are estimated by using the corresponding values from the nonscattering phantom ($\delta_0 = 1.345$ rad and $\psi_0 = 0.026$ rad) and accounting for increased path length $\langle Z \rangle$($\delta = \delta_0 \cdot \langle Z \rangle$, $\psi = \psi_0 \cdot \langle Z \rangle$, $\langle Z \rangle = 1.17$ cm is the MC-derived average photon path length).
Source: Adapted from Reference 44.

Evidently, the forward polar decomposition-derived basis matrices exhibit simpler characteristic features of standard sequential and homogeneous depolarization, retardance, and diattenuation matrices with many of the off-diagonal null elements (see Section 7.2.2), as expected. Similarly, the Lorentz antisymmetric $\mathbf{L}_m$ and symmetric $\mathbf{L}_u$ components of the matrix logarithm derived via the differential matrix formalism exhibit characteristic features of simultaneous depolarization, linear birefringence, and optical activity effects (their mean values and uncertainties discussed in Section 7.2.3.3).

The estimated polarization parameters using both the polar decomposition and the differential matrix formalisms are listed in the accompanying Table 7.3. In the absence of any intrinsic diattenuation property, the values for D estimated from both the decomposition formalisms are quite low and comparable (as expected). The estimated values for the depolarization coefficient Δ from the two formalisms are self-consistent and are also in excellent agreement with the controlled input.

Turning to the other two biologically important polarization parameters (linear retardance δ and optical rotation ψ), several interesting trends are seen. The derived optical rotation ψ in the presence of turbidity shows small increase as compared to that from analogous nonscattering phantom ($\psi_0 \sim 0.026$ rad, not shown here), which arises from the increase in optical path length due to multiple scattering (resulting in accumulations of ψ values). In fact, the accumulated value of ψ matches well the expected one$\psi = \psi_0 \cdot \langle Z \rangle$, where $\langle Z \rangle$ is the Monte Carlo-derived average photon path length for this specific geometry.

In contrast, although the composition-derived value for linear retardance δ of the turbid phantom is larger ($\delta \sim 1.386$ rad) than that for the clear phantom ($\delta_0 \sim 1.345$ rad), it is significantly *lower* than that expected for accumulated photon path length (1.574). This has been shown to arise due the curved zig-zag propagation paths for a group of multiply scattered photon population. Since components of such

curved photon paths are directed along the linear birefringence axis, this leads to a reduction in the apparent δ [44, 81].

The uncertainties (standard deviations) in the differential matrix-derived polarization parameters, $\Delta\delta^{\log\text{-}M}$, $\Delta\psi^{\log\text{-}M}$ (derived from the elements of the $\boldsymbol{L}_{\mathbf{u}}$ matrix), also warrant a brief comment. The uncertainty in linear retardance ($\Delta\delta^{\log\text{-}M}$) arises both due to strong depolarization present in this turbid phantom and due to the random orientation effects of linear birefringence (as observed by different sub-population of photons undergoing zig-zag paths in the medium). Since the latter effect does not influence the value for optical rotation, the resulting uncertainty $\Delta\psi^{\log\text{-}M}$ is also considerably lower as compared to $\Delta\delta^{\log\text{-}M}$. In general, the standard deviations in the polarization parameters contain useful information on the randomness of the medium and are also additionally influenced by the choice of the detection geometry, as described below.

The representative experimental results from complex tissue-like turbid media presented above (and continuing validation studies on several other phantoms exhibiting varying birefringence, optical activity, and depolarization effects) demonstrate that the intrinsic polarization parameters of such medium can be *self-consistently* extracted using either the logarithmic decomposition or the polar decomposition approach. One should note, however, that the illustrative results discussed above are based on Mueller matrices recorded in the forward detection geometry but the extension of this approach to backward detection geometry (which is well-suited for *in-situ* measurements) is warranted and has also been validated [82].

While the latter geometry is important for conceptual and practical reasons, it offers additional technical hurdles; notably, the polarization parameters associated with the intrinsic polarimetric properties of the sample in question can be difficult to infer since they are more strongly coupled with the scattering-induced artifacts. In fact, it has been shown that the scattering-induced artifacts gets considerably reduced for detection positions located at distances larger than a transport length away from the point of illumination ($r > l^*$). Thus, one possible method to measure polarization parameters from a turbid medium using backward detection geometry is to perform measurements at a distance larger than a transport length l^* away from the point of illumination [82].

It must, however, be noted that in the backscattering geometry, the reduction in apparent linear retardance δ due to the effect of the curved-propagation path is more prominent as compared to forward scattering geometry [44, 82]. Moreover, the apparent optical rotation Ψ in this geometry also gets considerably reduced due to the contribution of optical rotation of different handedness from two distinct subgroups of photons; while photons undergoing a series of forward scattering events to eventually emerge in the backward direction result in accumulated Ψ value, subgroups of photons that suffer scattering in the backward hemisphere only (backscattered photons) changes the handedness of rotation, leading to cancellation of net optical rotation [82]. For analogous reasons, the uncertainties in the differential matrix-derived linear retardance and optical rotation parameters ($\Delta\delta^{\log\text{-}M}$, $\Delta\psi^{\log\text{-}M}$) are also considerably larger in the backward detection geometry as compared to forward detection geometry [44].

Note that the phantoms described above do not exhibit any intrinsic diattenuation effect. Even though the magnitude of intrinsic diattenuation (dichroism) is typically very weak in most tissues, the effect of nonzero diattenuation effect is also worth a mention. As discussed in Section 7.2.3, in context to the forward and reverse polar decompositions, presence of layered tissue structures (interfaces) may yield significant diattenuation value, due to the different polarization response of the Fresnel reflection/transmission coefficients. For such tissues (e.g., skin), the diattenuation effect may not exhibit in a distributed manner (unlike depolarization or birefringence, which are typically exhibited from the bulk of tissue), rather may be exhibited in a sequential fashion. Since in the framework of the logarithmic decomposition (or in the differential matrix formalism), all the elementary polarization and depolarization properties of the medium are represented simultaneously, use of the logarithmic decomposition in such situation may lead to deviations in the extracted polarization parameters from those using polar decomposition. Moreover, in such case, either of the forward or the reverse decomposition may turn out to be advantageous depending upon the actual sequence of occurrence of the constituent polarization properties (as demonstrated with illustrative example in Fig. 7.6).

For most of the tissues exhibiting volumetrically distributed scattering and polarization effects, on the other hand, the logarithmic decomposition is expected to be more suitable. Thus, one must exercise caution in applying the different decomposition processes for tissue polarimetry characterization, a judicial choice of which (based on the experimental detection geometry and *a priori* estimate of the tissue morphology) may lead to realistic estimation of the intrinsic tissue polarization characteristics.

7.4.3 Summary

This part was devoted to the theoretical modeling of the propagation of polarized light in tissues. We first summarized the well-established methods for *forward modeling*, that is, the determination of the polarimetric response of well-known samples. Once adequate methods are available for forward modeling, the main issue to be addressed in practice is the inverse problem, that is, the interpretation of measured polarimetric responses of unknown samples.

As the main characteristic of biological tissues is predominantly their depolarizing power, which is related to multiple scattering, in first approximations most tissues can be modeled as suspensions of spherical scatterers in optically isotropic media. In such systems light propagation in multiple scattering regime may be conveniently described by the photon diffusion formalism, which provides simple analytical approximations for the DOP of the emerging light as function of the absorption and scattering coefficients μ_s and μ_a and the scattering anisotropy g, which, in turn, depend on the size and the index of the scatterers. Virtually all tissues exhibit larger depolarization for circular than linear incident polarization, as expected for scatterers much smaller than the light wavelength (Rayleigh regime) or with low index contrast (Rayleigh Gans regime). Beyond simple analytical approximations, the polarimetric response of suspensions of scatterers can be evaluated by Monte Carlo (MC)

simulations, provided the scatterers are not too closely packed, so that the light propagation in such suspensions can be considered as a sequence of "isolated" scattering events. MC method requires extensive computations, but it can fully take into account the actual geometry of the experiment, overall yielding accurate results. This accuracy has been experimentally tested on tissue phantoms exhibiting very complex polarimetric responses, including linear and circular birefringences as well as depolarization due to scattering.

These phantoms were also used to tackle the problem of inverse polarimetric analysis, by using the decomposition procedures outlined in Section 7.2.3. The logarithmic decomposition is expected to be the most accurate, as in the studied phantoms all polarimetric effects occur simultaneously and not sequentially, as assumed in the "three factor" forward and reverse polar decompositions. However, polar (forward) decomposition provides surprisingly good results, a finding which is yet to be fully understood. The logarithmic decomposition also allows to quantify the effect of increased photon path length in the evaluation of the phantom birefringence. Moreover, these phantom studies provide a good grasp of the dependence of the sample polarimetric response on the measurement geometry, which can act as a potentially misleading "artifact" if not properly taken into account.

In summary, the theoretical "toolbox" for the interpretation of polarimetric measurements, while not absolutely complete, seems sufficient for most practical investigations as those illustrated in the next part.

7.5 APPLICATIONS

In this section, we present some illustrative examples of selected polarimetry applications in biomedicine, both for optical imaging and tissue characterization applications.

7.5.1 Polarization-Gated Surface and Subsurface Imaging

Light polarization can be used as a *gating mechanism* able to separate the photons which have been deeply scattered in the bulk of the sample from those which remained close to the surface: the former are generally depolarized while the latter typically retain a significant part of their initial polarization. As a result, if an image (or a spectrum) $I_{\perp}$ is taken on with polarization orthogonal to that of the incident photons, the contribution of the deeply scattered photons is largely dominant. The contribution of the depolarized photons is also present in the image I_{II} taken with the same polarization as the incident light. As a result, the images $I_{\perp}$ and $I_{\mathrm{pol}} = I_{\mathrm{II}} - I_{\perp}$ are dominated by the "deep" or "superficial" contributions, respectively [83]. The penetration depth corresponding to the "superficial" contribution may be as small as a few mean free paths [84]. Spectral filtering may be added to polarization to further enhance the discrimination between "surface" and "bulk" contributions [85]. It is thus possible to get valuable information about the surface and bulk properties the tissue under study by taking only two orthogonally polarized image (or spectra). The use of linear polarizations discussed above can of course be generalized to

orthogonal circular polarizations as well. Moreover, in order to enhance the polarimetric response, the polarized image I_{pol} can be normalized by the total intensity, to provide the OSC

$$I_{\text{OSC}} = \frac{I_{\text{II}} - I_{\perp}}{I_{\text{II}} + I_{\perp}}. \tag{7.89}$$

Polarized imaging has been used, among other applications, in dermatology, to enhance the typically subtle visual contrasts differentiating various types of tissues. Early skin fibrosis of a thymic nude mice induced by X-ray irradiation was revealed by polarized imaging and suitable image analysis, while remaining undetectable by ordinary intensity imaging [85]. A variety of pigmented and nonpigmented skin abnormalities were studied by means of this technique by Jacques and coworkers [87], as illustrated in Figure 7.19. Polarized imaging revealed the disruption of the normal skin structure (collagen organization) due to cancerous lesions such as malignant basal cell carcinomas, suggesting a promising route to improve the definition of the excision margins in surgery [88].

The polarization gating schemes described above have also been exploited for depth selective spectroscopic measurements in tissue, which can improve the diagnostic efficacy of the spectroscopic approaches (elastic scattering [89, 90], fluorescence [91], and Raman spectroscopy [92]). As noted above, the underlying principle is similar: the photons which are scattered (or re-emitted) from deeper tissue layers undergo multiple scattering events and are depolarized to a larger extent. Polarization gating thus effectively selects photons which have not traveled beyond a few scattering mean free paths (mpf $= l^{-1} \sim 100$ μm in typical tissues).

Polarization-resolved spectroscopic approaches are thus expected to be particularly suitable for early detection of epithelial cancers (where the majority of human malignancies originate). Several illustrative examples demonstrate this approach. For instance, the polarization preserving component (from superficial tissue layers) extracted using polarization gating exhibited a fine structure component that was periodic in wavelength [89]. This was identified as being due to light that is Mie scattered by surface epithelial cell nuclei. By analyzing the amplitude and frequency of this signal using Mie theory, the size distribution and the refractive index of the nuclei was calculated. Since the size (and distribution) and refractive index of epithelial cell nuclei are valuable parameters for detecting precancerous changes, this technique holds promise for *in situ* and early diagnosis of epithelial cancer [93]. In addition to the fine structure component, the polarization-gated elastic scattering signal also showed inverse power law spectral dependence [90]. This was related to the self-similar (fractal) nature of microscale fluctuations of local refractive index in tissue. This was modeled using Fractal-Born approximation of light scattering to yield the fractal micro-optical parameters, namely, the fractal dimension and the fractal upper scale, which were also related to the pathological status of the examined tissue [90].

Polarization-gated fluorescence spectroscopic measurements have also been explored for improving diagnostic efficacy of fluorescence-based methods [91, 94]. Specifically, polarization-gated fluorescence measurements have been successfully

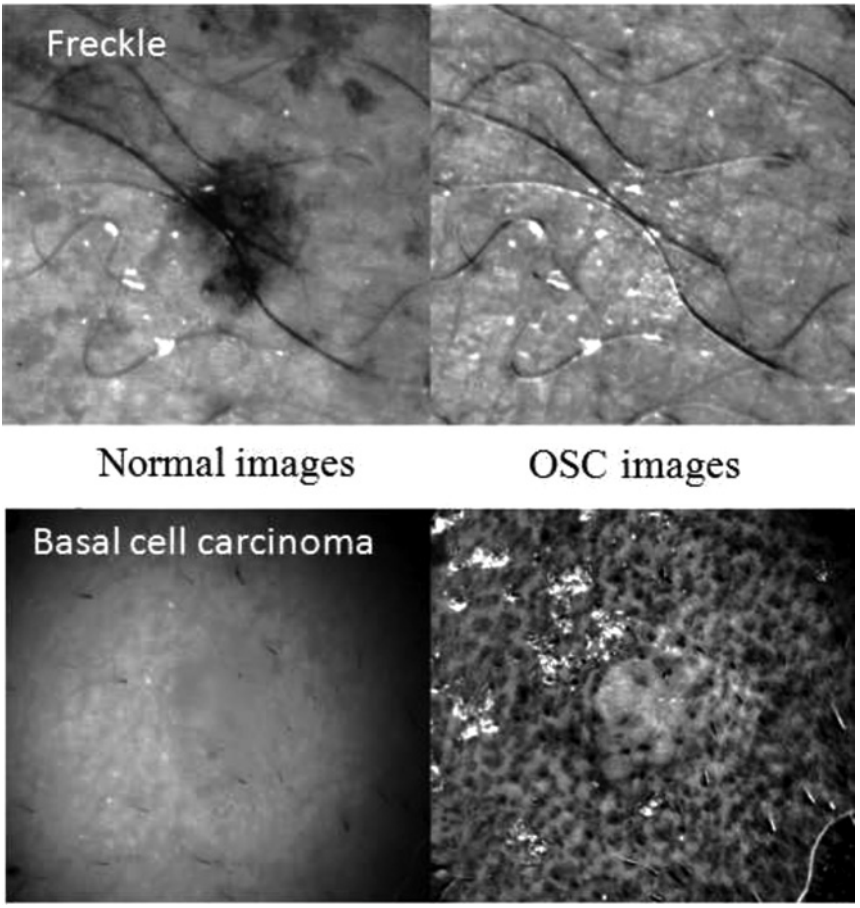

FIGURE 7.19 Normal intensity images and OSC images of a pigmented skin lesion (a freckle, top) and nonpigmented one (malignant basal cell carcinoma, bottom). The normalization by the total intensity in the OSC procedure is clearly very efficient in removing the effects of pigmentation in the polarimetric contrast. Adapted from Reference 87.

exploited to decouple, isolate, and quantify fluorescence contributions from tissue layers. Note that fluorescence signal from layered epithelial tissues, detected with conventional measurement technique (and similar to diffuse reflectance studies), is due to contributions from different endogenous fluorophores (having different quantum yields, lifetimes, and overlapping spectral line shapes) present in the superficial epithelial layer and the underlying connective tissue (stroma). Depth-resolved fluorescence measurement facilitated by the polarization gating should thus help improve contrast in the autofluorescence from malignant and normal sites. Similar strategy on polarization-resolved measurements has also been exploited for depth-resolved Raman spectroscopic measurements in layered epithelial tissues [92].

7.5.2 Tissue Assessment with Mueller Polarimetry

The OSC technique outlined above can provide quantitative and useful information primarily if the sample is a pure (linear and/or circular) depolarizer. In more complex cases of practical interest, the tissue may exhibit, in addition to depolarization, linear and possibly circular birefringence. If so, complete polarimetric characterization likely requires full Mueller matrix polarimetry, typically followed by an analysis based on the decompositions outlined in Section 7.2.3 and an interpretation of the polarimetric properties obtained by this procedure.

7.5.2.1 Noninvasive Glucometry Glucose is an optically active (chiral) molecule, and its structural asymmetry imposes a unique "fingerprint" on polarized light that interacts with it. For example, the plane of polarization of linearly polarized light is rotated upon passage through a glucose solution, by an amount proportional to the light interaction length, its concentration, and its wavelength-dependent rotatory power (a known quantity). As such, the glucose concentration in *clear* media can be easily determined by polarimetric measurements of optical rotation (this is routinely done, for example in biochemical laboratories and in the food industry). Can a similar polarized light approach be used in biomedicine, for example to noninvasively determine blood glucose levels in diabetic patients? If yes, this would represent a tremendous advance, as noninvasive glucose sensing remains arguably one of the most pressing unsolved problems in clinical medicine. Numerous approaches have been and are being actively explored to address this difficult challenge [61, 95].

Unfortunately, the polarimetric approach for biomedical glucometry is also fraught with difficulties. Unlike its "easy" transparent media counterpart, light propagating in tissue does not have a unique interaction length which is needed to convert measured optical rotation to glucose concentration; other dominant and complex tissue effects such as multiple scattering and inhomogeneous birefringence depolarize the light and alter its polarization properties (including causing chirality-unrelated apparent rotation of its linear polarized fraction); the glucose chirality effects are rather weak (owing to the low physiologic levels of blood glucose, in the range of 3–30 mM, or ~0.5–5 g L^{-1} of blood, yielding optical rotations in the millidegree range); other chiral molecules present in tissue mask the already-weak glucose signal, and so on. Nevertheless, we and others have performed careful fundamental feasibility studies toward polarimetric tissue glucometry, as briefly summarized below.

Figure 7.20 shows millidegree-level optical rotations ψ induced by physiological (millimolar) glucose concentrations in a 1-cm-thick polystyrene microsphere scattering phantom ($\mu_s \sim 30$ cm^{-1}) [61]. This study was performed with a sensitive polarimetric system that utilized polarization modulation and synchronous detection similar to Figure 7.12 but with a dual balanced photodetector approach, optimized to measure weak polarization signals in largely depolarized background. The results shown are for the forward-direction transmission geometry, with the rotations calculated from the determined Stokes vectors via $\psi = 0.5\tan^{-1}(u/q)$. The forward transmission direction was selected to enable direct results interpretation (path length $\geq$ cuvette thickness, rotation directly proportional to glucose concentration) and to

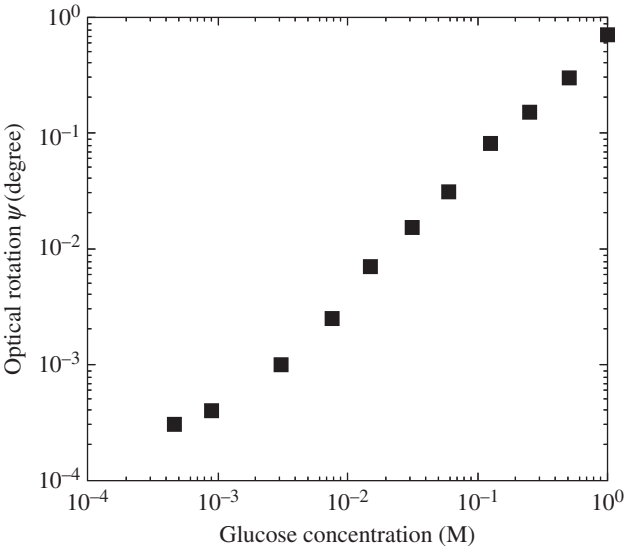

FIGURE 7.20 Logarithmic plot of experimentally determined optical rotation as a function of glucose concentration in scattering media (1.4 μm diameter polystyrene microspheres in water, $\mu_s \sim 28$ cm^{-1}) down to physiological glucose levels. Measurements were performed using forward detection geometry ($\gamma = 0°$ in Fig. 7.12) through 1 cm of turbid media in a quartz cuvette. Adapted from Reference 61.

minimize rotation artifacts unrelated to chirality (e.g., scattering-induced apparent rotation, see Figure 7.21). The drawback of the transmission geometry is severe depolarization, limiting polarimetric measurements to 2–3 mm thicknesses of tissue [61]; this is why the scattering coefficient for this study in 1-cm-thick cuvette was lowered to ~30% of typical tissue levels (~100 cm^{-1}). Nevertheless, this preliminary study shows the polarimetric potential for measuring physiological glucose levels in tissue-like scattering media.

Backward detection geometry in reflection mode is more convenient for practical tissue applications, yet the chirality-unrelated optical rotation artifacts can be severe [82]. A method to suppress these artifacts is thus essential, and the Mueller matrix polar decomposition methodology can be used to advantage here. Figure 7.21 shows the variations in the scattering-induced apparent rotation and in the chirality-induced true optical rotation as a function of offset distance from the point of illumination, in the backscattering direction [3, 82]. As seen, the scattering rotation artifact can be nearly an order of magnitude larger than the small chirality effect, completely dominating and masking the presence of glucose. The polar decomposition reveals that the scattering rotation does not arise due to intrinsic chirality of the medium, rather is due to the scattering-induced linear diattenuation effect (also shown in the figure). Importantly, polar decomposition can effectively separate out these two differently sized contributions, revealing the glucose signal in this important yet artifact-prone

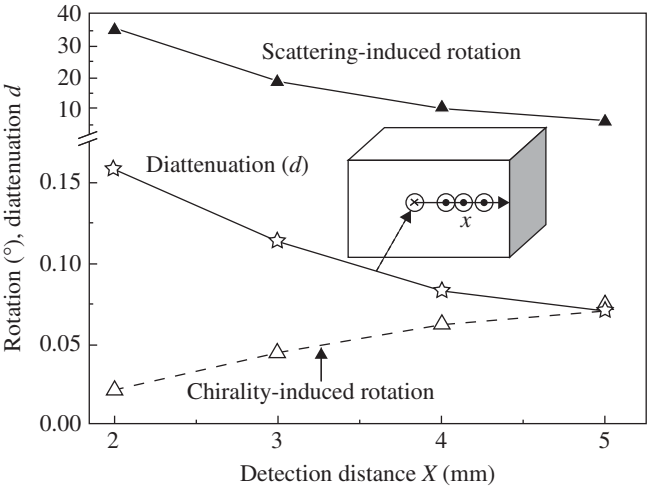

FIGURE 7.21 Optical rotation (ψ), derived from the decomposition of Monte Carlo-generated Mueller matrices (open triangles), of backscattered light as a function of distance from the center of the incident beam impinging on a chiral ($\chi = 0.082°$ cm^{-1}, corresponding to 100 mM concentration of glucose) isotropic turbid medium ($\mu_s = 30$ cm^{-1}, $g = 0.95$, thickness = 1 cm). The solid triangles represent the corresponding scattering-induced rotation of the polarization vector, derived from the Stokes parameters of the scattered light (for incident polarization state $S = (1,0,1,0)^T$). Also shown (open stars) is the apparent diattenuation which seems to be responsible for the scattering-induced rotation artifact. The inset shows the backward detection geometry. The chirality-induced rotation approaches zero as the detection angle approaches the exact backscattering detection ($\chi = 0^\circ$ cm^{-1}, data not shown). The symbols represent Monte Carlo and decomposition-derived data points and the lines serve to guide the eye. Adapted from References 3 and 82.

detection geometry. Despite the highly preliminary nature of this study—the complicating effects of other chiral confounders, experimental validation of these Monte Carlo simulations results, signal changes due to varying optical absorption, and other complexities yet to be evaluated—this does suggest a method to tease out small glucose specific signals in highly scattering tissues. In combination with Monte Carlo-determined path length distributions, we are currently investigating spectroscopic polarimetry coupled with chemometric regression analysis to isolate glucose rotations from contributions of other chiral confounders [96]. Further, given the extremely challenging nature of the noninvasive glucometry problem, it is worthwhile to consider hybrid approaches; that is, combining spectral turbid polarimetry with another diagnostic modality (e.g., spectral diffuse reflectance, Raman, photoacoustics) by carefully drawing on each technique's complementary strengths in isolating small tissue glucose signals.

7.5.2.2 Cancer Diagnosis Smith et al. [63] demonstrated the potential of full Mueller polarimetric imaging in dermatology by studying various tissue

abnormalities. Melanomas exhibited *reduced depolarization power* with respect to surrounding healthy tissue; as shown in several other studies, this trend seems to be quite general when comparing healthy and (pre)cancerous tissues. No such effect was observed on benign lesions, or in lupus lesions, which, however, exhibited slightly reduced retardance, whose slow and fast axes showed rapid spatial variation across the lesions.

Polar decomposition of Mueller matrices has also been evaluated for the diagnosis of oral precancer [97]. Precancers induced in cheek pouches of hamsters were imaged *in vivo* and then analyzed histologically. Again, the precancerous tissues were characterized by reduced depolarization and retardance with respect to surrounding healthy tissue.

Ex vivo colon samples have been studied by Pierangelo et al. [98, 99] with multispectral Mueller polarimetry. In contrast with the previous examples, these samples did not exhibit any significant retardance nor diattenuation. The polarimetric information was thus provided mostly by the depolarization power throughout the visible spectrum (from 500 to 700 nm). Depolarization was found to increase with increasing wavelength from the green to the red part of the spectrum. This general trend is due to decreasing absorption, which thus increases the average number of scattering events photons suffer before being detected and results in higher polarization scrambling/loss. Moreover, depolarization varied significantly with the degree of tumor penetration within the colon structure. At the beginning (stage T1), the tumor is confined to the most internal superficial layers (the mucosa and submucosa). Then at stage T2, it gets *ulcerated* (its thickness decreases by eliminating the "top" layers of cancerous tissue while the tumor attacks the underlying layer (the muscularis)). At stage T3, the tumor reaches the outermost layer (the serosa or pericolic tissue) and eventually perforates it (stage T4).

Figure 7.22 shows an example of depolarization images of a colon with a cancerous lesion, together with the corresponding histologic pathology analysis. Using the healthy region (H) at the left of the figure as a reference, the burgeoning part B (graded histologically as T1) is less depolarizing, in agreement with the previous examples. However, at inner regions of the lesion (point 2, stage T2), depolarization increases again, and even more so in the innermost region (stage T3). In the lowest part of the figure, the sample is "folded," showing directly pericolic tissue, which appears to be extremely depolarizing (probably due to its very weak absorption, as this tissue is essentially fat, with very low hemoglobin concentration). Thus the non-monotonic behavior of depolarization with the disease progression may be attributed to the influence of the pericolic tissue, which increases when ulceration progresses, making the tissue more and more depolarizing after the initial depolarization decrease observed at the initial burgeoning stage.

In spite of its complicated non-monotonic behavior, the depolarization contrast might be used as a diagnostic tool to provide a quick tumor staging, a possibility which would be particularly useful if polarimetric imaging could be implemented endoscopically.

In addition to tumor detection and staging, polarimetric imaging might also be useful for the follow-up of radiochemotherapy (RC) of locally advanced cancers [99].

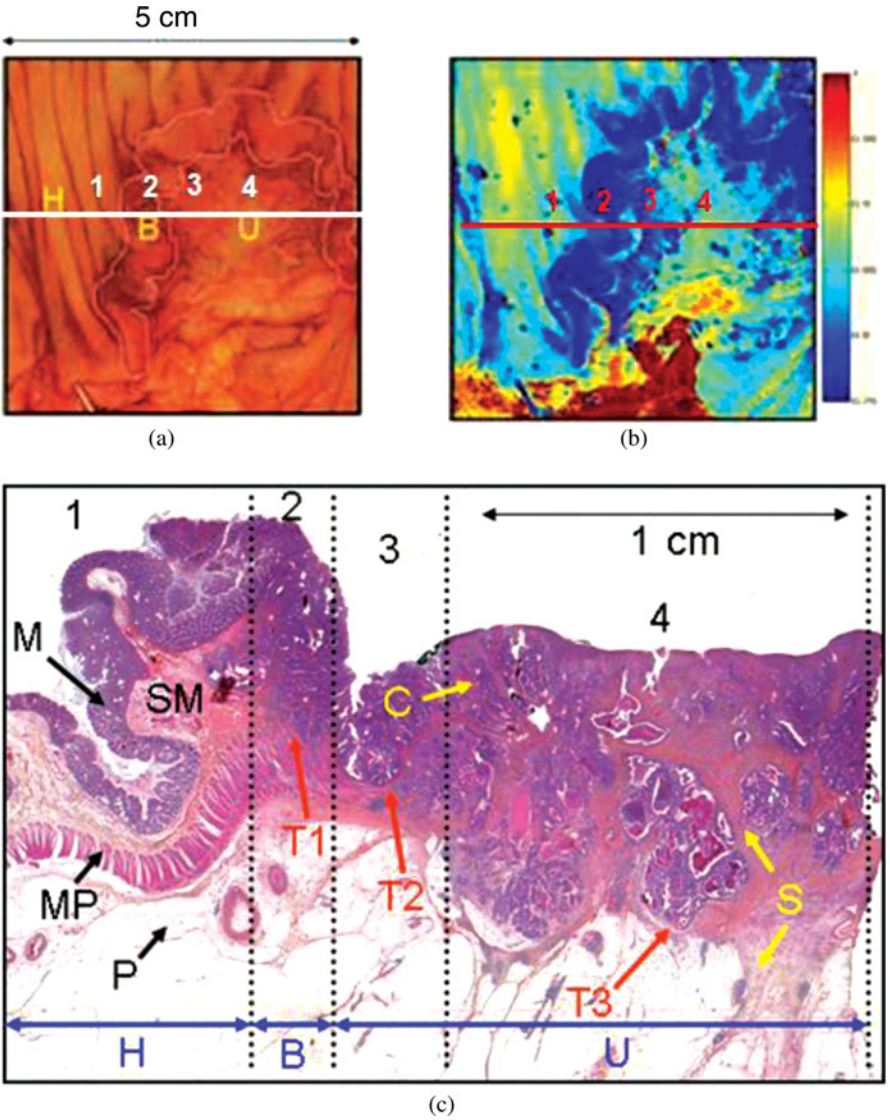

FIGURE 7.22 (a) Photo of the colon sample, with healthy (H) tissue, burgeoning (B) and ulcerated (U) cancerous regions. (b) Depolarization image (values given by the color bar from 0 (blue) to 1 (red)) of the same sample. The solid line indicates the depth cut which has been studied histologically. In this cut, shown in panel, (c), the regions marked 1 (healthy), 2 (burgeoning), 3 and 4 (ulcerated) are seen, together with the staging of the lesions, from T1 to T3. The different layers are identified by M (mucosa), SM (submucosa), MP (muscularis), and P (pericolic tissue, or serosa). (S) and (C) designate stromal and cancerous tissues, characterized by low and high cell densities, respectively. Adapted from Reference 99. (*For a color version of this figure, see the color plate section.*)

We studied three mesorectum samples excised after neoadjuvant radiochemotherapy. For T3 to T4 lesions, with or without regional metastatic lymph nodes, such neoadjuvant procedures are known to make surgery easier and to reduce the probability of relapse [100]. The patients were irradiated with standard doses (∼50 Gy) and operated 6 weeks later. For the three samples, the "footprints" of the initial tumors exhibited polarimetric contrasts (compared to healthy regions) which could be correlated with the degree of cancer regression after RC. Further, tumor depolarization appeared lower than that of surrounding healthy tissue, even though the residual tumor volume fraction/cellular tumor compartment was estimated from pathology to be only a few percent. Such high polarimetric sensitivity suggests that it is not the tumoral (cellular) tissue itself which is detected, but more probably the difference in the fibrous collagen structure induced by the presence of cancer cells (as further discussed below).

Another topic of potentially addressable by tissue polarimetry is the diagnosis of uterine cervical cancer. This disease, due to infection by Human Papilloma Virus (HPV), begins with precancerous lesions confined within the epithelium and classified as CIN1, CIN2 or CIN3 (acronym for Cervical Intraepithelial Neoplasia) when anomalous cells invade the lowest third, two-thirds, or the entire epithelium thickness. If not treated, CIN3 lesions eventually disrupt the epithelium basal membrane and evolve into potentially lethal invasive cancer. This evolution is very slow, with 5–10 years typically elapsing from the initial infection to the onset of invasive cancer. As with many cancers, the disease can be cured very effectively by surgically removing the anomalous regions on the cervix. Thus it is of paramount importance to screen female populations to enable early disease detection, and to localize the pathological regions as accurately as possible.

In developed countries, the first screening step is the Pap smear, which consists of a cytologic examination of the cells collected from the cervix. If these cells seem anomalous (typically exhibit large nuclei), the patient then undergoes a detailed examination of the cervix by means of a colposope (long working distance microscope) to localize the CIN lesions, take biopsies and eventually decide a treatment course. However, colposcopy is a notoriously difficult and operator-dependent examination, with relatively poor performance [101]. There are thus many surgeries performed without real necessity, or with incorrect surgical margins relative to the true extend on the tumor. Conversely, essentially no screening is proposed in developing countries (systematic Pap smears would require too many pathologists to examine the samples). Thus this disease kills ∼275,000 women worldwide every year, the vast majority of which could have been saved by a simple and accurate surgery. Clearly then, useful alternatives to the Pap smear, possibly by simple optical means, are very much needed to solve this outstanding public health problem [102]. In this respect, a large amount of work has been performed on fluorescence / reflectance cervical imaging by several groups, including those led by Richards Kortum, Follen, and MacAuley [102, 103]. A meta-study, carried out by these researcher and others and based on 26 clinical studies [103], concluded that these methods offered similar performance as colposcopy, and may thus be used as adjuncts. For resource limited countries, particularly simple and low-cost techniques, such as VIA (Visual Inspection with Acetic acid, which is

basically a colposcopic examination with the naked eye or a standard color camera) have also been evaluated and showed good potential, in spite of rather low sensitivity, of the order of 30% [104]. To summarize, significant progress is still needed in the management of cervical cancer, especially in low resource countries.

Polarimetric imaging is also a promising approach in addressing this topic [64]. Several samples have been imaged *ex vivo* by using the polarimeter shown in Figure 7.13 of Section 7.3.3.3. Typical results, obtained from two samples, are shown in Figure 7.23. The first sample was healthy, while the second one contained a CIN3 zone and a benign lesion (an ectropion), where a layer of glandular tissue was seen (this tissue is normally present only in the endocervix). The pathology diagnosis was established according to the standard procedure: fixing the sample in formalin, cutting it into 4 mm thick blocks, embedding it in paraffin, shaving from the

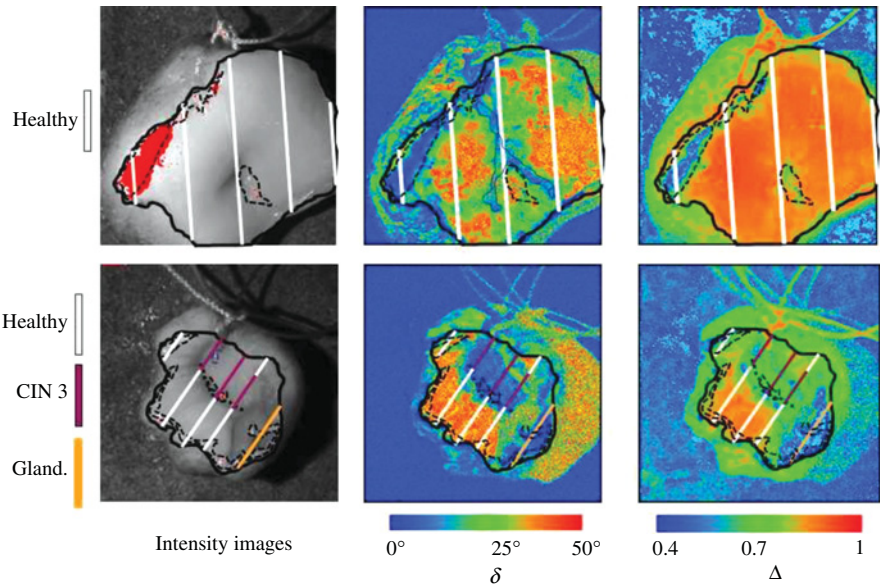

FIGURE 7.23 Images of two *ex vivo* cervix samples, one healthy (top) and the other one with a CIN3 zone and a benign lesion (visible glandular tissue) (bottom). Left column: raw intensity images. Middle column: images of scalar retardance δ, in color scale from 0° to 50°. Right column: images of depolarization Δ, from 0.4 to 1. Retardance and depolarization were obtained from raw Mueller images by standard Lu-Chipman decomposition procedure of the experimentally determined Mueller matrix images. On each sample, the solid black line shows the limit of the intact epithelium. The straight lines indicate the locations of the histological cuts where the pathology diagnostic was made (white for healthy, purple for CIN3, and orange for glandular tissue). The dashed black lines designate regions where at least one among the 16 raw intensity images was saturated due to tissue "glare." The top left image shows an example of such saturated region, shown in red. Obviously, polarimetric data in these regions are suspect. Adapted from Reference 64. (*For a color version of this figure, see the color plate section.*)

resulting "wax blocks" 5-μm-thick slices, deparaffinizing and staining them for microscopic examination. As a result, pathology diagnosis was established only along the "lines" shown in the intensity images (left column) of Figure 7.23; they are repeated in the corresponding polarimetrc images for landmarking and for correlation with microscopy-derived pathology grades. Viewing the ordinary intensity images in the left column, basically no difference was observable between the healthy and CIN3 tissues, while the glandular tissue was more reddish (and thus more absorbing at the operating wavelength, 550 nm).

The Mueller images were decomposed by the standard Lu-Chipman procedure, and the resulting scalar retardance and depolarization images are shown. The healthy sample is characterized by strong retardance almost everywhere, with predominantly tangential slow axis orientation (not shown). On the pathologic sample, there is a healthy region in the lower left part of the image, again characterized by a strong retardance, while both the CIN3 and the ectropion show essentially ∼zero retardance. The depolarization is again very strong everywhere on the healthy sample, while on the other one it decreases from healthy to CIN3 to glandular regions.

Although these results (described more fully in [64]) must be substantiated with much more extensive studies, preliminary trends strongly suggest that uterine cervix tissue exhibits strong birefringence in its healthy regions, with birefringence disappearing at the very earliest stages of the precancerous evolution.

These observations are very promising in the context of an "automated" optical diagnosis of uterine cervical precancer (thus not requiring the often unavailable expertise of a medical specialist) and are substantiated by the results of other groups. For example, Shukla and Pradhan [105] have also studied histology of cervical samples and showed that the connective tissue beneath healthy epithelium exhibits significantly larger retardance values than that beneath precancerous epithelium. It is well known that precancerous evolution of epithelia modifies the structure of neighboring connective tissues via a decrease in size and concentration of collagen fibers [106]. Such modifications are probably the main reason of the observed disappearance of the tissue birefringence in abnormal regions of cervical tissues, and might in fact occur in other sites/clinical scenarios of interest for medical diagnostics.

7.5.2.3 Characterization of Structural Tissue Anisotropy and Applications Several studies have addressed tissue structural anisotropy monitoring using polarimetric techniques [3, 62, 107, 108]; the above discussions of colonic and cervical pathologies are particular examples of this approach in oncology. As mentioned, tissue structural anisotropy can stem from aligned orientations of tissue fibrillar components, such as collagen and elastin, actin-myosin fibers, and mineralized hydroxyapatite crystals [1]. Since such structural alignments often manifest as linear birefringence effects, quantification of linear birefringence may represent a sensitive metric for changes in tissue structure. A number of investigations have therefore addressed such polarization birefringence measurement for the detection of tissue abnormalities like osteoarthritis, thermal injury and cancer (e.g., basal and squamous cell carcinomas) [3, 62, 107, 108]. Measurement of complete Mueller matrix and its inverse analysis via the various decomposition approaches (outlined in Section 2.3) are clearly

advantageous for this purpose because (*i*) the small birefringence alterations can be efficiently decoupled and quantified in presence of the other tissue polarimetry effects; (*ii*) the decomposition process yields additional tissue polarimetry metrics (e.g., diattenuation, depolarization, and potentially others not discussed above, such as retardance ellipticity), which provide useful complementary information thus generating a more complete picture of the complex biophysical alterations taking place in tissue. In the following, we offer two other cancer-unrelated illustrative examples of tissue structural anisotropy characterization with polarized light: bladder wall abnormalities and regenerative heart treatments.

Bladder is an example of internal organ whose structure and function engenders anisotropic tissue structure. Its purpose is to store and then expel urine, and its wall layers extend and then contract to allow this to happen. Microstructural remodeling in its epithelial layers is known to occur under mechanical distension and during various disease processes (e.g., bladder outlet obstruction). As a step toward developing a turbid polarimetry platform for human bladder pathology studies, we have recently obtained birefringence maps in normal *ex-vivo* distended rat bladders that demonstrate the differential response of different bladder regions (dome, ventral, and dorsal sides) to changes in filling pressure [109]. The results of Figure 7.24 were obtained under pressures that represent typical physiological ranges in normal rodent (and human) bladders; as we progress to examine pathological cases, the upper end of the pressure range will likely have to increase. As seen, the dome region of the bladder shows maximum birefringence when the bladder is distended to high pressures, whereas the ventral tissues remains roughly isotropic during distension. In addition, the average anisotropy direction is longitudinal, along the urethra to dome. Using the analysis in Section 7.2.3.1, we converted the retardance values (derived from polar decomposition) to birefringence by measuring the bladder wall thickness with an optical coherence tomography (OCT) system, and by estimating the average photon path length in this reflection geometry via our polarization-sensitive Monte Carlo model (Section 7.4.1.3). The derived wall anisotropy trends thus represent an intrinsic tissue property of its anisotropy/organization independent of thickness, to better aid in understanding the structure-functions relation in healthy bladders. These new insights into the wall microstructure anisotropy of *ex vivo* distending bladders may also help improve the functionality of the artificially engineered bladder tissues [110].

Myocardial muscle tissues exhibit high level of linear birefringence in its healthy state due to the aligned arrangement of cardiomyocytes and collagen fibers [111]. Following a heart attack, the structural anisotropy is expected to reduce due to structural remodeling, with cardiomyocyte atrophy and an increase in fibrotic collagen content (scar tissue). Various postinfarct therapies (e.g., stem cell tissue regeneration) aim to restore heart muscle towards its normal structure (by further structural remodeling), and more importantly restore some of its functional status. Mueller matrix measurement and its inverse analysis may serve as a sensitive probe the state of the myocardium after infarction and report on the success of regenerative treatments [111, 112]. In order to explore this possibility, Mueller matrices were recorded in the transmission geometry, from 1-mm-thick *ex vivo* myocardial samples from

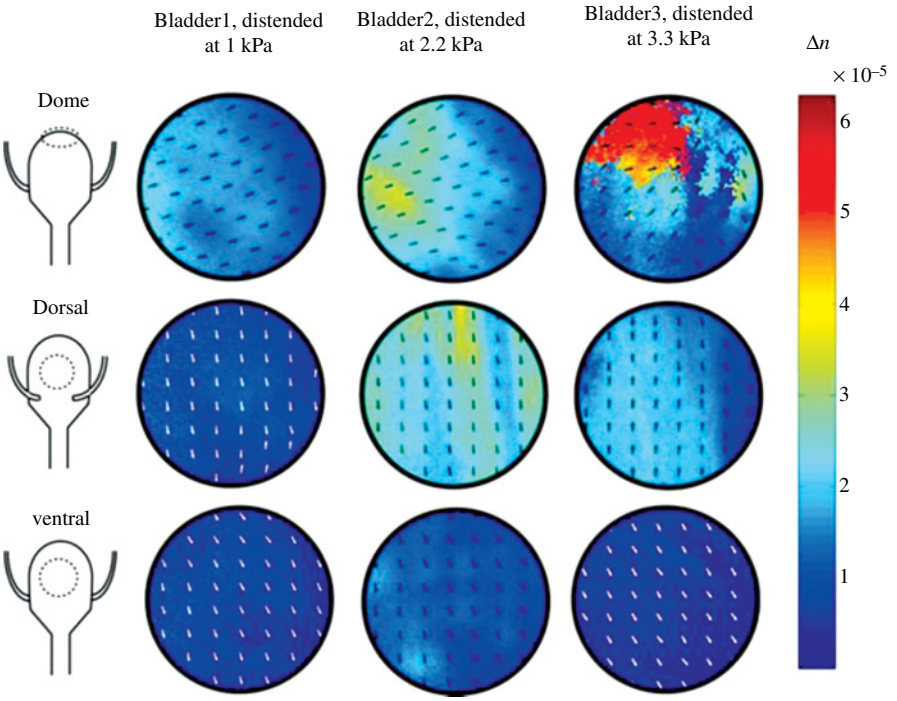

FIGURE 7.24 Variation of the local birefringence of *ex vivo* rat bladder tissue with pressure. The left, middle, and right columns show the retardance images of three different regions of the organ (dome, dorsal, and ventral surfaces, as shown at the extreme left of the figure) for distending pressures equal to 1.0, 2.2, and 3.3 kPa, respectively. The field of view is 2 mm in diameter. The images were taken in backscattering geometry, at 25° from the exact backscattering direction, and processed by the polar decomposition (see Section 7.2.3.1) to extract the retardance parameters, namely the scalar retardance and the anisotropy orientation, the latter being shown by arrows. The tissue birefringence, shown in the color bar scale of Δn at the extreme right, was calculated from the scalar retardance and the tissue effective thickness. This thickness was derived from OCT measurements and evaluation of the average path length of the photon trajectories due to the multiple scattering events by Monte Carlo simulations. Note the maximum birefringence in the dome region upon maximum distension, and the overall longitudinal anisotropy orientation (along the urethra-dome axis). Adapted from Reference 108. (*For a color version of this figure, see the color plate section.*)

Lewis rats after myocardial infarction, both with and without stem cell treatments. Measurements were made using both the point measurement and imaging polarimetry systems. The point measurement system employed polarization modulation and synchronous lock-in detection (described in Section 7.3.3.2, Fig. 7.12). Imaging polarimetry employed dc measurements with the PSG-PSA–based approach (also discussed in Section 7.3) to construct the Mueller matrix. The Mueller matrices measured by either of these systems were analyzed via polar decomposition to obtain linear retardance (δ) values. The results are summarized in Figure 7.24.

The observed main features can be summarized as (i) the infarcted region of the untreated myocardium exhibits a large decrease in the magnitude of δ (Fig. 7.25b). In contrast, in the infarcted region after stem cell treatment an increase in δ toward the native levels is observed (Fig. 7.25b), indicating regrowth and reorganization/remodeling of the myocardium. (ii) The polarimetry images (Fig. 7.25c) from the same tissue also show similar retardance trends, although with some variations (due to difference in measurement geometry and spatial heterogeneity in tissue optics). The spatial variation of the retardance images (Fig. 7.25c) not only shows difference from infarct to normal, but within each region as well (the δ values are higher in the middle of the myocardial wall with gradual lower values toward the edges).

This variation through the myocardial wall is attributed to the change in orientation of the myocyte fibers through the wall [112]. Nevertheless, the increase in δ in the infarcted regions of the stem-cell treated hearts indicates reorganization and regrowth of the myocardium microstructure caused by therapeutic stem cell injection, as was subsequently confirmed by histology [112]. Note that other tissue polarimetry metrics that emerged from the Mueller matrix decomposition analysis, namely, diattenuation and depolarization, also yielded complementary and useful microstructural information (on the orientation/alignment of the myocyte fibers through the wall and their changes with infarction as well as with stem cell treatment) [44, 111, 112]. Moreover, a study with nonlinear microscopy (second harmonic generation, two-photon excited fluorescence) has also validated and complemented the polarimetry results, and yielded useful information on the underlying causes of the measured retardance signals, in the context of collagen versus cardiomyocytes components and their spatial organization. The details of these results have been published [44, 111, 112].

Although quantification of tissue structural anisotropy via polarimetry have shown considerable promise for a variety of applications involving tissue diagnosis and therapy monitoring, several technical and conceptual challenges in quantifying intrinsic tissue anisotropy still remain to be resolved [113, 114]. These include understanding the influence of complex three dimensionally oriented birefringent tissue structures, orientation-varying spatial domains or potentially non-uniaxial (biaxial) birefringent domains, on the measured Stokes vector or Mueller matrix elements; and development of methods to extract geometry-independent metrics of tissue anisotropy (intrinsic birefringence and its actual orientation). Recent studies have attempted to address these issues [109, 113–115]. For example, a sphere-cylinder scattering model has been adopted in polarization sensitive Monte Carlo simulations to forward model the effect of such complex microstructural architecture (skeletal muscle as representative birefringent tissue) on the Mueller matrix elemental images [114]. A dual projection polarimetry method (whereby the sample is imaged twice at different incident angles of the probing beam) in combination with Mueller matrix decomposition has also been developed to quantify true intrinsic magnitude and orientation angle of retardance from three dimensionally oriented birefringent structures [113]. After successful validation of this approach on birefringent spherical phantoms, the method has been explored for the measurement (imaging) of the anisotropy axis and its true magnitude in *ex-vivo* porcine myocardium tissue [113].

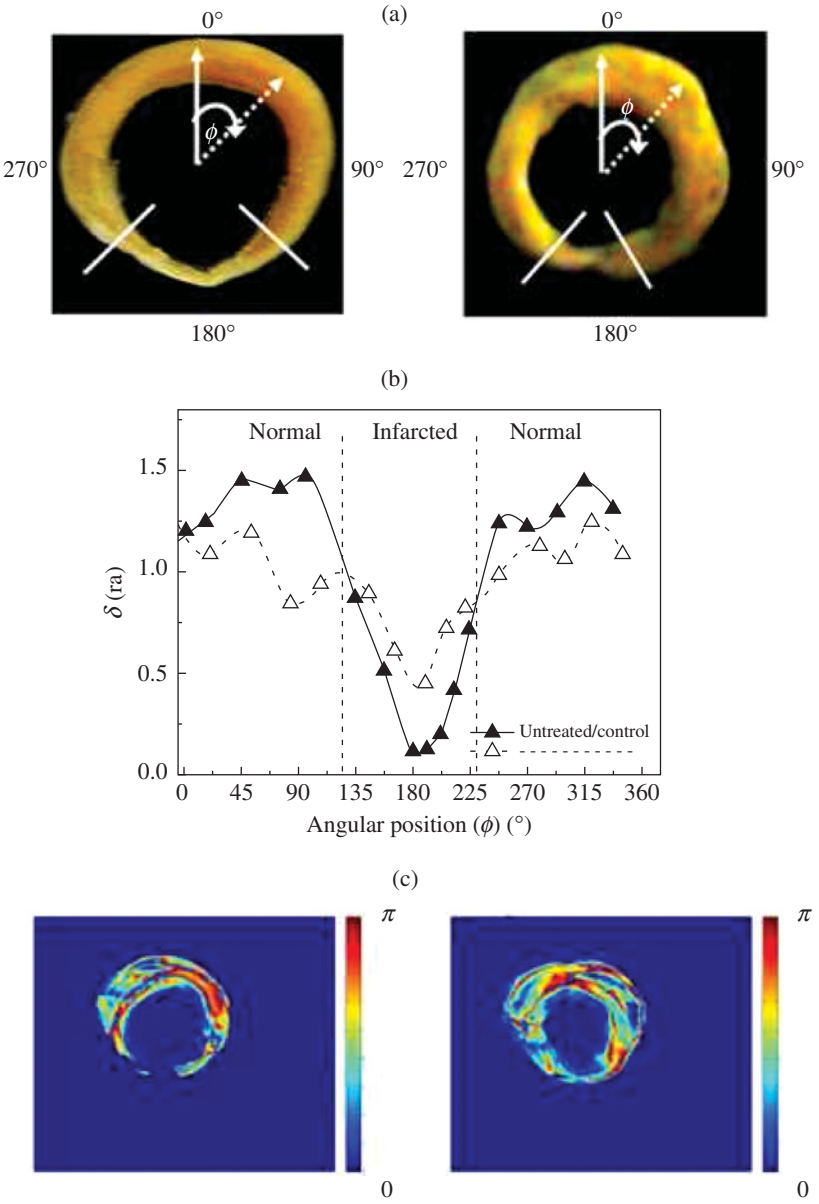

FIGURE 7.25 Linear retardance δ extracted from experimentally determined Mueller matrices (using the Mueller matrix polar decomposition analysis (Section 7.2.3) corresponding to 1-mm-thick tissue sections from Lewis rat hearts following myocardial infarction. (a) White-light photographs of untreated (left panel) and stem cell treated (right panel) tissue. (b) Mueller matrix-derived linear retardance (δ) values at different angular positions from the untreated (solid triangles) and treated (open triangles) samples. (c) The corresponding linear retardance (δ) images for the same tissue derived from imaging polarimetry measurements. Adapted from References 3 and 111.

7.5.3 Summary

In this section, we reviewed some examples of "real-world" applications of polarimetric imaging for biomedical purposes. In a first instance, polarization can be used as a gating mechanism, allowing to isolate nondepolarized contribution in scattered light to enhance single scattering signal coming from the most superficial tissue layers, which can be used for example to evaluate the size of the cell nuclei and differentiate healthy and cancerous tissues.

The multiply scattered contribution, which is usually dominant, typically exhibits strong depolarization. In the absence of other major polarimetric effects, this parameter can be easily evaluated by partial polarimetric techniques like OSC, which are relatively simple to implement in imaging systems and may prove very useful, for example in dermatology for assessment of the surgical margins for the removal of melanomas. Exploratory studies on colon samples suggest that simple OSC may also be sufficient for early detection and characterization cancerous polyps at various stages. At the earliest precancerous stages, depolarization decreases (this seems to be a quite general trend) while at more advanced stages, at least in colon, the depolarization variation is more complex due to increased contribution of the serosa, which is weakly absorbing and strongly depolarizing.

Conversely, many other samples of interest for medical applications, such as uterine cervix and oral cavity, may exhibit not only depolarization, but also linear and circular birefringence. If so, full Mueller polarimetry, with subsequent matrix decomposition, is needed to "disentangle" these effects to eventually provide relevant parameters for diagnostics. As a rule of thumb, precancerous evolution seems to be associated with a decrease of tissue birefringence and depolarizing power, but here too the detailed behavior may be more complex, at least for cervical tissue, due to the presence of two very different epithelia (malpighian and columnar). Further studies, involving tens or even hundreds of samples, are thus needed to fully assess the performance of polarimetric imaging for cancer detectionand staging.

Polarimetry is also promising in fields other than oncology. Noninvasive glucometry has been viewed as "holy grail" in diabetology for decades. The optical activity induced by glucose may prove relevant for this purpose, provided extremely weak rotations can be measured and isolated from artifacts. Highly sensitive Mueller polarimetry coupled with matrix decomposition has demonstrated the capability to extract optical rotations in the millidegree range induced by glucose at physiological levels in the presence of multiple scattering and strong geometry induced artifacts. However, the elimination of the contribution of optically active compounds other than glucose remains a formidable challenge.

Last but not least, polarimetry may also prove very useful for noninvasive characterization of many other anisotropic tissues, such as myocardial muscle, where birefringence seems to provide a very sensitive indicator of the tissue status (healthy or infarcted or regenerating) and for the follow-up of treatments like tissue reconstitution from stem cells. Preliminary studies on bladder wall tissue also show the relevance of polarimetric imaging for the study of biomechanical properties of tissues, in part aimed at improving tissue engineering for grafts.

All these examples clearly show the strong potential of polarimetry, both in imaging and nonimaging modes, for medical applications. However, large-scale studies are still needed for each application to fully assess the performance of the technique. Moreover, each application may require specialized developments, both in instrumentation and in data analysis.

7.6 CONCLUSIONS AND OUTLOOK

Biological tissues typically exhibit quite complex polarimetric responses, which may require sophisticated experimental and data treatment techniques to eventually provide relevant parameters for medical diagnostics and tissue assessment. This complexity is certainly the main reason why polarimetry has not yet been developed to its full potential. However, this field has been progressing very quickly in the past decade, holding the promise of great improvements in optical diagnostics for many diseases in various fields.

In almost all tissues, the incident beam is strongly scattered, with scattering path lengths on the order of $\sim$100 μm, leading to significant depolarization of the emerging light. The other polarimetric effects often present are linear retardation, due to possible tissue linear birefringence, and (generally weaker) optical activity (or circular retardation/birefringence). Adequate description of these effects requires the Stokes Mueller formalism, which is not so widely known in biophotonics. It is thus described in some detail in the first part of this chapter, including the currently available procedures of matrix decompositions, which are essential for polarimetric data analysis and constitute an active research field in themselves.

Polarimetric instrumentation is also rapidly evolving, based on the general principles and typical setups outlined in the second part. In this respect, it is worth emphasizing that polarimetry is intrinsically a low cost technique, which can be added to virtually any optical system, allowing operation at any chosen spatial scale, from microscopic to mesoscopic to macroscopic.

The interpretation of polarimetric data is also a challenging and active field. Forward modeling of the polarimetric responses of known systems can be realized by various approaches, from simple analytical models to numerically demanding Monte Carlo simulations. Forward modeling has provided considerable physical insight in the mechanisms of depolarization in suspensions of spherical scatterers in optically isotropic media. Other practically important properties, such as the effect of tissue linear and circular birefringence, are currently being actively explored.

While forward modeling is extremely useful to understand the basic mechanisms defining the polarimetric response of a given type of sample in a given measurement geometry, for optical diagnostics in principle one has to solve the *inverse problem*, that is to determine the tissue "nature" from the measured polarimetric data. Ideally, this should be achieved by fitting simulation based on a relevant multiparameter physical model of the tissue to the experimental data. The values of the physical parameters, such as scatterer densities, optical indexes, layer thicknesses, and the like, could then be "parametrically" mapped onto "conventional" (optical, histologic, etc.) images

whose meaning is clear. Unfortunately this is seldom feasible, due to the difficulty of realistic and accurate tissue models (without relying on too many loosely determined "parameters"), and to the computational burden related to such fitting procedure. As a result, polarimetric data are usually interpreted in terms of the elementary polarimetric properties provided by matrix decompositions. For a number of samples and various pathologies, these properties exhibit interesting trends which may eventually provide highly relevant tissue assessment metrics related to underlying tissue biophysical properties. To this end, the current developments in Mueller matrix decomposition theory and polarimetric instrumentation advances must be pursued in concert with extensive *ex vivo* and *in vivo* cross-checking and validation studies.

So far, polarimetry has been limited to tissues accessible to direct imaging, and many possibilities, such as polarimetry-guided surgery, have still to be explored within this parameter space. But of course the scope of the polarimetric methodologies would be significantly broadened if it could be extended to endoscopic systems. Several research groups are at the forefront of this exciting polarimetric development [116–118].

To conclude, given the expanding range of medical applications and the current improvements in both experimental setups and data analysis procedures, the medium-term and long-term future of tissue polarimetry appear very promising.

REFERENCES

[1] V. V. Tuchin, L. Wang, and D. À. Zimnyakov, *Optical Polarization in Biomedical Applications* (Springer, New York, 2006).

[2] L. V. Wang, G. L Coté, and S. L. Jacques, "Special section guest editorial: tissue polarimetry," *J. Biomed. Opt.* **7**, 278 (2002).

[3] N. Ghosh and I. A. Vitkin, "Tissue polarimetry: concepts, challenges, applications and outlook," *J. Biomed. Opt.* **16**, 110801 (2011).

[4] S. L. Jacques, "Polarized light imaging of biological tissues" in *Handbook of Biomedical Optics*, edited by D. Boas and N. Ramanujam (CRC Press, 2011).

[5] R. C. Jones, "A new calculus for the treatment of optical systems," *J. Opt. Soc. Am.* **31**, 488–493 (and following papers in the same issue) (1941).

[6] E. Collett, *Polarized Light: Fundamentals and Applications* (Marcel Dekker Inc., New York, 1990).

[7] D. S. Kliger, J. W. Lewis, and C. E. Randall, *Polarized Light in Optics and Spectroscopy* (Academic Press–Harcourt Brace Jovanovich, New York, 1990).

[8] J. W. Goodman, "Statistical Properties of Laser Speckle Patterns", in *Laser Speckle and Related Phenomena, Vol. 9, Topics in Applied Physics*, edited by J. C. Dainty (Springer, Berlin, Heidelberg, New York, Tokyo, 1984).

[9] G. G. Stokes, "On the composition and resolution of streams of polarized light from different sources," *Trans. Cambridge Phil. Soc.* **9**, 339–416 (1852).

[10] S. Huard, *The Polarization of Light* (John Wiley & Sons, New York, 1997).

[11] R. A. Chipman, "Polarimetry," in *Handbook of Optics*, 2nd ed., edited by M. Bass (McGraw-Hill, New York, 1994), Vol. 2, Chap. 22, pp. 22.1–22.37.

[12] D. Goldstein, *Polarized Light* (Marcel Dekker, New York, 2003).

[13] B. N. Simon, S. Simon, F. Gori, M. Santarsiero, R. Borghi, N. Mukunda, and R. Simon, "Nonquantum entanglement resolves a basic issue in polarization optics," *Phys. Rev. Lett.* **104**, 023901 (2010).

[14] E. Wolf, "Unified theory of coherence and polarization of random electromagnetic beams," *Phys. Lett. A* **312**, 263–267 (2003).

[15] G. Milione, H. I. Sztul, D. A. Nolan, and R. R. Alfano, "Higher-order Poincaré sphere, stokes parameters, and the angular momentum of light," *Phys. Rev. Lett.* **107**, 053601 (2011).

[16] G. Milione, S. Evans, D. A. Nolan, and R. R. Alfano, "Higher order Pancharatnam-Berry phase and the angular momentum of light," *Phys. Rev. Lett.* **108**, 190401 (2012).

[17] L. Marrucci, E. Karimi, S. Slussarenko, B. Piccirillo, E. Santamato, E. Nagali, and Fabio Sciarrino, "Spin-to-orbital conversion of the angular momentum of light and its classical and quantum applications," *J. Opt.* **13**, 064001 (2011).

[18] H. Mueller, "The foundation of optics," *J. Opt. Soc. Am.* **38**, 551 (1948)

[19] J. J. Gil, "Characteristic properties of Mueller matrices," *J. Opt. Soc. Am. A* **17**, 328–334 (2000).

[20] S. R. Cloude, "Group theory and polarisation algebra," *Optik* **75**, 26 (1986).

[21] D. G. M. Anderson and R. Barakat, "Necessary and sufficient conditions for a Mueller matrix to be derivable from a Jones matrix," *J. Opt. Soc. Am. A* **11**, 2305 (1994).

[22] J. J. Gil and E. Bernabeu, "A depolarization criterion in Mueller matrices," *Opt. Act.* **32**, 259–261 (1985).

[23] M. Born and E. Wolf, *Principles of Optics* (Cambridge University Press, New York, 2002).

[24] S. Lu and R. A. Chipman, "Interpretation of Mueller matrices based on polar decomposition," *J. Opt. Soc. Am. A* **13**, 1106–1113 (1996).

[25] M. Xu and R. R. Alfano, "Random walk of polarized light in turbid media," *Phys. Rev. Lett.* **95**, 213901 (2005).

[26] R. Ossikovski, M. Anastasiadou, and A. de Martino, "Product decompositions of depolarizing Mueller matrices with negative determinants," *Opt. Commun.* **281**, 2406 (2008).

[27] S. P. Morgan and M. E. Ridgway, "Polarization properties of light backscattered from a two layer scattering medium," *Opt. Express* **7**, 395–402 (2000).

[28] A. H. Hielscher, A. A. Eick, J. R. Mourant, D. Shen, J. P. Freyer, and I. J. Bigio, "Diffuse backscattering Mueller matrices of highly scattering media," *Opt. Express* **1**, 441–453 (1997).

[29] V. Sankaran, J. T. Walsh Jr., and D. J. Maitland, "Comparative study of polarized light propagation in biologic tissues," *J. Biomed. Opt.* **7**, 300–306 (2002).

[30] M.-R Antonelli, A. Pierangelo, T. Novikova, P. Validire, A. Benali, B. Gayet, and A. De Martino, "Mueller matrix imaging of human colon tissuefor cancer diagnostics: how Monte Carlo modeling can help in the interpretation of experimental data," *Opt. Express* **18**, 10200–10208 (2010).

[31] M. Ahmad, S. Alali, A. Kim, M. F. G. Wood, M. Ikram, and I.A. Vitkin, "Do different turbid media with matched bulk optical properties also exhibit similar polarization properties ?" *Biomed. Opt. Express* **2**, 3248–3258 (2011).

[32] N. Ghosh, M. F. G. Wood, and I. A. Vitkin, "Influence of the order of the constituent basis matrices on the Mueller matrix decomposition derived polarization parameters in complex turbid media such as biological tissues," *Opt. Commun.* **283**, 1200–1208 (2010).

[33] J. Morio and F. Goudail, "Influence of the order of diattenuator, retarder, and polarizer in polar decomposition of Mueller matrices," *Opt. Lett.* **29**, 2234–2236 (2004).

[34] R. Ossikovski, A. De Martino, and S. Guyot, "Forward and reverse product decompositions of depolarizing Mueller matrices," *Opt. Lett.* **32**, 689 (2007).

[35] M. Anastasiadou, S. Ben Hatit, R. Ossikovski, S. Guyot, and A. de Martino, "Experimental validation of the reverse polar decomposition of depolarizing Mueller matrices," *J. Eur. Opt. Soc (JEOS) – Rapid Publ.* **2**, 07018 (2007).

[36] R. Ossikovski, M. Anastasiadou, S. Ben Hatit, E. Garcia-Caurel, and A. de Martino, "Depolarizing Mueller matrices: how to decompose them?" *Phys. Stat. Sol* (a) **205**, 720–727 (2008).

[37] R. Ossikovski, "Analysis of depolarizing Mueller matrices through a symmetric decomposition," *J. Opt. Soc. Am. A* **26**, 1109–1118 (2009)

[38] C. Fallet, A. Pierangelo, R. Ossikovski, and A. de Martino, "Experimental validation of the symmetric decomposition of Mueller matrices," *Opt. Express* **18**, 831–842, (2009).

[39] R. Ossikovski, C. Fallet, A. Pierangelo, and A. de Martino, "Experimental implementation and properties of Stokes nondiagonalizable depolarizing Mueller matrices," *Opt. Lett.* **34**, 974 (2009).

[40] R. Ossikovski, M. Foldyna, C. Fallet, and A. de Martino, "Experimental evidence for naturally occurring nondiagonal depolarizers," *Opt. Lett.* **34**, 2426–2428 (2009).

[41] R. Ossikovski, "Differential matrix formalism for depolarizing anisotropic media," *Opt. Lett.* **36**, 2330–2332 (2011).

[42] N. Ortega-Quijano and J. L. Arce-Diego, "Depolarizing differential Mueller matrices," *Opt. Lett.* **36**, 2429–2431 (2011).

[43] R. M. A. Azzam, "Propagation of partially polarized light through anisotropic media with or without depolarization: a differential 4×4 matrix calculus," *J. Opt. Soc. Am.* **68**, 1756–1767 (1978).

[44] S. Kumar, H. Purwar, R. Ossikovski, I. Alex Vitkin, and N. Ghosh, "Comparative study of differential matrix and extended polar decomposition formalisms for polarimetric characterization of complex tissue-like turbid media," *J. Biomed. Opt.* **17**, 105006 (2012).

[45] N. Ortega-Quijano, B. Haj-Ibrahim, E. García-Caurel, J.-L. Arce-Diego, and R. Ossikovski, "Experimental validation of Mueller matrix differential decomposition," *Opt. Express* **20**, 1151–1163 (2012).

[46] D. H. Goldstein, "Mueller matrix dual-rotating retarder polarimeter," *Appl. Opt.* **31**, 6676–6683 (1990).

[47] D. S. Sabatke, M. R. Descour, E. L. Dereniak, W. C. Sweatt, S. A. Kemme, and G. S. Phipps, "Optimization of retardance for a complete Stokes polarimeter," *Opt. Lett.* **25**, 802–804 (2000).

[48] J. S. Tyo, "Noise equalization in Stokes parameter images obtained by use of variable-retardance polarimeters," *Opt. Lett.* **25**, 1198–1200 (2000).

[49] E. Compain and B. Drévillon, "High-frequency modulation of the four states of polarization of light with a single phase modulator," *Rev. Sci. Instrum.* **69**, 1574–1580 (1998).

[50] M. H. Smith, "Optimization of a dual-rotating-retarder Mueller matrix polarimeter," *Appl. Opt.* **41**, 2488–2493 (2002).

[51] J. Zallat, S. Aïnouz S, and M. Ph. Stoll, "Optimal configurations for imaging polarimeters: impact of image noise and systematic errors," *J. Opt. A. Pure Appl. Opt.* **8**, 807 (2006).

[52] D. Layden, M. F. G. Wood, and A. Vtikin, "Optimum selection of input polarization states in determining the sample Mueller matrix: a dual photoelastic polarimeter approach," *Opt. Express* **20**, 20466–20481 (2012).

[53] E. Collett, "Measurement of the four Stokes polarization parameters with a single circular polarizer," *Opt. Commun.* **52**, 77–80 (1984).

[54] R. W. Collins and J. Koh, "Dual rotating-compensator multi-channel ellipsometer: instrument design for real-time Mueller matrix spectroscopy of surfaces and films," *J. Opt. Soc. Am. A* **16**, 1997–2006 (1999).

[55] C.-Y. Han and Y.-F. Chao, "Photoelastic modulated imaging ellipsometry by stroboscopic illumination technique," *Rev. Sci. Instrum.* **77**, 023107–5 (2006).

[56] M. Richert, X. Orlik, and A. De Martino, "Adapted polarized state contrast image," *Opt. Express* **17**, 14199–14210 (2009).

[57] G. Anna, F. Goudail, and D. Dolfi "General state contrast imaging: an optimized polarimetric imaging modality insensitive to spatial intensity fluctuations," *J. Opt. Soc. Am. A* **29**, 892–900 (2012).

[58] M. Anastasiadou, A. de Martino, D. Clément, F. Liège, B. Laude-Boulesteix, N. Quang, J. Dreyfuss, B. Huynh, A. Nazac, L. Schwartz, et al. "Polarimetric imaging for the diagnosis of cervical cancer," *Phys. Stat. Sol. (c)* **5**, 1423 (2008).

[59] A, Bénière, M. Alouini, F. Goudail, and D. Dolfi, "Design and experimental validation of a snapshot polarization contrast imager," *Appl. Opt.* **48**, 5764–5773 (2009).

[60] J. C. Ramella-Roman, K. Lee, S. A. Prahl, and S. L. Jacques, "Designing, testing and clinical studies of a handheld polarized light camera," *J. Biomed. Opt.* **9**, 1305–1310 (2004).

[61] M. F. G. Wood, N. Ghosh, X. Guo, and I. A. Vitkin, "Towards noninvasive glucose sensing using polarization analysis of multiply scattered light," in *Handbook of Optical Sensing of Glucose in Biological Fluids and Tissues*, Series in Medical Physics and Biomedical Engineering, edited by V. V. Tuchin (Taylor and Francis Publishing, London, 2008), Vol. 12, Chap. 17.

[62] N. Ghosh, M. Wood, and A. Vitkin, "Polarized light assessment of complex turbid media such as biological tissues using Mueller matrix decomposition," in *Handbook of Photonics for Biomedical Science*, edited by V. V. Tuchin (Taylor and Francis Publishing, London, 2010), Chap. 9.

[63] M. H. Smith, P. Burke, A. Lompado, E. Tanner, and L. W. Hillman "Mueller matrix imaging polarimetry in dermatology," *Proc. SPIE* **3911**, 210–216 (2000)

[64] A. Pierangelo, A. Nazac, A. Benali, P. Validire, H. Cohen, T. Novikova, B. Haj Ibrahim, S. Manhas, C. Fallet, M.-R. Antonelli, et al. "Polarimetric imaging of uterine cervix: a case study," *Opt. Express* **21**, 14120–14130 (2013).

[65] D. Bicout, C. Brosseau, A. S. Martinez, and J. M. Schmitt, "Depolarization of multiply scattered waves by spherical diffusers: influence of size parameter," *Phys. Rev. E* **49**, 1767–1770 (1994).

[66] E. E. Gorodnichev, A. I. Kuzolov, and D. B. Rozozkin, "Diffusion of circularly polarized light in a disordered medium with large scale inhomogeneities," *JETP Lett.* **68**, 22–28 (1998).

[67] A. D. Kim and M. Moscoso, "Influence of the refractive index on the depolarization of multiply scattered waves," *Phys. Rev. E* **64**, 026612 (2001).

[68] L. F. Rojas-Ochoa, D. Lacoste, R. Lenke, P. Schurtenberger, and F. Scheffold, "Depolarization of backscattered linearly polarized light," *J. Opt. Soc. Am. A* **21**, 1799–1804 (2004).

[69] M. Xu and R. R. Alfano, "Random walk of polarized light in turbid media," *Phys. Rev. Lett.* **95**, 213901 (2005).

[70] A. J. Welch, M. J. C. Van Germert, W. M. Star, and B. C. Wilson, "Overview of tissue optics," in *Optical Thermal Response of Laser Irradiated Tissue*, edited by A. J. Welch and M. J. C. Van Germert (Plenum, New York, 1995).

[71] L. Wang, S. L. Jacques, and L. Zheng, "MCML—Monte Carlo modeling of light transport in multi-layered tissues," *Comput. Methods Programs Biomed.* **47**, 131–146 (1995).

[72] N. Ghosh, P. K. Gupta, A. Pradhan, and S. K. Majumder, "Anomalous behavior of depolarization of light in a turbid medium," *Phys. Lett. A* **354**, 236–242 (2006).

[73] V. Sankaran, K. Schonenberger, J. T. Walsh Jr., and D. J. Maitland, "Polarization discrimination of coherently propagating light in turbid media," *Appl. Opt.* **38**, 4252–4261 (1999).

[74] V. Sankaran, J. T. Walsh Jr., and D. J. Maitland, "Comparative study of polarized light propagation in biological tissues," *J. Biomed. Opt.* **7**, 300–306(2002).

[75] N. Ghosh, A. Pradhan, P. K. Gupta, S. Gupta, V. Jaiswal, and R. P. Singh, "Depolarization of light in a multiply scattering medium: effect of refractive index of scatterer," *Phys. Rev. E* **70**, 066607 (2004).

[76] M. F. G. Wood, X. Guo, and I. A. Vitkin, "Polarized light propagation in multiply scattering media exhibiting both linear birefringence and optical activity: Monte Carlo model and experimental methodology," *J. Biomed. Opt.* **12**, 014029 (2007).

[77] J. C. Ramella-Roman, S. A. Prahl, and S. L. Jacques, "Three Monte Carlo programs of polarized light transport into scattering media: part I," *Opt. Express* **13**, 4420–4438 (2005).

[78] M. Moscoso, J. B. Keller, and G. Papanicolaou, "Depolarization and blurring of optical images by biological tissue," *J. Opt. Soc. Am. A* **18**, 948–960 (2001).

[79] R. Clark Jones, "New calculus for the treatment of optical systems. VII. Properties of the N-matrices," *J. Opt. Soc. Am.* **38**, 671–685 (1948).

[80] S. Alali, Y. Wang, and I. Alex Vitkin "Detecting axial heterogeneity of birefringence in layered turbid media using polarizd light imaging," *Biomed. Opt. Express* **3**, 3250–3263 (2012)

[81] N. Ghosh, M. F. G. Wood, and I. A. Vitkin, "Mueller matrix decomposition for extraction of individual polarization parameters from complex turbid media exhibiting multiple scattering, optical activity and linear birefringence," *J. Biomed. Opt.* **13**, 044036 (2008).

[82] N. Ghosh, M. F. G. Wood, and I. A. Vitkin, "Polarimetry in turbid, birefringent, optically active media: a Monte Carlo study of Mueller matrix decomposition in the backscattering geometry," *J. Appl. Phys.* **105**, 102023 (2009).

[83] S. G. Demos, W. B. Wang, J. Ali, and R. R. Alfano, "New optical difference approaches for subsurface imaging of tissues," *OSA TOPS* **21**, in *Advances in Optical Imaging and Photon Migration*, edited by J. G. Fujimoto and M. S. Patterson, pp. 405–410 (1998).

[84] Y. Liu, Y. L. Kim, X. Li, and V. Backman, "Investigation of depth selectivity of polarization gating for tissue characterization," *Opt. Express* **13**, 601–611 (2005).

[85] S. G. Demos, H. B. Radousky, and R. R. Alfano, "Deep subsurface imaging in tissues using spectral and polarization filtering," *Opt. Express* **7**, 23–28 (2000).

[86] A. P. Sviridov, V. C. M. Hassan, A. C. Boccara, A. Russo, P. Smith, and A. Gandjbackche, "Enhancement of hidden structures of early skin fibrosis using polarization degree patterns and Pearson correlation analysis," *J. Biomed. Opt.* **10**, 051706 (2005).

[87] S. L. Jacques, J. C. Ramella-Roman, and K. Lee, "Imaging skin pathology with polarized light," *J. Biomed. Opt.* **7**, 329–340 (2002).

[88] S. L. Jacques, R. Samathama, S. Isenhath, and K. Lee, "Polarized light camera to guide surgical excision of skin cancers," *Proc. SPIE* **6842** 68420I (2008).

[89] V. Backman, M. B. Wallace, L. T. Perelman, J. T. Arendt, R. Gurjar, M. G. Muller, Q. Zhang, G. Zonios, E. Kline, T. McGillican, et al., "Detection of preinvasive cancer cells in situ," *Nature (London)* **406**, 35–36 (2000).

[90] M. Hunter et al., "Tissue self-affinity and polarized light scattering in the born approximation: a new model for precancer detection," *Phys. Rev. Lett.* **97**, 138102 (2006).

[91] N. Ghosh, S. K. Majumder, H. S. Patel, and P. K. Gupta, "Depth resolved fluorescence measurement in layered turbid medium by polarized fluorescence spectroscopy," *Opt. Lett.* **30**, 162–164 (2005).

[92] Z. J. Smith and A. J. Berger, "Surface-sensitive polarized Raman spectroscopy of biological tissue," *Opt. Lett.* **30**, 1363–1365 (2005).

[93] R. S. Gurjar, V. Backman, L. T. Perelman, I. Georgakoudi, K. Badizadegan, I. Itzkan, R. R. Dasari, and M. S. Feld, "Imaging human epithelial properties with polarized light scattering spectroscopy," *Nat. Med.* **7**, 1245–1249 (2001).

[94] N. C. Biswal, S. Gupta, N. Ghosh, and A. Pradhan, "Recovery of intrinsic fluorescence from the measured fluorescence in a turbid medium: an experimental approach," *Opt. Express* **11**, 3320–3331 (2003).

[95] R. J. Mc Nichols and G. L. Cote, "Optical glucose sensing in biological fluids: an overview," *J. Biomed. Opt.* **5**, 5–16 (2000).

[96] M. F. G. Wood, D. Côté, and I. A. Vitkin, "Combined optical intensity and polarization methodology for analyte concentration determination in simulated optically clear and turbid biological media," *J. Biomed. Opt.* **13**, 044037 (2008).

[97] J. Chung, W. Jung, M. J. Hammer-Wilson, P. Wilder-Smith, and Z. Chen, "Use of polar decomposition for the diagnosis of oral precancer" *Appl. Opt.* **46**, 3038–3045 (2007).

[98] A. Pierangelo, A. Benali, M. R. Antonelli, T. Novikova, P. Validire, B. Gayet, and A. de Martino, "Ex-vivo characterization of human colon cancer by Mueller polarimetric imaging," *Opt. Express* **19**, 1582–1593 (2011).

[99] A. Pierangelo, S. Manhas, A. Benali, C. Fallet, J.-L. Totobenazara, M. R. Antonelli, T. Novikova, B. Gayet, A. de Martino, and P. Validire "Multispectral Mueller polarimetric imaging detecting residual cancer and cancer regression after neoadjuvant treatment for colorectal carcinomas," *J. Biomed. Opt.* **18**, 046014 (2013).

[100] O. Visser, R. Bakx, F. A. Zoetmulder, C. C. Levering, S. Meijer, J. F. Slors, and J. J. van Lanschot, "The influence of total mesorectal excision on local recurrence and survival in rectal cancer patients: a population-based study in Greater Amsterdam," *J. Surg. Oncol.* **95**(6), 447–454 (2007).

[101] M. Underwood, M. Arbyn, W. Parry-Smith, S. De Bellis-Ayres, R. Todd, C. Redman, and E. Moss, "Accuracy of colposcopy-directed punch biopsies: a systematic review and meta-analysis," *BJOG* **119**, 1293–1301 (2012).

[102] N. Thekkek and R. Richards-Kortum, "Optical imaging for cervical cancer detection: solutions for a continuing global problem," *Nat. Rev. Cancer* **8**, 725–731 (2008).

[103] M. Cardenas-Turanzas, J. A. Freeberg, J. L. Benedet, E. N. Atkinson, D. D. Cox, R. Richards-Kortum, C. MacAuley, M. Follen, and S. B. Cantor, "The clinical effectiveness of optical spectroscopy for the *in vivo* diagnosis of cervical intraepithelial neoplasia: where are we?," *Gynecol. Oncol.* **107** S138–S146 (2007).

[104] P. E. Gravitt, P. Paul, H. A. Katki, H. Vendantham , G. Ramakrishna, M. Sudula, B. Kalpana, B. M. Ronnett, K. Vijayaraghavan, K. V. Shah, and CATCH Study Team. "Effectiveness of VIA, Pap, and HPV DNA testing in a cervical cancer screening program in a peri-urban community in Andhra Pradesh, India," *PLoS ONE* **5**(10), e13711 (2010). doi:10.1371/journal.pone.0013711

[105] P. Shukla and A. Pradhan, "Mueller decomposition images for cervical tissue: potential for discriminating normal and dysplastic states," *Opt. Express* **17**, 1600–1609 (2009).

[106] D. Arifler, I. Pavlova, A. Gillenwater, and R. R. Kortum, "Light scattering from collagen fiber networks: micro-optical properties of normal and neoplastic stroma," *J. Biophys.* **92**, 3260–3274 (2007).

[107] D. J. Maitland and J. T. Walsh Jr., "Quantitative measurements of linear birefringence during heating of native collagen," *Lasers Surg. Med.* **20**, 310–318 (1997).

[108] M. F. G. Wood, N. Ghosh, E. H. Moriyama, B. C. Wilson, and I. A. Vitkin, "Proof-of-principle demonstration of a Mueller matrix decomposition method for polarized light tissue characterization in vivo," *J. Biomed. Opt.* **14**, 014029(2009).

[109] S. Alali, K. Aitken, D. Bagli, and I. A. Vitkin, "Optical assessment of anisotropy in ex-vivo distended rat bladders,'' *J. Biomed. Opt.* **17**, 109801 (2012).

[110] G. S. Jack, R. Zhang, M. Lee, Y. Xu, B. M. Wu, and L. V. Rodrigues, "Urinary bladder smooth muscle engineered from adipose stem cells and a three dimensional synthetic composite,'' *Biomaterials* **30**, 3259–3270 (2009)

[111] N. Ghosh, M. F. G. Wood, S. Li, R. D. Weisel, B. C. Wilson, R. Li, and I. A. Vitkin, "Mueller matrix decomposition for polarized light assessment of biological tissues," *J. Biophoton.* **2**, 145 (2009).

[112] M. F. G. Wood, N. Ghosh, M. A. Wallenburg, S.-H. Li, R. D. Weisel, B. C. Wilson, R.-Ki Li, and A. Vitkin, "Polarization birefringence measurements for characterizing the myocardium, including healthy, infracted, and stem cell treated regenerating cardiac tissues," *J. Biomed. Opt.* **15**, 047009 (2010).

[113] M. A. Wallenburg, M. F. G. Wood, N. Ghosh, and I. A. Vitkin, "Polarimetry-based method to extract geometry-independent metrics of tissue anisotropy," *Opt. Lett.* **35**, 2570–2572 (2010).

[114] H. He, Z. Nan, L. Ran, Y. Tianliang, L. Wei, H. Yonghong, and M. Hui, "Application of sphere-cylinder scattering model to skeletal muscle," *Opt. Express* **18**, 15104–15112 (2010).

[115] S. Alali, Y. Wang, and I. A. Vitkin, "Detecting axial heterogeneity of birefringence in layered turbid medial using polarized light imaging," *Biomed. Opt. Express* **3,** 3250–3263 (2012).

[116] A. Myakov, L. Nieman, L. Wicky, U. Utzinger, R. Richards-Kortum, and K. Sokolov, "Fiber optic probe for polarized reflectance spectroscopy *in vivo*: design and performance," *J. Biomed. Opt.* **7**(3), 388–397 (2002).

[117] V. M. Turzhitsky, A. J. Gomes, Y. L. Kim, Y. Liu, A. Kromine, J. D. Rogers, M. Jameel, H. K. Royand, and V. Backman," Measuring mucosal blood supply *in vivo* with a polarization gating probe," *Appl. Opt.* **47**(32), 6046–6057 (2008).

[118] T. C. Wood and D. S. Elson, "Polarization response measurement and simulation of rigid endoscopes," *Biomed. Opt. Express* **1,** 463–471 (2010).